Fundamental dislocation theory and 3D dislocation mechanics

Volker Mohles *

* Institute of Physical Metallurgy and Metals Physics, RWTH Aachen, Aachen, Germany

Abstract In chapter 1 an introduction to basic dislocation properties in an elastic continuum is given. Displacements, strains, stresses and energies of straight edge and screw dislocations are compiled as well as forces on dislocations, implications of dislocation motion and aspects of dislocations in real crystals. Chapter 2 details the models of dislocation self interaction for curved dislocations including the line tension model and linear elastic self interaction. The former is essential for basic understanding, whereas the latter is the basis of accurate dislocation dynamics simulations of plasticity. In chapter 3 these models are applied for 2-dimensional dislocation glide which allow to calculate the strengthening effect of second phase particles and solute atoms in a material. Finally, aspects of 3-dimensional dislocation motion are outlined in chapter 4.

1 Basic Dislocation Theory

1.1 Heuristic Dislocation Creation

In the literature, a number of excellent introductions to the basics of dislocation theory have been given (e.g. (Hirth and Lothe, 1992), (Hull and Bacon, 1992), (Weertman, 1992)). They cover the historical development of the dislocation concept (Volterra, 1907), (Peierls, 1940), experimental discovery of dislocations in crystals (Orowan, 1934), (Polanyi, 1934), (Taylor, 1934) and overviews of physical phenomena which can only show up in the presence of dislocations. Moreover, detailed introductions to linear elasticity theory have been given (Hirth and Lothe, 1992) because elastic distortions and stresses determine most of the dislocation properties: about 80-90% of a dislocation's energy is stored in the elastic strains. The present compilation of dislocation theory addresses students and researchers who already have a certain knowledge in dislocation theory, but who want to refresh and extend their understanding, in particular with respect to dislocation dynamics simulations. From the start, it is emphasized that, in

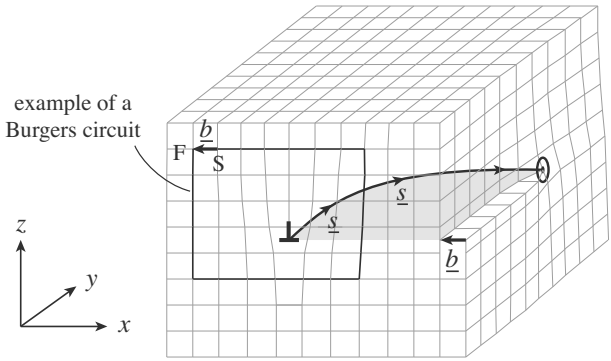

Figure 1. Dislocation in a linear elastic medium. The dislocation (black line) demarcates the area (light grey) in which the material has slipped by the Burgers vector $\underline{b}$, which is a lattice vector. The sign of $\underline{b}$ and of the line vector $\underline{s}$ can only be defined in combination.

general, dislocations are curved and flexible.

The generation of a dislocation in a linear elastic continuum can be envisaged by the following hypothetical steps: First, a cut is performed through part of a specimen along a certain plane. Then one of the surfaces which have been newly created by the cut is shifted by a vector $\underline{b}$, called the Burgers vector. Finally the surfaces are rejoined and the specimen is allowed to relax. An example for the outcome of this procedure is plotted in figure 1. The light grey area is the plane in which the cut had been performed. This area is framed by the specimen's dimensions and by the line which the tip of the hypothetical knife had moved along. This latter line (thick and black in figure 1) is the new dislocation. All material that does not include a piece of dislocation is distorted and elastically stressed, but it is still continuous. This includes the area of the hypothetical cut.

The dislocaton itself is a displacement singularity, as can be seen from the Burgers circuit. The construction of this circuit requires a lattice in the material, which is naturally given by the atomic arrangement of any real crystal. In figure 1 a simple cubic lattice has been used for simplification. The Burgers circuit is started at any lattice point S. From S, a number of i, j, and k steps along the lattice vectors in x-, y-, and z-direction, respectively, are drawn subsequently. From there, the same numbers of steps are drawn in the same order along the lattice vectors in the opposite direction. This defines the final lattice point F. In a perfect lattice or even in a distorted but continuous one, F equals S so that a closed circuit has been

described by these six lattice vectors. But if the described sequence of six vectors encloses a dislocation, an additional lattice vector from F to S is required to close the circuit. This defines the Burgers vector $\underline{b}$. Disregarding continuous lattice distortions, its magnitude and direction are independent of the choice of the numbers i, j, and k and of the starting point S as long the dislocation is enclosed by the circuit. However, a convention about the sign of $\underline{b}$ is required because an inversion of the circuit's sense would yield $-\underline{b}$ instead of $\underline{b}$, while the real geometry is not changed at all. The convention must link the sign of $\underline{b}$ to the actual shift that had been used in the above hypothetical dislocation generation. A convenient and always applicable way is to assign a local tangent vector $\underline{s}$ to the dislocation. This defines the line direction or 'line vector'. Then the Burgers circuit is performed following the right-hand-rule, where the thumb points in the line direction. $\underline{b}$ is defined as the vector from start (S) to finish (F). This is the most frequently used rule (see (Hirth and Lothe, 1992)), and it is adopted subsequently. However, there are prominent exceptions (Weertman, 1992); therefore one must be careful about which convention is taken. In any case, the sign of the Burgers vector $\underline{b}$ and the line vector $\underline{s}$ can only be defined in combination. It is important for consistency that the right-hand Burgers circuit yields the vector $\underline{b}$ indicated in the figure. This can easily be verified on the front plane (y=const., with j=0) or on the right side (x=const., with i=0) of the specimen. When $\underline{s}$ is inverted, $\underline{b}$ is reversed as well so that the same geometry is described.

From the hypothetical way in which the dislocation in figure 1 had been produced, several fundamental dislocation properties can be deduced. One is that the Burgers vector $\underline{b}$, being identical to the shift vector, is a lattice vector, which is constant by definition with respect to magnitude and direction. Obviously three cases are to be distinguished: Firstly, $\underline{b}$ and the line vector $\underline{s}$ are parallel and lie in the 'cutting plane'. This is the case for the dislocation part that leaves the crystal on the right side of figure 1. Owing to the geometry of the displacements visible on this free surface, this dislocation part is said to have screw character. Secondly, $\underline{s}$ is normal to $\underline{b}$ but both lie in the cutting plane. This case is found on the dislocation portion that leaves the crystal on the front plane. This part has, by definition, edge character. And thirdly, $\underline{b}$ is normal to the cutting plane (and to $\underline{s}$); this case is called a prismatic dislocation (see below).

Another feature becoming apparent from figure 1 is that a dislocation cannot terminate inside a crystal because it represents the fringe of a plane, the slipped area. Still it can be useful to refer to dislocation segments or parts (short straight pieces) in order to describe local properties, like the dislocation character. The possibility of a blurred fringe and hence a

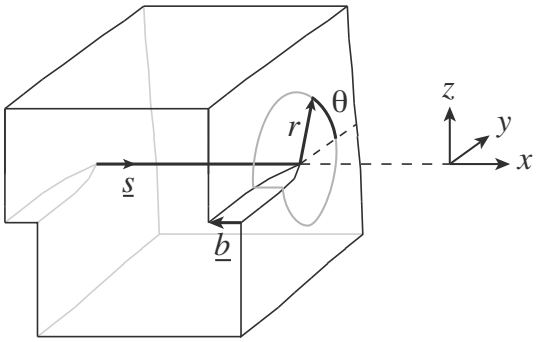

Figure 2. Straight screw dislocation. With $\underline{s}$ parallel to $\underline{b}$, the glide plane is undefined.

distributed dislocation is discussed later. When a dislocation moves, the slipped region increases or decreases with the motion. This means that the crystal is deformed, which enables crystal plasticity. In the following, dislocation features are described in more detail.

1.2 Basic Dislocation Types

According to the hypothetical generation of a dislocation described in the introduction, several basic types of dislocation can be distinguished, depending on the angular relations between Burgers vector $\underline{b}$, line vector $\underline{s}$ and the 'cutting plane'. In the following, the coordinate system is equivalently given either by $\underline{x}_1 = (x_1, 0, 0)$, $\underline{x}_2 = (0, x_2, 0)$, $\underline{x}_3 = (0, 0, x_3)$, or by $\underline{x} = (x, 0, 0)$, $\underline{y} = (0, y, 0)$, $\underline{z} = (0, 0, z)$, whichever is more convenient.

Straight screw dislocation The displacement u_x in the direction x caused by a straight screw dislocation along the x-axis can be read directly from figure 2: When the angle θ around the dislocation line is increased by 2π, a displacement of one lattice vector along the x-axis occurs. This is, by the definition of the Burgers circuit, one Burgers vector $\underline{b}$. When elastic isotropy is assumed for the material and the block is extended infinitely in all directions, the incremental displacement $\mathrm{d}u_x/\mathrm{d}\theta$ will be equally distributed (i.e., constant) over the whole range $0 \leq \theta < 2\pi$. This yields

$$u_x(r, \theta) = b\frac{\theta}{2\pi} = \frac{b}{2\pi}\tan^{-1}\left(\frac{z}{y}\right) \tag{1}$$

Note that u_x does not depend on the radius r of the circuit. In figure

2 this has been relaxed: there the displacement has been assumed to be distributed approximately over the range $0 < r < b = |\underline{b}|$; this is equivalent to a blurred fringe of the cutting plane mentioned earlier. With the general definition of the strain tensor $\boldsymbol{\varepsilon}$ or $\{\varepsilon_{ij}\}$,

$$\varepsilon_{ij} = \frac{1}{2}\left(\frac{\partial u_i}{\partial x_j} + \frac{\partial u_j}{\partial x_i}\right) \tag{2}$$

and with Hook's law

$$\sigma_{ij} = C_{ijkl}\ \varepsilon_{kl} \tag{3}$$

which connects the stess tensor $\{\sigma_{ij}\}$ with the strains $\{\varepsilon_{ij}\}$ and the stiffness tensor $\{C_{ijkl}\}$, the stresses of the straight screw dislocation can be derived from (1) by elementary mathematics. Note that in equation (3) and subsequently, Einstein's summation convention is applied: summation is to be performed over equal indices (k and l in (3)). In case of an elastically isotropic material the stiffness tensor $\{C_{ijkl}\}$ contains only two independent elastic constants (see e.g. (Hirth and Lothe, 1992)), for instance, the shear modulus μ and Poisson's ratio ν. With these, the resulting stresses for the screw dislocation along the $\underline{x}$-axis can be written as $\sigma_{yz} = \sigma_{xx} = \sigma_{yy} = \sigma_{zz} = 0$ and

$$\sigma_{xy} = -\frac{\mu b}{2\pi}\frac{z}{y^2+z^2}, \quad \sigma_{xz} = \frac{\mu b}{2\pi}\frac{y}{y^2+z^2} \tag{4a}$$

or

$$\sigma_{x\theta} = -\frac{\mu b}{2\pi r} \tag{4b}$$

with all other components vanishing in cylindrical coordinates.

The stresses and strains around the dislocation mean that a certain elastic energy is stored by the dislocation. As mentioned in the introduction, this energy accounts for 80-90% of the total energy of a dislocation and therefore controls many of its properties. In general, the elastic energy E can be calculated by integrating over the volume the elastic energy density, which is $\sigma_{ij}\varepsilon_{ij}/2$. For a dislocation it is more useful to calculate the energy per unit length, E^*, by integration over the area normal to it. Here and subsequently, the asterisk is meant to indicate a length specific unit.

$$E^* = \frac{1}{2}\int \sigma_{ij}\ \varepsilon_{ij}\ dy\ dz \tag{5}$$

For the screw dislocation it is most convenient to use cylindrical coordinates and equation (4b) for $\sigma_{x\theta}$. In case of elastic isotropy with $\varepsilon_{x\theta} = \sigma_{x\theta}/\mu$, this

yields

$$E^*(\text{screw}) = \frac{1}{2}\int_0^{2\pi}\int_{r_{\text{core}}}^{r_{\text{shield}}} \frac{\mu b^2}{4\pi^2 r^2} r \; dr \; d\theta = \frac{\mu b^2}{4\pi}\ln\frac{r_{\text{shield}}}{r_{\text{core}}} \qquad (6a)$$

Here the integration has been restricted to the range $r_{\text{core}} < r < r_{\text{shield}}$ because the integral diverges for $r \to 0$ and for $r \to \infty$. The divergence of $E^*(r \to 0)$ arises obviously because the validity of linear elasticity breaks down when r reaches down to atomic scales, that is a few times b. Hence with $r_{\text{core}} = 3b$, for example, the energy of the dislocation core is left out of E^*. Anyway, with an appropriate choice of r_{core}, the missing core energy with its atomistic nature can still be taken into account approximately: this is usually done with a smaller core radius $r_{\text{core}} \approx 1b$.

In a real specimen the divergence of $E^*(r \to \infty)$ is prevented by the finite size of the specimen. This shows that even if the core energy were known accurately, it is not possible to ascribe a certain value to the total energy of a dislocation. Usually a crystal contains a number of dislocations in each of the opposite the signs. In that case these opposite dislocations compensate for each other's stresses and strains, in effect, shielding each other. Therefore a useful shielding distance r_{shield} is half the distance between nearest dislocations. Because of the logarithmic dependence of $E^*(r_{\text{shield}}/r_{\text{core}})$ and $r_{\text{shield}} \gg r_{\text{core}}$, the exact choice of r_{shield} is not too important.

For the derivation of $\sigma_{x\theta}$ (equation (4b)) it had been assumed that the dimensions of the specimen are infinite in all directions. This condition is obviously violated when r_{shield} is chosen to be finite in equation (6a), which uses $\sigma_{x\theta}$. When $\sigma_{x\theta}$ is derived for a screw dislocation in a rod with free cylindrical boundaries, E^* comes out to be lower than in equation (6aa) by the term $\mu b^2/(4\pi)$. Hence altogether, a good approximation for the energy of a straight screw dislocation is

$$E^*(\text{screw}) = \frac{\mu b^2}{4\pi}\left(\ln\frac{r_{\text{shield}}}{b} - 1\right) \qquad (6b)$$

Straight edge dislocations The derivation of stresses and strains is more elaborate for straight edge than for screw dislocations. The reasons are that there is no radial symmetry around the dislocation, and that there are normal stresses $(\sigma_{xx}, \sigma_{yy}, \sigma_{zz})$ and normal strains $(\varepsilon_{xx}, \varepsilon_{yy}, \varepsilon_{zz})$ involved. Both can be seen in figure 3: The dislocation is the line which terminates the half-plane inserted from the top or squeezed into the rod from the right side during the hypothetical generation procedure outlined. Obviously, there is a compressive stress σ_{xx} above the light grey plane and a tension below it,

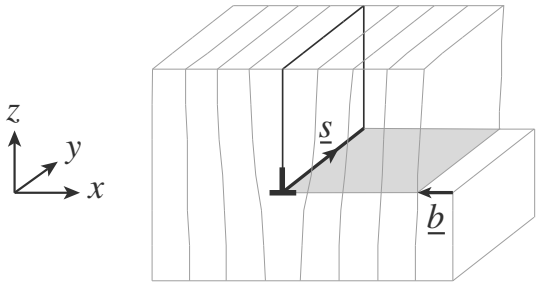

Figure 3. A straight edge dislocation is equivalent to an additional or missing half plane.

where the lattice is widened in x-direction. The derivation of all the stress components are omitted here, but the results are compiled for later reference. For an edge dislocation in an infinite medium with the line vector $\underline{s}$ equal to the y-axis and a Burgers vector $\underline{b}$ pointing in positive x-direction (inverse to the case of figure 3), the stress components are $\sigma_{xy} = \sigma_{yz} = 0$ and

$$\begin{aligned} \sigma_{xx} &= \frac{\mu b}{2\pi(1-\nu)} \frac{-z\left(3x^2+z^2\right)}{\left(x^2+z^2\right)^2}, \quad \sigma_{zz} = \frac{\mu b}{2\pi(1-\nu)} \frac{z\left(x^2-z^2\right)}{\left(x^2+z^2\right)^2}, \quad (7) \\ \sigma_{yy} &= \nu\left(\sigma_{xx}+\sigma_{zz}\right), \quad \sigma_{zx} = \frac{\mu b}{2\pi(1-\nu)} \frac{x\left(x^2-z^2\right)}{\left(x^2+z^2\right)^2} \end{aligned}$$

Again, elastic isotropy is assumed, and ν denotes the Poisson ratio. The strain energy of the edge dislocation is found in full analogy to E^*(screw) of equation (6a). This yields:

$$E^*(\text{edge}) = \frac{\mu b^2}{4\pi(1-\nu)} \left(\ln \frac{r_{\text{shield}}}{b} - 1\right) \quad (8)$$

Dislocations with mixed character Edge and screw dislocations have their line vectors $\underline{s}$ normal or parallel, respectively, to the Burgers vector $\underline{b}$. As is obvious from the hypothetical dislocation generation, a general dislocation has neither edge nor screw, but mixed character. In case of a curved dislocation, the character even varies locally along the dislocation line: $\underline{b}$ is constant, but $\underline{s}$ varies (figure 1). Still, the distinction between edge and screw character remains useful. For instance, the energy E^* of a straight dislocation with mixed character can be superimposed from equations (6ab) and (8). This is possible because parallel screw and edge dislocations do

not interact with each other (within linear elasticity): a screw dislocation along the x_2-direction (parallel to the edge dislocation in figure 3) has only σ_{12} and σ_{23} as non-vanishing stress components (and the respective strain components ε_{12} and ε_{23}); all other components equal zero. This can be seen from (4b)) with x_1- and x_2-directions exchanged. For the edge dislocation this is just vice versa (see above equation (8)): $\sigma_{12} = \sigma_{23} = 0$. With this and the Peach-Koehler formula detailed in section 1.3, it can be shown that E^* of the mixed-character dislocation can be written as:

$$E^*\left(\underline{b}^0, \underline{s}^0\right) = \left|\underline{b}^0 \times \underline{s}^0\right|^2 E^*(\text{edge}) + \left|\underline{b}^0 \cdot \underline{s}^0\right|^2 E^*(\text{screw}) \tag{9}$$

Here and subsequently, the superscript 0 in $\underline{b}^0$ and $\underline{s}^0$ indicates that the respective vectors have unit length. The fact that E^* is an energy per unit length suggests that the total energy of a curved dislocation can be found by integrating equation (9) along its curved path. However, this is only an approximation. The theory of curved dislocations is detailed in chapter 2.

Prismatic dislocation loops In case of the dislocations described in the previous sections, the shift vector $\underline{b}$ lay in the cutting plane. If $\underline{b}$ is normal to this plane, a layer of material must be inserted between the two cutting surfaces before rejoining, as sketched in figure 4, or removed. The dislocation bordering the cutting plane has edge character regardless of its course in this plane. Consequently, its energy E^* is essentially given by equation (8). If the shape of the loop is assumed circular, the shield radius r_{shield} is given by the radius of the loop: the dislocation part on the opposite site of the loop has the opposite sign, because the line vector points in the opposite direction there. Prismatic loops represent dislocation dipoles; as such they hardly contribute to plasticity.

1.3 Moving Dislocations

The most important property of dislocations is that they enable plastic deformation: the overall shape of a crystal changes permanently when dislocations move. For instance, a cube is transformed into the shape in figure 5 when a dislocation with the indicated Burgers vector $\underline{b}$ moves through it in the grey surface. There are other mechanisms which enable plastic deformation, like twinning, grain boundary sliding and phase transformations, but in general, plasticity is dominated by dislocations.

Dislocation glide and climb Two basic types of dislocation motion are to be distinguished: glide and climb. In figure 5, the effect of dislocation glide has been sketched. Note that this shape may have resulted from the

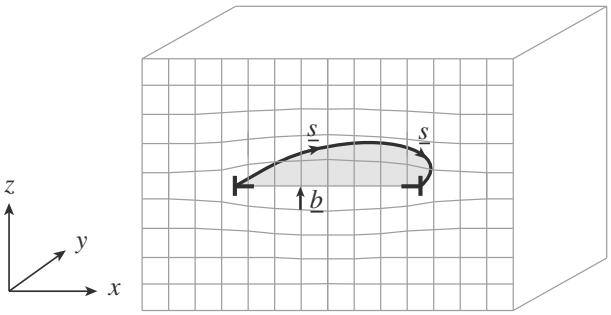

Figure 4. Half a prismatic dislocation loop.

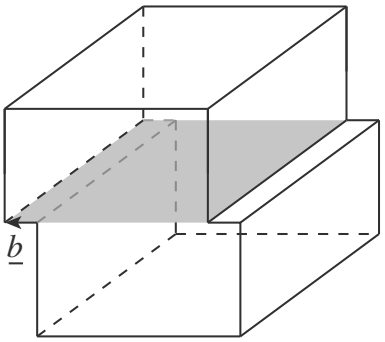

Figure 5. Sheared Cube after glide of dislocations in figures 1, 2 or 3.

motion of a screw dislocation, an edge dislocation or even a curved one: In figure 2, the screw dislocation may have moved from the front to the back plane; in figure 3, the edge dislocation may have moved from the right to the left side. Or in figure 1, the quarter dislocation loop may have expanded to the back left corner. For all three cases the grey area in figure 5 indicates the glide plane. It is described by the dislocation's line vector $\underline{s}$ and, in principle, by the direction of its motion, which is always perpendicular to $\underline{s}$. It is more convenient, though, to use $\underline{s}$ and the Burgers vector $\underline{b}$ to define the glide plane and its normal vector $\underline{n}^0$:

$$\underline{n}^0 = \frac{\underline{b} \times \underline{s}}{|\underline{b} \times \underline{s}|} \tag{10}$$

In the case of a screw dislocation, where $\underline{s}$ is parallel to $\underline{b}$, the glide plane $\underline{n}^0$ is undefined: The screw dislocation can glide in any direction — but only

in the continuum description used here. In real crystals, Burgers vectors and glide planes are restricted to certain crystallographic directions (section 1.4). But within these restrictions, several glide directions (and hence actual glide planes) are equivalent for screw dislocations. This means that screw dislocations can even switch their glide plane; this effect is called cross-slip and detailed in section 4.1.

For edge and mixed-character dislocations, though, the glide plane $\underline{n}^0$ is fixed. The motion normal to $\underline{n}^0$ is called climb. It is associated with material transport: when the edge dislocation in figure 3 moves up or downwards (normal to the glide plane), material must be moved away from or towards the dislocation line, respectively. This changes the total volume of the rod; therefore, climb is called non-conservative motion, as opposed to glide, which is conservative. The material transport can happen by diffusion. Except at very high temperatures, diffusion is a very slow process. Hence climb is extremely slow as compared to glide, which can proceed at sound velocity. Therefore in most cases, plastic deformation is dominated by glide.

In case of the prismatic loop of figure 4, the glide plane is a cylinder: the dislocation can glide up and down. To extend the loop, in contrast, reguires material to diffuse towards the dislocation. However, prismatic dislocation loops are usually of minor importance.

Macroscopic shape change Since the Burgers vector is usually very small compared to the sample's dimensions, the shape change caused by dislocation glide can be considered as continuous since the steps on a surface like in figure 3 are usually negligibly small. Still, the overall shape change is of importance, for instance its elongation. To quantify the length change in relation to dislocation glide, a rod is sketched in figure 6 before and after the glide of a dislocation with arbitrary glide plane and Burgers vector. The rod suffers the elongation $\Delta h = b \cdot \cos\lambda$, where λ is the angle between $\underline{b}$ and the z-direction, in which the length h is measured. The relative length change, $\Delta\varepsilon = \Delta h/h$, called strain, can be written as

$$\Delta\varepsilon = \frac{b\ \cos\lambda}{h} = b\ \cos\lambda \frac{\Delta x}{V}\Delta y = b\ \cos\lambda \frac{\Delta x}{V}\ \Delta y_{\mathrm{g}}\ \cos\phi \tag{11}$$

Here $V = h\Delta x\Delta y$ is the volume of the rod, Δy_{g} is the distance the dislocation moves in its glide plane, and ϕ is the angle between the glide plane vector $\underline{n}$ and the z-direction. The expression $\Delta x/V$ can be interpreted as the dislocation density in the rod, which is defined as the total dislocation length (here: Δx) per volume. More accurately, $\rho_{\mathrm{m}} = \Delta x/V$ is the mobile dislocation density because only dislocations that actually move contribute to deformation. If we divide equation (11) by a time step Δt and read

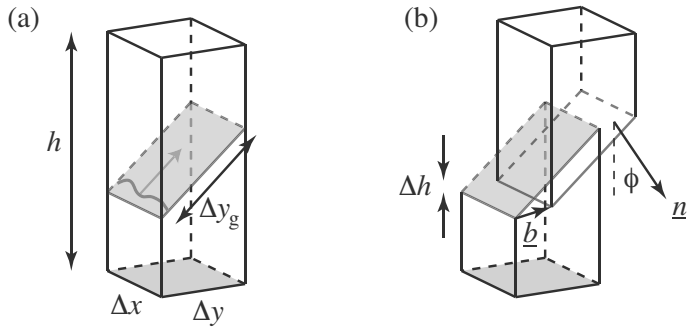

Figure 6. A rod before and after glide of a single general dislocation.

$\Delta y_{\mathrm{g}}/\Delta t$ as the dislocation's velocity v, we get the strain rate $\mathrm{d}\varepsilon/dt$:

$$\dot{\varepsilon} = b\ \rho_{\mathrm{m}}\ v\ \cos\lambda\ \cos\phi \tag{12}$$

When we introduce the Schmid factor $S = \cos\lambda\cos\phi$ and the resolved strain rate or 'shear rate' $\dot{\gamma} = \dot{\varepsilon}/S$, we obtain the Orowan equation. It relates the macroscopic amount of shear strain to the abundance and velocity of moving dislocations (regardless of any forces that drive the dislocations)

$$\dot{\gamma} = b\ \rho_{\mathrm{m}}\ v \tag{13}$$

Forces on dislocations When dislocation motion enables a shape change of a piece of material, then the corresponding external work must be 'consumed' by the moving dislocation, for instance, for overcoming obstacles. From this fact the forces on dislocations can be derived. In figure 7, a general force $\underline{F} = (F_x, F_y, F_z)$ is applied to shift the upper half of a cube to the left along the vector $\underline{b}$ (figure 5). If this force is caused by a general stress tensor $\boldsymbol{\sigma}$ acting on the top surface A_z of the cube, then $\underline{F}$ can be written as $\underline{F}_A = (A_z\sigma_{zx},\ A_z\sigma_{zy},\ A_z\sigma_{zz})$. With the shift vector $\underline{b}$, the external work is

$$\Delta W_{\mathrm{g}} = \underline{b} \cdot \underline{F}_A = b_x A_z \sigma_{zx} + b_y A_z \sigma_{zy} + b_z A_z \sigma_{zz} \tag{14}$$

The subscript g in ΔW_{g} stands for the 'global' view of the energy. The deformation is accomplished by an edge or screw dislocation, which takes a more local view: when it glides a distance d while a general force F is acting on it (F and d have the same directions), it consumes the energy $\Delta W_{\mathrm{l}} = Fd$. Here the subscript l stands for 'local'. By using $\Delta W_{\mathrm{l}} = \Delta W_{\mathrm{g}}$ (no other energies are involved) and the dislocation's length $L = A_z/d$

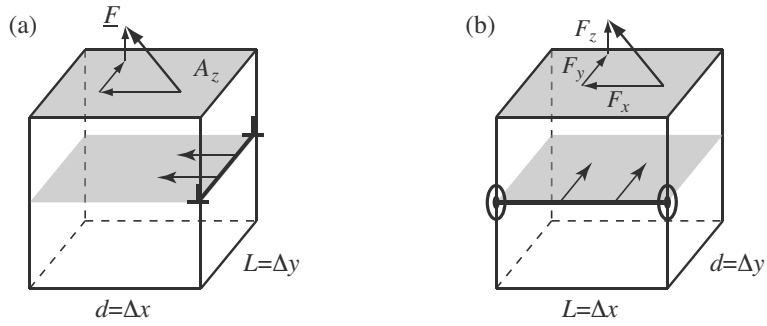

Figure 7. A force F is used to transform a cube into the shape of figure 5. The corresponding external work is equal to the energy that an edge (a) or screw (b) dislocation 'consumes' while gliding.

(figures 7(a) or 7(b)), we get

$$\frac{F}{L} = b_x\sigma_{zx} + b_y\sigma_{zy} + b_z\sigma_{zz} \tag{15a}$$

or, if we define $\tau = F/(bL)$,

$$\tau = b_x^0\sigma_{zx} = b_y^0\sigma_{zy} + b_z^0\sigma_{zz} \tag{15b}$$

τ is called the resolved shear stress. It is useful to keep in mind that by the definition just introduced, the resolved shear stress multiplied by the (constant) magnitude of the Burgers vector of a dislocation equals the force per unit length on this dislocation: $b\tau = F/L$. It should also be noted that in the derivation of τ we made no assumption about the line vector $\underline{s}$, hence τ is independent of $\underline{s}$. However, we assumed that $\boldsymbol{\sigma}$ acts only on the top surface A_z in figure 7, which is parallel to the glide plane, and underhand we prevented rotation. If we assume $\boldsymbol{\sigma}$ to act on all surfaces instead, rotation is avoided automatically and equation (15b) takes the more general form:

$$\tau = \underline{b}^0 \cdot \boldsymbol{\sigma} \cdot \underline{n}^0 \tag{16}$$

Again, n_0 is the normalized glide plane vector. If we assume $\underline{n}^0 = (0, 0, 1)$, we retain equation (15b). Since the Burgers vector $\underline{b}$ lies in the glide plane its component b_z vanishes; from this it can be seen that only shear components of a stress tensor $\boldsymbol{\sigma}$ give rise to τ and hence drive dislocation glide (σ_{zx} and σ_{zy} of equation (15b)). Equation (16) projects any stress tensor $\boldsymbol{\sigma}$ into the 'glide system', defined by the glide plane $\underline{n}$ and the Burgers vector $\underline{b}$. Hence,

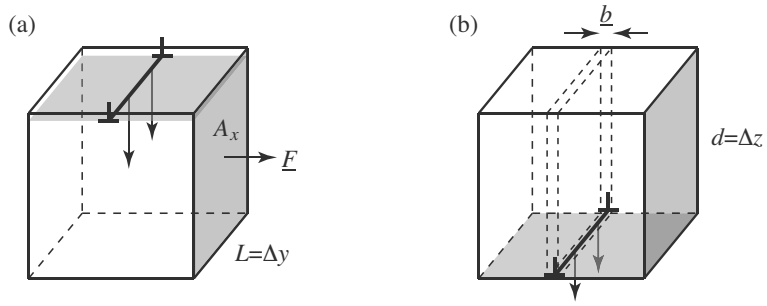

Figure 8. A force $\underline{F}$ is used to elongate a cube, which gives rise to a climb force on an edge dislocation.

it is also a generalized version of Schmid's law. The latter considers only a single stress component like in figure 6, where the sketched elongation may be caused by a force in z-direction on the upper and lower surfaces A_z. This means that all stress components of $\boldsymbol{\sigma}$ vanish except for σ_{zz}. Equation (16) can then be written as $\tau = S\sigma_{zz}$ where the Schmid factor, $S = \cos\lambda\cos\phi$, projects the normal stress σ_{zz} into the glide system.

But equation (16) is restricted to dislocation *glide* (as the 'glide system' implies). The driving force on an edge dislocation to *climb* can be derived in a similar way (figure 8): the external work $\Delta W_\mathrm{g} = \underline{F}_A \cdot \underline{b} = A_x\sigma_{xx}b_x + A_x\sigma_{xy}b_y + A_x\sigma_{xz}b_z$ is set equal to the energy $\Delta W_\mathrm{l} = Fd$ consumed by the climbing dislocation. From this, the climb force per unit length, F/L, and the respective climb stress τ_c (c stands for climb) is found to be

$$\tau_\mathrm{c} = b_x^0\sigma_{xx} + b_y^0\sigma_{xy} + b_z^0\sigma_{xz} \tag{17}$$

τ_c renders a driving force for material (interstitial atoms or vacancies) to move towards or away from the dislocation. When all surfaces A_x, A_y, and A_z are taken into account, τ and τ_c, which are both scalar values, can be combined to form the Peach-Koehler-formula (Peach and Koehler, 1950). It describes the local force vector $\underline{\Delta F}$ on a dislocation segment described by the line vector of finite length Δs:

$$\underline{\Delta F} = (\underline{b} \cdot \boldsymbol{\sigma}) \times \underline{\Delta s} \tag{18}$$

It should be emphasized that the cause for the stress $\boldsymbol{\sigma}$ plays no role here; it may result from an external force $\underline{F}$ as assumed above, from other dislocations as by equations (4) or (7), or from any other kind of stress source.

Forces on dislocations arise not only from elastic stresses $\boldsymbol{\sigma}$, but also

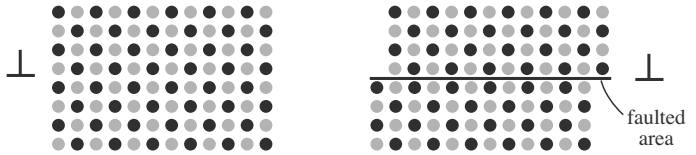

Figure 9. A dislocation creating an antiphase boundary while gliding through a long-range ordered crystal.

whenever the overall energy of a specimen is changed as a dislocation moves. For example, when the atoms in a specimen are usually ordered in some way, this order may be destroyed when a dislocation glides (or climbs) through it. A simplified case is sketched in figure 9, where a dislocation creates an antiphase boundary while gliding through a long-range ordered crystal. The boundary means an energy increment by the amount $E = A\gamma_{\text{fault}}$, where A is the faulted area and γ_{fault} is the specific fault energy. A dislocation of length L moving by a distance x sweeps the area $A = xL$, therefore, senses the force $F = -\mathrm{d}E/\mathrm{d}x = -L\gamma_{\text{fault}}$. The force per unit length F/L equals $-\gamma_{\text{fault}}$, and by the definition above the corresponding shear stress is

$$\tau_\gamma = -\gamma_{\text{fault}}/b \tag{19}$$

An energy change depending on dislocation motion can also arise when the elastic properties, the shear modulus μ in particular, vary locally inside a crystal. As can be seen from the derivation of equations (6ab) or (8), a dislocation's energy is stored in the elastic distortions around its core, and it is proportional to μ. For instance when a dislocation approaches a region with low shear modulus (a constant lattice constant is assumed here), its energy will decrease. Hence there will be a force that attracts the dislocation towards the region with low μ.

Interaction between straight dislocations With the stress tensors of screw and edge dislocations given by equations (4) and (7), respectively, and applying the Peach-Koehler equation (16), we can calculate the driving stress τ for glide that parallel dislocations impose on each other. To derive some qualitative insight in the interaction between dislocations we consider two dislocations as a stress source and a receiver, lying in parallel glide planes with normal vector $\underline{n}^0 = (0, 0, 1)$ and with parallel line vectors $\underline{s}^0 = (0, 1, 0)$, as sketched in figure 10. If we assume two screw dislocations first, their Burgers vectors are $\underline{b}_{\text{s}} = (0, b_{\text{s}}, 0)$ and $\underline{b}_{\text{r}} = (0, b_{\text{r}}, 0)$, and their mutual

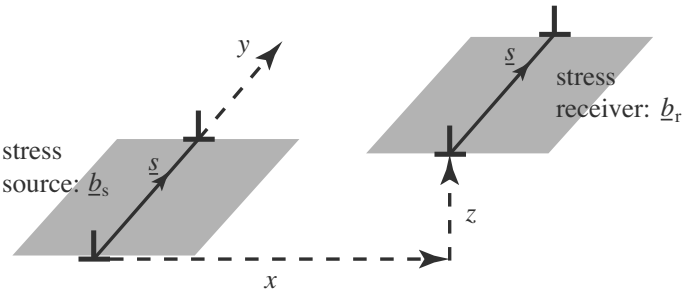

Figure 10. A stress receiving dislocation parallel to a source dislocation. The respective Burgers vectors $\underline{b}_r$ and $\underline{b}_s$ are meant to be arbitrary.

glide stress $\tau_{\text{screw}\to\text{screw}}$ is

$$\tau_{\text{screw}\to\text{screw}} = \frac{\mu b_s}{2\pi} \frac{x}{x^2 + z^2} \tag{20}$$

If the stress receiver is located right from the source ($x > 0$), it senses a positive stress $\tau_{\text{screw}\to\text{screw}}$ which drives it to more positive x-values, i.e. away from the source: parallel screw dislocations repel each other if they have the same sign. With either $\underline{b}_s$ or $\underline{b}_r$ inverted, the dislocations are called antiparallel, and they attract each other. When they meet, they annihilate each other. For instance, the two opposing half planes of antiparallel edge dislocations form a full plane of the crystal. For equation (20) it had been assumed that the dislocations are bound to the glide plane $\underline{n}^0 = (0, 0, 1)$. Pure screw dislocations in a continuous medium are not bound to a glide plane; for this case it may be derived that $\tau_{\text{screw}\to\text{screw}} = \mu b_s/(2\pi d)$, where d is the distance between the dislocations. However, in real crystals (section 1.4), screw dislocation motion is still bound to certain crystallographic planes.

If we consider two edge dislocations (as sketched in figure 10), the Burgers vectors are $\underline{b}_s = (b_s, 0, 0)$ and $\underline{b}_r = (b_r, 0, 0)$, and the mutual glide stress $\tau_{\text{edge}\to\text{edge}}$ is much more complicated. In particular, the sign of the interaction depends on x and z:

$$\tau_{\text{edge}\to\text{edge}} = \frac{\mu b_s}{2\pi(1-\nu)} \frac{x\left(x^2 - z^2\right)}{\left(x^2 + z^2\right)^2} \tag{21}$$

If the stress receiver is close to the source's glide plane ($z^2 < x^2$) the edge dislocations with equal sign repel each other, essentially like in the case of

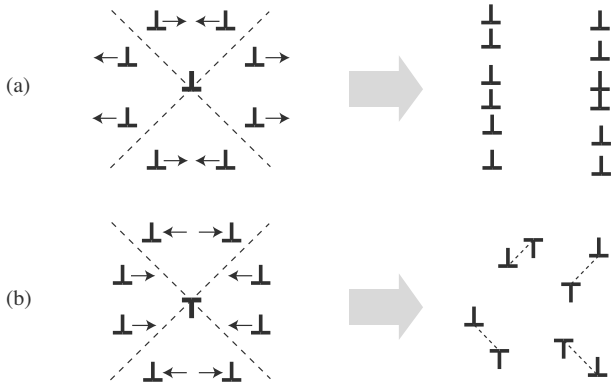

Figure 11. Interaction between edge dislocations in parallel glide planes: (a) parallel ones tend to form low angle boundaries; (b) antiparallel ones tend to form dipoles.

screw dislocations. But in the opposite case $z^2 < x^2$ the receiver is attracted, so that these dislocations tend to group above each other along the z-direction (figure 11(a)). Such groups form an interface between two parts of a crystal with slightly tilted crystallographic orientation: They are low angle tilt grain boundaries.

When edge dislocations of opposite sign are considered, $\tau_{\text{edge}\to\text{edge}}$ just switches its sign. The effect of this can be seen in figure 11(b): the stress receiving dislocation is attracted to the 45°-lines where $z^2 = x^2$; there, $\tau_{\text{edge}\to\text{edge}} = 0$. This means that edge dislocations of opposite sign tend to form dislocation dipoles, with a 45° angle between the glide plane and the shortest vector connecting both.

Dislocation dipoles have the important property that they cannot be driven by a homogeneous stress $\boldsymbol{\sigma}$: the two edge dislocations are driven in opposite directions. This may break up the dipole, but it will not drive it. In this sense, dipoles can be considered as immobile, in contrast to the mobile dislocations which actually enable plasticity. Even if they move, the bits of deformation the two edge dislocations cause cancel out each other for the most part.

Another important feature of dipoles is that the dislocations involved can move towards each other by a mix of glide and climb and finally annihilate. Climb requires material transport by diffusion, and hence this annihilation is kinetically inhibited. But since the edge dislocations attract each other, the dipole renders a driving force which attracts or emits interstitial atoms

or vacancies.

Between parallel edge and screw dislocations there is no elastic interaction: the combinations of $\underline{b}_\mathrm{s} = (0, b_\mathrm{s}, 0)$, $\underline{b}_\mathrm{r} = (b_\mathrm{r}, 0, 0)$, and $\underline{b}_\mathrm{s} = (b_\mathrm{s}, 0, 0)$, $\underline{b}_\mathrm{r} = (0, b_\mathrm{r}, 0)$, both yield $\tau_{\mathrm{screw}\to\mathrm{edge}} = 0$ and $\tau_{\mathrm{edge}\to\mathrm{screw}} = 0$, respectively. Hence without energy change, parallel screw and edge dislocations can be moved to fully coincide. By this procedure a straight dislocation with mixed character is generated. Conversely, this means that any mixed character dislocation with Burgers vector $\underline{b}$ may be considered as being composed of an edge and a screw dislocation with Burgers vector components $b_\mathrm{edge} = |\underline{b} \cdot \underline{s}^0|$ and $b_\mathrm{screw} = |\underline{b} \times \underline{s}^0|$, respectively. With these, the stress tensor $\boldsymbol{\sigma}$ of a mixed character dislocation may be written as

$$\boldsymbol{\sigma}^{\mathrm{mixed}}(\underline{b}) = \boldsymbol{\sigma}^{\mathrm{screw}}\left(b_\mathrm{screw}\right) + \boldsymbol{\sigma}^{\mathrm{edge}}\left(b_\mathrm{edge}\right) \tag{22}$$

where the components of $\boldsymbol{\sigma}^{\mathrm{screw}}$ and $\boldsymbol{\sigma}^{\mathrm{edge}}$ are, in principle, given by equations (4a) or (7), respectively. But before that, equation (4a) must be transformed such that the line vector $\underline{s}$, which had been assumed to point in x-direction for equation (4a) (figure 2), equals that for equation (7) (figure 3). This geometry has for instance been used in (Hirth and Lothe, 1992). However, in the present description, it has been chosen to use the same Burgers vector $\underline{b}$ for the cases in figures 1 to 3 to emphasize that $\underline{b}$ of a given dislocation is constant, so that a dislocation's character is exclusively determined by (variations of) the line vector $\underline{s}$ since, a variation of $\underline{b}$ is impossible for a given dislocation.

Image stresses So far it has been assumed that the dislocations reside in a specimen with infinite dimensions. However, often boundary conditions like free surfaces need to be considered. As is usual in other physical boundary condition problems, this can be done by assuming infinite dimensions, but adding entities which enforce the conditions involved with a given boundary. In case of elasticity and hence dislocations, a free boundary means that all forces on the boundary surface must vanish. In the case of figure 12, in which a free surface is assumed normal to the x-axis, this means $\sigma_{xx} = \sigma_{xy} = \sigma_{xz} = 0$. For a screw dislocation, this can easily be achieved by adding an additional dislocation of opposite sign mirrored to the opposite side of the surface: from equation (4b) it can be seen that the only non-vanishing stress component in cylindrical coordinates of a dislocation along the y-axis, $\sigma_{y\theta}$, depends only on the distance $r = \left(x^2 + z^2\right)^{1/2}$, which is always positive. Hence, all stresses of the dislocation (with $\underline{b}^{(1)}$, at $x^{(1)} = -L$, figure 12(a)) and its image counterpart (with $\underline{b}^{(2)} = -\underline{b}^{(1)}$, at $x^{(2)} = +L$) combined vanish in the whole plane $(0, y, z)$. The original

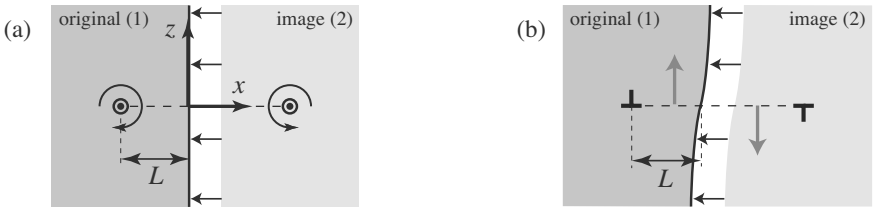

Figure 12. Material with image dislocations used to account for a free surface; (a) exact solution for a screw dislocation; (b) approximation for an edge dislocation.

dislocation is attracted towards the image dislocation and hence towards the free surface as described by equation (20) with $z = 0$ and $x = 2L$, i.e. with $\tau_{(2)\to(1)} = \mu b/(4\pi L)$.

The case of an edge dislocation parallel to a free surface is more complex. For the geometry used in figure 12(b), the stress components σ_{xy} vanish for both the original and the mirrored dislocation (section 1.2), and the componens σ_{xx} of the two compensate for each other (equation (7)). But in case of σ_{xz}, the components for the two dislocations add up because the sign of σ_{xz} depends not only on that of $\underline{b}$ but also on that of x (equation (7)). In figure 12(b) the non-vanishing stress components are indicated by grey arrows. In case of straight dislocations, the interaction between the dislocation and its image is still given by equation (21), with $z = 0$ and $x = 2L$, which results to $\tau_{(2)\to(1)} = \mu b/(4\pi L(1-\nu))$ (Hirth and Lothe, 1992). The stress components σ_{xz} are simply removed by a minor translational shift along the directions of the grey arrows.

The case of a free surface may be considered as an interface inside a specimen where the shear modulus switches from μ to zero, or where the material is infinitely soft. The other extreme is an interface to an infinitely rigid material ($\mu \to \infty$), which allows no elastic (or plastic) strains: $\varepsilon_{xx} = \varepsilon_{xy} = \varepsilon_{xz} = 0$. Similar to the case discussed above, this can be achieved by adding material with an image dislocation with the same Burgers vector: $\underline{b}^{(2)} = +\underline{b}^{(1)}$. In that case the dislocation experiences the same amount of stresses $\tau_{(2)\to(1)}$, but with inverted sign: The dislocation is repelled from the rigid part.

1.4 Dislocations In Real Crystals

In real crystals, the Burgers vector $\underline{b}$ and the glide plane vector $\underline{n}$ are bound to crystallographic directions: the Burgers circuit (section 1.1) is to

be performed along atomic positions, leaving an interatomic vector for $\underline{b}$. Since the energy of dislocations scales with b^2, the Burgers vector must be short; this leaves only a few possibilities. For a dislocation to glide, a glide plane must be 'smooth'. This is the case only when its normal vector points in certain crystallographic directions.

Perfect dislocations In a face centred cubic (fcc) lattice the elementary cell consists of a cube with one eighth of an atom in all eight corners and half an atom on all six faces. The shortest interatomic distance in this lattice is along the diagonals of the sides; hence in terms of lattice vectors, the Burgers vector has the type $\langle 110 \rangle$ and the length $a_0/2^{1/2}$, where a_0 is the lattice constant. The closest packed planes are normal to the space diagonal, hence the glide planes have Miller indices of the type $\{111\}$. In each of the four independent glide planes (111), $(\bar{1}11)$, $(1\bar{1}1)$, and $(11\bar{1})$, there are three possible Burgers vector directions such that $\underline{b} \cdot \underline{n} = 0$ (for instance $[\bar{1}10]$, $[\bar{1}01]$ and $[01\bar{1}]$ for (111)), hence there are 12 glide systems of this kind. One example is sketched in figure 13. An edge dislocation in the depicted $(1\bar{1}1)$-plane with the indicated Burgers vector would have the line vector $s^0 = 6^{-1/2}[121]$ along the dark atoms. These latter atoms can be seen as the first ones of the missing half plane inside the volume that has not been plotted. There are actually two rows of dark atoms along the dashed lines; this will be detailed later on in the context of partial (i.e. non-perfect) dislocations.

The elementary cell of a body centred cubic (bcc) lattice is a cube with one eighth of an atom in all eight corners and one atom in its centre. The shortest interatomic vector and hence the Burgers vector is of the type $\langle 111 \rangle$ and has the length $\left(3^{1/2}/2\right) a_0$. There are three possible types of glide planes which are experimentally observed: $\{110\}$, $\{112\}$ and $\{123\}$. Among these, the $\{110\}$-planes sketched in figure 14 have the closest packing. There are six non-parallel planes of this type, and each of them can contain two Burgers vectors, for instance, $[111]$ and $[11\bar{1}]$ for the $(\bar{1}10)$-plane. So there are 12 glide systems of this type. Of the $\{112\}$-planes there are 12. Each can contain only one Burgers vector, for instance $[11\bar{1}]$ for the (112)-plane. This gives another 12 glide systems. Finally there are 24 $\{123\}$-planes, which contain one Burgers vector each. Hence there are 48 glide systems altogether in body centred cubic crystals.

In principle, any plane qualifies as a glide plane as long as it contains the Burgers vector. For instance, the (134)-plane contains the direction $[11\bar{1}]$, but glide on $\{134\}$-planes is not observed: the glide is prevented by the Peierls stress τ_{Peierls}. This stress describes all resistance against glide that a dislocation experiences due to the atomistic nature of its core in a

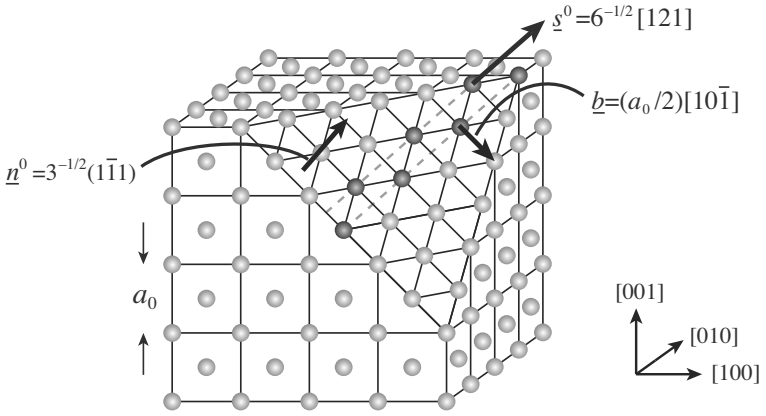

Figure 13. Glide plane $\underline{n}$ and Burgers vector $\underline{b}$ in a face centred cubic crystal. The dark atoms indicate the direction of an edge dislocation, for instance the first atoms of the missing half plane.

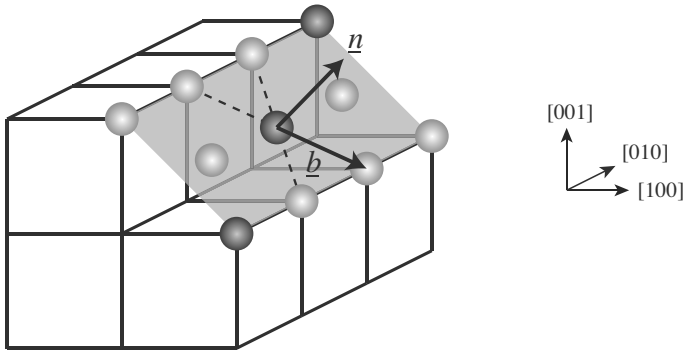

Figure 14. A glide plane $\underline{n} = (101)$ and Burgers vector $\underline{b} = [11\bar{1}]$ in a body centred cubic crystal. The dark atoms indicate the direction $[\bar{1}21]$ of an edge dislocation, for instance the first atoms of the missing half plane.

given plane. This resistance has a short-ranged periodic nature inherited from the crystal structure, the glide plane and the glide direction. Brownian motion of the atoms, i.e. thermal pulses on them, helps a dislocation to overcome this resistance, as if the glide plane were smoothed out by temperature. Therefore, τ_{Peierls} is a function of temperature. In case of face centred cubic crystals the glide planes are closely packed (figure 13) and therefore 'smooth'; the Peierls stress in these crystals is negligible even at room temperature. But in body centred cubic materials, only the $\{110\}$-planes are rather smooth. The other glide planes $\{112\}$ and $\{123\}$ need to be 'smoothed' by temperature, so that they are active only at higher temperatures.

Among metals the hexagonal crystal structure is also of importance. Here the basal planes $\{0001\}$ enable three glide directions of the type $\langle 11\bar{2}0\rangle$. Furthermore, three prism planes of the type $\{10\bar{1}0\}$ with one glide direction each (type $\langle 11\bar{2}0\rangle$) can be active as well as the pyramidal $\{10\bar{1}1\}$-planes, also with a $\langle 11\bar{2}0\rangle$ glide direction. As long as the axes of the hexagonal crystal have a ratio $c/a \geq 1.63$, the basal plane is closest packed and always active. However, in case of an axis ratio $c/a \leq 1.63$, the density in the plane can get as low as that in the other planes. Again, temperature decides which glide systems get activated first.

Partial dislocations As outlined before, a Burgers vector $\underline{b}$ must be short because a dislocation's energy scales with b^2. So far we have assumed that $\underline{b}$ is a lattice vector, but this is not always required. A face centred cubic crystal, for instance, can be seen as a periodic stack of three closely packed atom layers, as indicated in figure 15(a). The layers A, B, and C differ by small translational vectors for valid atom positions in the plane, as can be seen in figure 15(b). In a perfect fcc crystal, which has the closest possible packing density, a C layer must follow a sequence of A and B to form an $ABCABC$ stack. The same packing density can be found with an $ABABAB$ stacking sequence, but this would mean a slight increase of the free energy. An $ABABAB$ stack would form a hexagonal crystal with closest packing and an axis ratio of $c/a = 1.63$. However, the quoted fcc materials obviously prefer the fcc crystal and, therefore, the $ABCABC$ sequence.

In figure 15(b), part of the atoms in layer B, which lies on top of a C layer, have been shifted such that they reach another valid B-position. This corresponds to the Burgers vector $\underline{b}$ of a perfect dislocation. But instead, these atoms can also shift so that they reach an A-position. This creates a partial dislocation (here: Shockley partial dislocation) and a stacking fault on one side of it. The stacking fault entails an increase of the free energy,

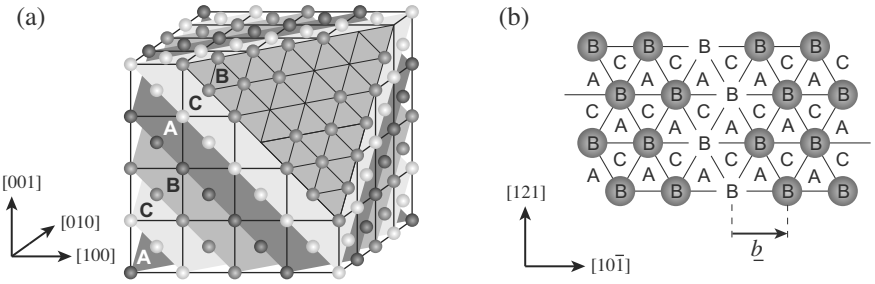

Figure 15. Atom layers in a face centred cubic lattice. A row of atoms is omitted to indicate the first missing atoms of the missing half plane of an edge dislocation.

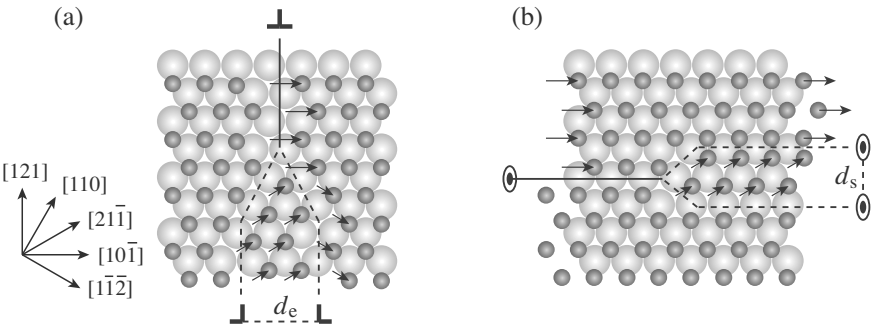

Figure 16. Atom layers adjacent to the glide plane of a perfect/dissociated dislocation of (a) edge and (b) screw character.

but the total energy is lowered because the Burgers vector $\underline{b}_p$ of the partial dislocation (short: partial) is smaller than that of a perfect one. Partials are usually found in pairs of two; this keeps the energy penalty from the stacking fault low. Together such a pair is called a dissociated dislocation. Shockley partial Burgers vectors are of the type $\langle 112 \rangle$ and have the length $b_p = a_0/6^{1/2} = b/3^{1/2}$. The sum of the partial Burgers vectors of a pair equals that of the dissociated perfect dislocation: $\underline{b}_1 + \underline{b}_2 = \underline{b}$. In figure 16 an example is given for the glide plane $\underline{n} = (1\bar{1}1)$ and a screw or edge dislocation with the Burgers vector $\underline{b} = \left(a_0/2^{1/2}\right)(10\bar{1})$ dissociated into $\underline{b}_1 = \left(a_0/6^{1/2}\right)(21\bar{1})$ and $\underline{b}_2 = \left(a_0/6^{1/2}\right)(1\bar{1}\bar{2})$.

It should be noted that the Burgers circuit, which is used to define the Burgers vector, cannot be performed for single partial dislocations unless

the circuit is started and finished in a point in the stacking fault. The region of stacking sequence $ABAB$ around the stacking fault may be considered as a small volume with hexagonal crystal structure. But besides that, partials can be considered as normal dislocations, in particular with respect to all properties deriving from elasticity. In section 1.3 it has been shown that a dislocation with a faulted area on one side of it in the glide plane senses the constant stress $\tau_\gamma = -\gamma_{\text{fault}}/b$ (equation (19)), where γ_{fault} is the energy density of the faulted area. Accordingly, in case of partials with a stacking fault energy γ_{sf}, the stress is $\tau_{\text{sf}} = \pm\gamma_{\text{sf}}/b_{\text{p}}$. The sign of it is such that it drives the partials towards each other. On the other hand, the partials repel each other elastically reciprocal with their distance d, as can be seen from equations (20) or (21) with $z = 0$. The equilibrium distance between partials d_{eq} can be found by equating the repulsive stress with τ_{sf}. Here we have to consider that the partial Burgers vectors are neither normal nor parallel to each other, but they enclose an angle of 60°. As described by equation (22), the dislocations can be decomposed in their screw and edge components. Then the superimposed stress tensors $\boldsymbol{\sigma}^{\text{mixed}}\,(x = d_{\text{eq}}, z = 0)$ for a distance d_{eq} can be subjected to the Peach-Koehler formula (16) to calculate the glide component τ. Equating this with τ_{sf} yields for d_{eq}:

$$d_{\text{eq}} = \frac{\mu b_{\text{p}}^2}{2\pi\gamma_{\text{sf}}} \left[\left(\underline{b}_1^0 \cdot \underline{s}^0\right)\left(\underline{b}_2^0 \cdot \underline{s}^0\right) + \frac{\left(\underline{b}_1^0 \times \underline{s}^0\right) \cdot \left(\underline{b}_2^0 \times \underline{s}^0\right)}{1-\nu} \right]^{-1} \tag{23}$$

When a material with $\nu = 1/3$ is considered with equation (23), edge dislocations are found to dissociate stronger than screw ones by a factor 7/3. This strong difference is caused by the fact that the partials of a pair are in part parallel and antiparallel when decomposed in edge and screw components. The parallel parts repel each other, whereas the antiparallel ones attract. Hence the edge components of the partials of a dissociated edge dislocation repel rather strongly (factor $3/4/(1-\nu)$, for $b_{\text{edge}}/b = 3^{1/2}/2$ with $\alpha = 60°$ for Shockley partials) and attract rather weakly (factor 1/4, for $b_{\text{screw}}/b = 1/2$ with $\alpha = 60°$), whereas in the case of a dissociated screw dislocation, repulsion (factor 3/4 with $\alpha = 30°$) and attraction (factor $1/4/(1-\nu)$) are more balanced and d_{eq} is rather small. The dislocation width is important for the probability of dislocations to cross-slip, as is detailed in section 4.1. Cross-slip means that a screw dislocation leaves its primary glide plane. Perfect screw dislocations have no fixed glide plane, but dissociated ones have a primary glide plane which is defined by the plane of the stacking fault regardless of the dissociation width d_{eq}.

In hexagonal crystals an equivalent stacking fault may occur in the base plane, forming a region with an $ABCABC$ stacking sequence enclosed by

Shockley partials. However, this is only possible when the axis ratio c/a is close to 1.63 because otherwise the stacking fault energy is likely to be high. In body centred cubic crystals dislocation dissociation can even extend in three dimensions.

2 Curved Dislocations

In section 1 on basic dislocation theory it has been emphasized from the start that in general, dislocations are curved and flexible. While several basic dislocation features are understood best by considering straight dislocations, the flexibility should always be kept on mind. As a result of stresses, dislocations can bend locally and thereby change their local line vector $\underline{s}$. The latter thereby changes the local dislocation character (edge/screw), because the Burgers vector $\underline{b}$ is constant.

The degree of flexibility, that is, the stress sensitivity of bending is quite important for the course of events that may happen during plastic deformation. The flexibility is defined by the dislocation's self interaction: a dislocation causes and at the same time senses elastic stresses, including those from itself. Various models have been derived in the past to account for this, with differing complexity and accuracy. Today even the rather complex model for the elastic (self-) interaction of curved dislocations can be utilized in computer programs to simulate dislocation glide in various problems of plasticity. This self interaction model is described in section 2.2. But before that, the simple line tension model is described in detail because it is required for understanding and proper interpretations of simulation results. The description of the line tension model given here differs from other approaches. Unlike other descriptions it is fully consistent and therefore believed to provide a better understanding.

2.1 Line Tension Model

In equation (9) the length specific energy E^* of a straight dislocation with mixed character had been given. The character dependence has been expressed by the directions of the Burgers vector $\underline{b}$ and the line vector $\underline{s}$. Using the angle α between $\underline{b}$ and $\underline{s}$, and $R = r_{\text{shield}}/e$ for simplification, we can write:

$$E^*(\alpha) = \left[\frac{\mu b^2}{4\pi(1-\nu)}\,\sin^2\alpha + \frac{\mu b^2}{4\pi}\,\cos^2\alpha\right] \ln\left(\frac{R}{b}\right) \tag{24}$$

For later reference, the square bracket in equation (24) is called the prelogarithmic energy factor $K_E(\alpha)$. It contains the shear modulus μ and Poisson's ratio ν as elastic constants; elastic isotropy has been assumed in

section 1. In general, $K_E(\alpha)$ is a more complex function (see e.g. (Nembach, 1996) containing more elastic constants, like C_{ijkl}. But for the time being, K_E is considered constant.

Constant line energy With a constant energy per unit length E^*, any object and in particular a dislocation tries to contract itself in order to reduce the free energy. The energy of a segment described by $\underline{\Delta s}$ is $E^*|\underline{\Delta s}|$. This causes the force $\underline{F} = -\underline{\nabla}\,(E^*\Delta s)$, which obviously points along $\underline{\Delta s}$ and has the magnitude $F = E^*$. This means that the dislocation behaves like a string under constant tension in this model. This knowledge can be used to evaluate the force equilibrium in the middle point of figure 17, which holds the force caused by both adjacent dislocation arcs in their given circular shape. The x-components of the forces from the arcs, $F_x = \pm E^* \cos\varphi$, cancel each other; the superimposed y-component is $F_y = 2E^* \sin\varphi$. Assuming small angles φ for simplicity (this is not a necessary condition) such that $\sin\varphi \approx \varphi$, and expressing φ by the arc length L and the curvature radius R_c $(\varphi = L/R_\mathrm{c})$, we find $F_y = E^* L/R_\mathrm{c}$. This is the force that the arcs cause in the middle point. But as mentioned above, the dislocation arcs would try to contract; the same force F_y is needed for each point or arc to keep the dislocation in its shape. Over the length L, the required stress is known to be $\tau_\mathrm{ext} = F_y/(bL)$ (stress definition in section 1.3). Since a stress equilibrium must be fulfilled and no other stresses are involved, this external stress must equal the stress $\tau_{\mathrm{self}-E}$ that the dislocation produces on itself in every point. Altogether this yields:

$$\tau_{\mathrm{self}-E} = \frac{E^*}{b\ R_\mathrm{c}} \tag{25}$$

According to equation (25) the dislocation's self-interaction depends only on the curvature $1/R_\mathrm{c}$, which is a very local property. This is only a rough approximation, as is seen later. In addition, it must be emphasized here that equation (25) holds only for the rather hypothetical case of a constant line energy E^*. The effects of $E^*(\alpha)$ are described later on; before that, we take a look at the importance of a dislocation's flexibility or rigidity in strengthening models. The rigidity is represented here by E^*, and later more accurately by the line tension S.

Simple Strengthening Models Strengthening models relate properties of obstacles, which impede dislocation glide, to the critical stress required to enforce dislocation glide to continue. The simplest but still important strengthening model is that of Orowan (Orowan, 1934). It assumes that dislocation glide in a plane is impeded by obstacles which, for any reasons,

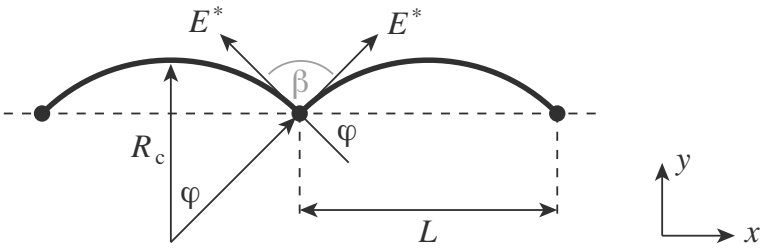

Figure 17. Force on the middle point: the x-components $\pm E^*\cos\varphi$ of the left and right dislocation arcs cancel each other, the y-components $E^*\sin\varphi$ add up. Often the cusp angle $\beta = \pi - 2\varphi$ is used instead of φ.

cannot be cut through by dislocations: the obstacles are impenetrable. Dislocations can still overcome these obstacles provided that an external stress τ_{ext} exceeds some critical stress τ_{Orowan}, as sketched in figure 18(a). Between obstacles, in a static configuration (no motion) τ_{ext} equals $\tau_{\text{self}-E}$ because no other stresses are involved. Hence according to equation (25) τ_{ext} will cause a curvature with the radius $R_{\text{c}} = E^*/(b\tau_{\text{ext}}))$. When τ_{ext} is high enough such that R_{c} is equal or just below the free space $L_{\text{cc}} - 2R$ between the obstacles, the angle φ (see figure 17) will reach $\pi/2$, (or, $\beta = 0$). This defines the Orowan stress

$$\tau_{\text{Orowan}} = \frac{E^*}{b\,(L_{\text{cc}} - 2R)} \tag{26}$$

where R and L_{cc} are the obstacle radius and their centre-to-centre spacings, respectively. At $\tau_{\text{ext}} = \tau_{\text{Orowan}}$, the dislocation arcs are driven forwards by the force $(L_{\text{cc}} - 2R)b\tau_{\text{ext}}$. This force equals $2E^*$ and therefore is just enough to keep the length of the two dislocation arcs that touch one obstacle. When $\tau_{\text{ext}} > \tau_{\text{Orowan}}$ the dislocation length is increased, and the dislocation overcomes the obstacles by circumventing them. Thereby parts of the dislocation with opposite line vectors annihilate each other, and Orowan loops around the particles are left behind, as indicated in figure 18(b). Equation (26) describes the strengthening effect that the impenetrable obstacles give to the material in terms of b, of the obstacle's geometrical parameters L_{cc} and R, and of E^*. For the case $R \ll L_{\text{cc}}$, only the obstacle spacing L_{cc} is of importance, but no obstacle parameters. L_{cc} may be expressed in more useful terms, like a volume density of obstacles. But here only the importance of E^* is emphasized: apart from geometrical factors, the strengthening effect of the obstacles depends on the rigidity E^*, which is a pure dislocation

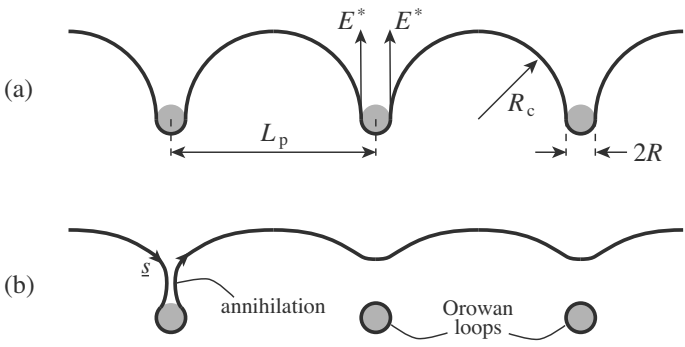

Figure 18. A dislocation overcoming an equidistant row of impenetrable obstacles.

property.

Another simple but important strengthening model is that of Friedel (Friedel, 1964), and derivations thereof. Here the obstacles are not impenetrable, so that they can only hold a finite maximum force $F_{\max}$. However, we assume the obstacle to be point-like ($R = 0$) for simplification. In the terms of figure 17, the finite force $F_{\max}$ means that the range of possible angles is reduced to $\sin\varphi < F_{\max}/(2E^*)$, or $\cos(\beta/2) < F_{\max}/(2E^*)$. This influences the effective number of obstacles that prevent dislocation glide: in a random field of point obstacles, an extremely rigid, i.e. straight dislocation touches only very few obstacles, whereas a rather flexible dislocation ($E^* \to F_{\max}/2$) will touch many. To derive the effect of this, we consider the configurations given in figure 19, where a dislocation first lies behind a row of three equidistant obstacles and then breaks free from the obstacle in the middle. It then bows out until it touches another obstacle in a random obstacle arrangement, thereby sweeping the area A. Before and after the break-through the curvature radius R_c is the same because the external stress τ_{ext} is constant.

Assuming a parabolic dislocation arc, for simplicity, instead of a circular one (restricting the model to low angles φ) before and after break-through, the following purely geometrical relation can be derived:

$$A = 2\frac{2}{3}\,(1 - 2/8)\;\; L_F \cdot h = L_F \cdot h \quad \text{with} \quad h = \frac{1}{2R_c} L_F^2 \tag{27}$$

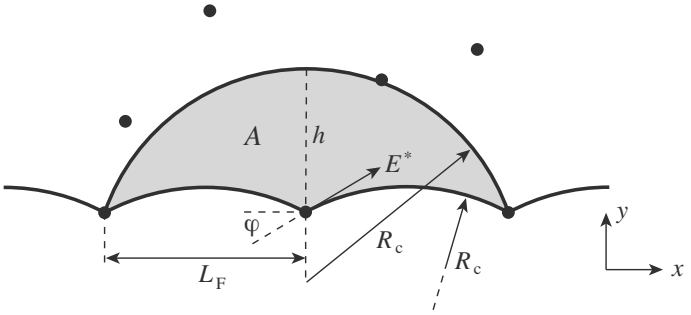

Figure 19. Geometry for Friedel's strengthening model. The grey area A is swept when the dislocation breaks through the obstacle in the middle, until the next obstacle is found.

Here so far, none of the variables A, L_F, and h are known. But it is known that on average during dislocation glide, one new obstacle must be found by the dislocation after it has overcome another. This means that $1/A$ equals the area density of obstacles, c, which is fixed and can be measured, or $A = L_\mathrm{square}^2$, where L_square denotes the square lattice spacing. This is the shortest distance between obstacles if they were arranged in a square lattice. Next, the force equilibrium in the obstacles is applied: at the critical stress τ_Friedel, the force $bL_\mathrm{F}\tau_\mathrm{Friedel}$ acts on one dislocation arc of the length L_F and hence on the obstacles, so we get $F_\mathrm{max} = bL_\mathrm{F}\tau_\mathrm{Friedel}$. Finally, from the stress equilibrium between the obstacles we know that, like in the Orowan model above, $\tau_\mathrm{Friedel} = \tau_{\mathrm{self}-E} = E^*/(bR_\mathrm{c})$. With these considerations, equation (27) can be resolved for the length L_F, called the Friedel length:

$$L_\mathrm{F} = \frac{b}{\sqrt{ck}} = \frac{L_\mathrm{square}}{\sqrt{k}} \quad \text{with} \quad k = \frac{F_\mathrm{max}}{2E^*} \tag{28}$$

Here k denotes a relative obstacle strength. If the obstacles are weak ($\mathrm{F}_\mathrm{max} \ll 2E^*$, or $k \ll 1$), L_F is large compared to the square lattice spacing L_square, which is a constant parameter given by the obstacle array. This means that the dislocation touches only very few obstacles when they are weak, or, as indicated above, when the dislocation is very rigid and remains straight. This emphasizes the importance of the line tension model, because the line energy is needed to rate the obstacle force F_max, even in simulations in which the line tension model is not used at all. However, it must be stressed again that it had been assumed that E^* is constant. If E^* is a function of the dislocation character, often (but not always) the line tension $S(\alpha)$ introduced in section 2.1 is to be used instead of $E^*(\alpha)$. With L_F and

k from equation (28), the strengthening effect τ_{Friedel} of the obstacles can finally be written as:

$$\tau_{\text{Friedel}} = \sqrt{k}\ \tau_{\max} \quad \text{with} \quad \tau_{\max} = \frac{F_{\max}}{bL_{\text{square}}} \tag{29}$$

At a given obstacle spacing L_{square}, the strengthening effect of obstacles obviously increases with $F_{\max}$ with a power of 3/2, but only up to $k = 1$. When $F_{\max} \geq E^*$, only the obstacle spacing is of importance, as seen in the Orowan model.

Line Torque So far it has been shown that a dislocation with the length specific energy E^* is under tension with the force $F = E^*$ along its line direction. The stress $\tau_{\text{self}-E}$ (equation (25)), and the force $\Delta F_E = b\tau_{\text{self}-E}\Delta s$ normal to the segment vector $\underline{\Delta s}$ resulted from this assumption. This holds for a constant line energy E^*. But usually E^* is a function of the dislocation character, indicated by the angle α between Burgers- and line vector. From $E^*(\alpha)$, a dislocation segment of length Δs senses a torque ΔM that attempts to rotate the segment such that its energy $(E^*\Delta s)$ is lowered:

$$M(\alpha) = -\left.\frac{\partial(E^*\Delta s)}{\partial\alpha}\right|_{\Delta s} \quad \text{or} \quad M^*(\alpha) = -\frac{\partial E^*}{\partial\alpha} \tag{30}$$

where $M^* = \Delta M/\Delta s$ is a length specific torque, called line torque in analogy to the line energy. Here Δs is assumed to be constant because the effect of a length change has already been covered by $\tau_{\text{self}-E}$ in section 2.1. The torque tries to rotate the segment, but for the most part this is prevented by the neighbouring segments since they want to rotate in the same direction when they are close and sense the same torque. In figure 20 three segments with the same lengths Δs are plotted. They sense slightly varying torques $\Delta M^{(-1)}$, $\Delta M^{(0)}$, and $\Delta M^{(+1)}$ resulting from a varying M^*. The torques ΔM result in forces in the segments' end points. Between the segments (0) and (+1), the sum of forces in y-direction is $\Delta F_M = \left(\Delta M^{(0)}/\Delta s\right) - \left(\Delta M^{(+1)}/\Delta s\right) = M^{*(0)} - M^{*(+1)}$. With the distance between the connections being the segment lengths Δs, the corresponding stress is

$$\tau_M = \frac{M^{*(0)} - M^{*(+1)}}{b\ \Delta s} = -\frac{1}{b}\frac{\mathrm{d}M^*}{\mathrm{d}s} \tag{31}$$

The second part of equation (31) is the transition to infinitesimally short. For equation (31) no assumption has been used, so far, about the cause of the difference between $M^{*(0)}$ and $M^{*(1)}$, or for $\mathrm{d}M^*/\mathrm{d}s$. The line torque M^* may have an explicit dependence on the location $\underline{x}$, like in the case of

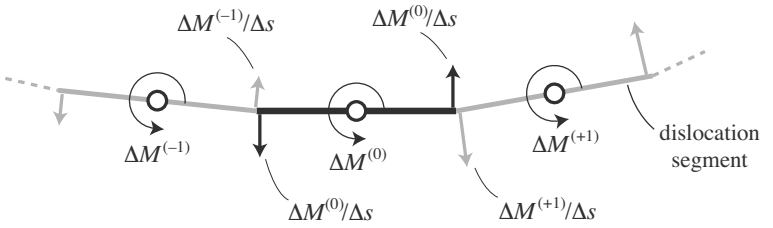

Figure 20. A dislocation cut into short segments of length Δs. When a line torque M^* with a gradient acts on the dislocation, a non-vanishing force results in the segments' connections.

elastic interaction between a dislocation and a size mismatched particle with a fixed location $\underline{x}_\mathrm{p}$ (Mohles, 1997). Another possibility is the dependence of M^* on α:

$$\frac{\mathrm{d}M^*}{\mathrm{d}s} = \frac{\partial M^*}{\partial s} + \frac{\partial M^*}{\partial \alpha}\frac{\mathrm{d}\alpha}{\mathrm{d}s} \tag{32}$$

When the dislocation has the curvature $1/R_\mathrm{c}$, then going from s to $s + \Delta s$ along the dislocation rotates the local line vector direction $\underline{s}^0$ by the angle $\Delta s/R_\mathrm{c}$, and α changes by the same amount. In figure 20 a slight curvature is indicated, but R_c and $\Delta\alpha$ are not indicated because $R_\mathrm{c} \gg \Delta s$. With $\Delta\alpha = \Delta s/R_\mathrm{c}$, M^* from equation (30), and $\partial M^*/\partial s = 0$ (this is not used here) we get for τ_M:

$$\tau_{\mathrm{self}-M} = +\frac{1}{b}\frac{\partial^2 E^*(\alpha)}{\partial^2 \alpha}\frac{1}{R_\mathrm{c}} \tag{33}$$

This ist the stress that a dislocation poses upon itself only because its line energy $E^*(\alpha)$ is character dependent, and because this results in a torque. Usually, $\tau_{\mathrm{self}-M}$ has the same order of magnitude as $\tau_{\mathrm{self}-E}$. But unlike $E^*(\alpha)$ itself, its derivative $\partial^2 E^*/\partial\alpha^2$ can be negative.

Line Tension Both the stresses $\tau_{\mathrm{self}-E}$ and $\tau_{\mathrm{self}-M}$ arise from the line energy E^*. But they consider different, independent forces: $\tau_{\mathrm{self}-E}$ is derived from forces along the line vector $\underline{s}$, $\tau_{\mathrm{self}-M}$ from those normal to $\underline{s}$. The total self interaction stress τ_line — in the line tension model — is, therefore, superimposed of both $\tau_{\mathrm{self}-E}$ and $\tau_{\mathrm{self}-M}$:

$$\tau_\mathrm{self} = \frac{S(\alpha)}{b\,R_\mathrm{c}} \quad \text{with} \quad S(\alpha) = E^*(\alpha) + \frac{\partial^2 E^*(\alpha)}{\partial^2 \alpha} \tag{34}$$

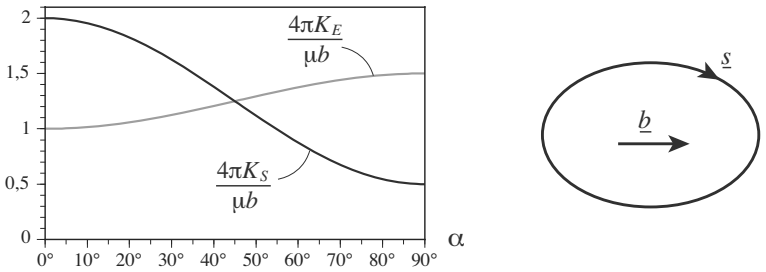

Figure 21. Pre-logarithmic factors K_E and K_S as functions of the dislocation character for $\nu = 1/3$, and the corresponding equilibrium shape of a dislocation loop.

$S(\alpha)$ is called the line tension and is actually a force, like $E^*(\alpha)$. The relation (34) between S and E^* holds in general, including elastically anisotropic materials. S is the true rigidity in the line tension model, not E^*. Consider for instance the pre-logarithmic factor $K_E(\alpha)$ of E^* for an isotropic material as given in equation (24), and its counterpart $K_S(\alpha)$ for the line tension S:

$$K_E = \frac{\mu b^2}{4\pi}\left(\cos^2\alpha + \frac{\sin^2\alpha}{1-\nu}\right) \tag{35a}$$

and

$$K_S = \frac{\mu b^2}{4\pi}\left(\frac{1+\nu}{1-\nu}\cos^2\alpha + \frac{1-2\nu}{1-\nu}\sin^2\alpha\right) \tag{35b}$$

As can be seen in figure 21, K_E and hence E^* are larger for edge than for screw dislocations, but for K_S and S, the opposite holds. This means that screw dislocations are stiffer than edge ones: when a screw dislocation is bent, edge components are generated, which needs much energy. On the other hand, when an edge dislocation is bent, only the lower energy screw components are generated. Accordingly, an equilibrium dislocation loop with a constant self-stress τ_{line} is elongated in the direction of the Burgers vector.

It is frequently claimed or assumed that S were the actual force along the dislocation line, but this perception is misleading and involves inconsistencies, as demonstrated below. The line tension model may be seen as inconsistent, anyway, in light of the more accurate self interaction model (section 2.2). But since the line tension is used for interpretations of simulations using the dislocation self-interaction, inconsistencies in the line tension model may lead to misinterpretations.

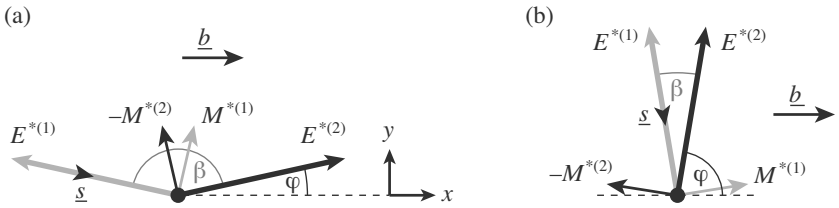

Figure 22. Forces from a dislocation on a point obstacle.

Forces on Obstacles In figure 22 all forces from a dislocation exerted on a point obstacle are plotted for two cases: large and small cusp angles β. The forces are E^* along the dislocation and M^* normal to it. The opposite forces of the line torque M^* are not plotted; they are distributed along the dislocation line in $b\tau_{\text{self}-M}$ (see above). Equation (36) describes this sum of forces in terms of $\varphi = (\pi - \beta)/2$.

$$F_y = \sin\,\varphi \left(E^{*(1)} + E^{*(2)}\right) + \cos\,\varphi \left(M^{*(1)} - M^{*(2)}\right) \tag{36}$$

Note that $M^{*(2)}$ in equation (36) and in figure 22 has a negative sign; this is because this force acts on the left side of a dislocation segment, and not on the right as $M^{*(1)}$. This is consistent with equation (31). Yet in figure 22, both force vectors $M^{*(1)}$ and $-M^{*(2)}$ point in positive y-direction against the point obstacle. This is caused by the fact that $M^*(\alpha)$ changes its sign as the angle α between Burgers and line vector changes from $-\varphi$ to $+\varphi$ in the obstacle; the sign of M^* is always so that M^* tries to rotate the dislocation into screw character, which has the lowest energy E^*.

The only difference between figures 22(a) and 22(b) lies in the line vector $\underline{s}$, such that $\varphi \to 0$ in figure 22(a) as for weak obstacles, and $\varphi \to \pi/2$ in 22(b) as for strong obstacles. In the latter case, the force contributions $M^{*(1)}$ and $-M^{*(2)}$ cancel each other (figure 22(b)). Hence the total force F_y pulling on the obstacle equals $2E^*$: in case of strong obstacles, like for Orowan's strengthening model (see above), the line energy is the appropriate force.

In contrast, for weak obstacles $M^{*(1)}$ and $-M^{*(2)}$ add up, and they add to the force $2E^*\sin\varphi$. With $\varphi \to 0$, $\cos\varphi = 1$, and $E^{*(1)} = E^{*(2)} = E^*$, equation (36) can be written as

$$F_y = 2E^*\,\sin\,\varphi - \frac{\Delta M^*}{\Delta\alpha}\Delta\alpha \tag{37}$$

Here $-\Delta M^*$ replaces $M^{*(1)} - M^{*(2)}$, and $\Delta\alpha$ is just inserted without damage. Then $(\Delta M^*/\Delta\alpha)$ can be read as the first derivative of $M^*(\alpha)$. While crossing the particle, the line vector $\underline{s}$ changes by $\Delta\alpha = 2\varphi$ (figure 22(a)). Now inserting this and replacing φ by $\sin\varphi$ ($\varphi \to 0$), and using $M^* = -\partial E^*/\partial\alpha$ (equation (30)), we get:

$$F_y = 2 \sin \varphi \left(E^* + \frac{\partial^2 E^*}{\partial \alpha^2} \right) \tag{38}$$

The bracket in equation (38) is obviously identical with the line tension S as introduced in equation (34). Hence equation (38) can be read as if in figure 22(a), two forces $S^{(1)}$ and $S^{(2)}$ acted on the obstacle instead of $E^{*(1)}$ and $E^{*(2)}$, and no forces M^*. Hence, for weak obstacles, the line tension S may be considered as the appropriate force acting on an obstacle. But this perception is not consistent because for strong obstacles, E^* is the appropriate force (see above). This means that at some point in the transition from weak to strong obstacles, a 'switch' from S to E^* would be needed if the line torque were to be disregarded. In case of obstacles of medium strength, around $\varphi = \pi/4$, either force S or E^* would only be an approximation. It seems more useful to keep a fully consistent view in mind, in which the true forces, namely the line energy E^* and the line torque M^*, are considered as in equation (36). With these, even the force components F_x, which act on the obstacle in figure 22 from the sides, can be treated correctly with an equation equivalent to (36). Such side forces F_x may be larger than F_y and hence be critical for overcoming an obstacle.

While the line tension model as described here is consistent and exact for a linear object with a line energy E^*, it is still only an approximation for dislocations because they have a long-ranged self-interaction.

2.2 Dislocation Self-Interaction

Each infinitesimal piece of a dislocation somehow interacts elastically with every other piece. This can be stated, as seen later, in spite of the fact that a single piece of dislocation does not exist. In principle the interaction goes through every point in space; however, when an elastically homogeneous material is assumed, the latter complication is dropped. Since elasticity is linear, the stress and strain contributions caused by all dislocation pieces can be calculated separately for an arbitrary point in space and then superimposed later. This is Green's principle, which is usually well known and used in electrodynamics or heat conduction. In case of elasticity, a Green's displacement tensor is required instead of a Green's function.

Green's displacement tensor The general elastic stress equilibrium can be written as $\underline{\nabla} \cdot \boldsymbol{\sigma} + \underline{f} = 0$, where $\boldsymbol{\sigma}$ is a general stress tensor, $\underline{f}$ is a volume force (force per unit volume) and $\underline{\nabla}$ denotes the gradient operator. With the definition of a strain $\boldsymbol{\sigma}$ in terms of a displacement $\underline{u}$, $\varepsilon_{kl} = \left(\partial u_k/\partial x_l + \partial u_l/\partial x_k\right)/2$, and Hooke's law $\sigma_{ij} = C_{ijkl}\varepsilon_{kl}$, the stress equilibrium can be written as a relation between between a volume force $\underline{f}$ and the corresponding displacements $\underline{u}$:

$$C_{ijkl}\frac{\partial^2 u_k}{\partial x_j \partial x_l} + f_i = 0 \tag{39}$$

Here C_{ijkl} denotes the 4th grade tensor of elastic constants, and Einstein's summation convention over equal indices is applied. The subsequent derivation is restricted to an elastically isotropic medium. For this, the tensor of elastic constants can be written in terms of the shear modulus μ and the Poisson ratio ν: $C_{ijkl} = \left[\delta_{ik}\delta_{jl} + \delta_{il}\delta_{jk} + (2\nu/(1-2\nu))\,\delta_{ij}\delta_{kl}\right]\mu$, where δ_{ij} is the Kronecker symbol with $\delta_{ij} = 1$ if $i = j$, and $\delta_{ij} = 0$ if $i \neq j$. Using this in equation (39) and considering a volume force $\underline{f} = (\delta(\underline{r}), 0, 0)$ pointing only to the x_1-direction, we can write:

$$\begin{aligned}
\frac{\mu}{1-2\nu}\frac{\partial}{\partial x_1}(\underline{\nabla}\cdot\underline{u}) + \mu\,\underline{\nabla}^2 u_1 + \delta(\underline{r}) &= 0 \\
\frac{\mu}{1-2\nu}\frac{\partial}{\partial x_2}(\underline{\nabla}\cdot\underline{u}) + \mu\,\underline{\nabla}^2 u_2 &= 0 \\
\frac{\mu}{1-2\nu}\frac{\partial}{\partial x_3}(\underline{\nabla}\cdot\underline{u}) + \mu\,\underline{\nabla}^2 u_3 &= 0
\end{aligned} \tag{40}$$

This is a set of coupled differential equations for the displacement $\underline{u}$ caused by the 'force' $\delta(\underline{r})$, which acts only in x_1-direction and only in the origin $r = 0$ due to the delta function $\delta(\underline{r})$. This function has the dimension m^{-3} instead of Nm^{-3} for a volume force because by definition, a Green's function is the reaction of a system to the inhomogeneity of the δ-function. With some help from potential theory, equation (41) can be solved analytically (e.g. (Hirth and Lothe, 1992)). The solution is $\underline{u}_1$, with the subindex 1 indicating the direction of the force used. Repeating this for forces in x_2- and x_3-directions, we find the matrix u_{ij}, where i is the index for the displacement component and j that for the force component. This is already Greens displacement tensor. Because of the choice of the δ-function as the inhomogeneity in equation (40), the dimension of u_{ij} is not that of a displacement (m) but mN^{-1}. Therefore, we rename the u_{ij} into the usual name for a Greens function or tensor, G_{ij}.

$$G_{ij} = \frac{1}{8\pi\mu}\left(\delta_{ij}\underline{\nabla}^2 r - \frac{1}{2(1-\nu)}\frac{\partial^2 r}{\partial x_i \partial x_j}\right) \tag{41}$$

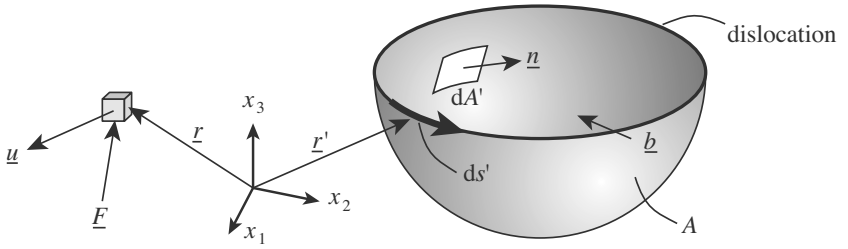

Figure 23. A dislocation is generated by a cutting procedure along the area A in the presence of a test force $\underline{F}$ in the point $\underline{r}$ to derive the dislocation's displacements there.

As is the idea for any Green's function, the displacement caused by a given distribution of volume forces $\underline{f}(\underline{r})$, can then be found by integration over the volume:

$$u_i(\underline{r}) = \int G_{ij}\,(\underline{r} - \underline{r}')\,f_j\,(\underline{r}')\;\mathrm{d}V' \tag{42}$$

Dislocation stress due to Peach and Koehler To derive the stress caused by an arbitrarily curved dislocation, the energy required to generate this dislocation by the cutting procedure described in section 1.1 is considered in the presence of a test force $\underline{F}$ acting in an arbitrary location $\underline{r}$. The cutting area A can be arbitrarily curved, as depicted in figure 23. The test force contributes the energy

$$W = \underline{F} \cdot \underline{u}(\underline{r}) = F_m u_m(\underline{r}) \tag{43}$$

to the dislocation's creation, where $\underline{u}$ is the displacement caused by the dislocation. On the other hand, this energy can also be expressed by the stress $\boldsymbol{\sigma}^F$ caused by $\underline{F}$ and the displacement in the area A during the dislocation's generation. In A, the displacements are obviously given by the Burgers vector b.

$$W = -\int_A b_i\;\sigma_{ij}^F\,(\underline{r}' - \underline{r})\;\mathrm{d}A'_j \tag{44}$$

The sign in equation (44) is negative because F helps in the dislocation creation. With Hooke's law, $\sigma_{ij} = C_{ijkl}\varepsilon_{kl}$, and the strain definition $\varepsilon_{kl} = (\partial u_k/\partial x_l + \partial u_l/\partial x_k)/2$, the stress $\boldsymbol{\sigma}^F$ can be expressed by the displacement $\underline{u}^F$ that F causes. Due to the symmetry of C_{ijkl} ($C_{ijkl} = C_{ijlk}$), $\boldsymbol{\sigma}$ is simplified to $\sigma_{ij} = C_{ijkl}\partial u_k/\partial x_l$. Since $\underline{F}$ acts in the point $\underline{r}$, the displacements $\underline{u}^F$ are known from Green's displacement tensor: $\underline{u}^F = \underline{F} \cdot \boldsymbol{G}$.

Hence equation (44) can be rewritten as

$$W = -F_m \int_A b_i \, C_{ijkl} \frac{\partial G_{km}\left(\underline{r}' - \underline{r}\right)}{\partial x_l'} \, \mathrm{d}A_j' \tag{45}$$

Now by comparing equation (45) with (43), the displacement components u_m caused by the dislocation in the point $\underline{r}$ is found. Subsequently, $\underline{r}$ is chosen as the origin. To yield the strain tensor, $\underline{u}$ is differentiated with respect to a general direction x_s:

$$\frac{\partial u_m}{\partial x_s} = \int_A b_i \left(C_{ijkl} \frac{\partial^2 G_{km}\left(\underline{r}'\right)}{\partial x_s' \partial x_l'} \right) \mathrm{d}A_j' \tag{46}$$

Here it has been used that $\partial/\partial x_s = -\partial/\partial x_s'$. Multiplying equation (46) with C_{ijms} yields the stress tensor σ_{ij} of the dislocation, but this would be an expression of the cutting area A, which is unhandy. Moreover, A has no physical meaning; a line integral along the dislocation line is needed. In the point of strain observation (the origin), which is not on the dislocation itself, there are no volume forces. Therefore, by using the general stress equilibrium of equation (39) with $f_i = 0$, the bracket in equation (46) can be rewritten such that

$$\frac{\partial u_m}{\partial x_s} = b_i \, C_{ijkl} \int_A \left(\frac{\partial^2 G_{km}\left(\underline{r}'\right)}{\partial x_s' \partial x_l'} \mathrm{d}A_j' - \frac{\partial^2 G_{km}\left(\underline{r}'\right)}{\partial x_j' \partial x_l'} \mathrm{d}A_s' \right) \tag{47}$$

This expression can be subjected to Stoke's theorem to be converted into a line integral along the dislocation:

$$\frac{\partial u_m}{\partial x_s} = \epsilon_{jsn} \, b_i \, C_{ijkl} \oint \frac{\partial G_{km}\left(\underline{r}'\right)}{\partial x_l'} \mathrm{d}x_n' \tag{48}$$

Here ϵ_{ijk} is the Einstein permutation operator with $\epsilon_{ijk} = 0$ except for $\epsilon_{123} = \epsilon_{231} = \epsilon_{312} = 1$ and $\epsilon_{321} = \epsilon_{213} = \epsilon_{132} = -1$. Equation (48) is generally valid for anisotropic materials. However, here Green' displacement tensor G_{ij} for isotropic materials of equation (41) and the isotropic constants $C_{ijkl} = \left(\delta_{ik}\delta_{jl} + \delta_{il}\delta_{jk} + (2\nu/(1-2\nu))\delta_{ij}\delta_{kl}\right)\mu$ are inserted, and Hooke's law is applied to finally get the stress $\boldsymbol{\sigma}$ of an arbitrary dislocation loop:

$$\begin{aligned} \sigma_{\mathrm{disl},\alpha\beta} = &-\frac{\mu}{8\pi} \oint_C b_m \frac{\partial}{\partial x_i'} \underline{\nabla}'^2 r' \left(\epsilon_{im\alpha} \mathrm{d}x_\beta' + \epsilon_{im\beta} \mathrm{d}x_\alpha' \right) - \\ &- \frac{\mu}{4\pi(1-\nu)} \oint_C b_m \, \epsilon_{imk} \frac{\partial}{\partial x_i'} \left(\frac{\partial^2 r'}{\partial x_\alpha' \partial x_\beta'} - \delta_{\alpha\beta} \underline{\nabla}'^2 r' \right) \mathrm{d}x_k' \end{aligned} \tag{49}$$

where $r' = \left(x_1'^2 + x_2'^2 + x_3'^2\right)^{1/2}$ is the length of the vector from the origin to a point on the dislocation curve C. Equation (49) is a useful result, as is seen later on, and it seems as if the integrand defined the stress contribution of a dislocation segment $\underline{\mathrm{d}x}$. But the integrand is not unequivocal; one alternative is Brown' stress formula (Brown, 1964), (Brown, 1967), (Hirth and Lothe, 1992).

Dislocation stress due to Brown For the derivation of Brown's stress formula of a curved dislocation we start with equation (46), and the point of stress observation in the origin, $\underline{r} = 0$. When we insert Green's tensor G_{km} of equation (41) and remove all primes for simplicity, the result can be written as

$$\frac{\partial u_m}{\partial x_s} = \int_A \frac{a_{ms}\left(x_1/r, x_2/r\right)}{r^3} \mathrm{d}x_1 \mathrm{d}x_2 \tag{50}$$

where the term a_{ms} is just used as an abbreviation; it has been formulated such that it depends on the dimensionless terms x_i/r. The term a_{ms}/r^3 satisfies Euler's identity of -3rd degree, which means that:

$$\frac{a_{ms}}{r^3} = -\frac{\partial}{\partial x_1}\left(\frac{x_1}{r^3} a_{ms}\right) - \frac{\partial}{\partial x_2}\left(\frac{x_2}{r^3} a_{ms}\right) \tag{51}$$

This can be verified with a_{ms} defined by the comparison of equation (50) with the combination of equations (46) and (41). Subsequently, this particular function a_{ms} is not used. Instead, it is only assumed that $\partial u_m/\partial x_s$ can be expressed as in equation (50) with a function a_{ms} that is yet unknown, but that satisfies Euler's identity of equation (51). The advantage of this procedure is that the assumption of elastic isotropy used for G_{km} in equation (41) is dropped. This allows for the consideration of elastically anisotropic materials. Using equation (51) and Green's theorem, equation (50) can be rewritten as an integral along the dislocation line C:

$$\frac{\partial u_m}{\partial x_s} = \oint_C \frac{1}{r^2}\left(\frac{x_1}{r}\frac{\mathrm{d}x_2}{\mathrm{d}s} - \frac{x_2}{r}\frac{\mathrm{d}x_1}{\mathrm{d}s}\right) a_{ms}\left(x_1/r, x_2/r\right) \mathrm{d}s \tag{52}$$

The terms x_1/r, x_2/r, $\mathrm{d}x_1/\mathrm{d}s$, and $\mathrm{d}x_2/\mathrm{d}s$ can be interpreted as $\cos(\theta)$, $\sin(\theta)$, $\cos(\varphi)$ and $\sin(\varphi)$, respectively, with the meanings of the angles φ and θ given in figure 24(a). Using these angles, equation (52) can be rewritten as:

$$\frac{\partial u_m}{\partial x_s} = \oint_C \frac{1}{r}\frac{\sin(\theta-\varphi)}{r}\, a_{ms}(\theta)\mathrm{d}s \tag{53}$$

As mentioned above, the function $a_{ms}(\varphi)$ is still considered as unknown. Subsequently, the known stress of a straight dislocation (section 1.2) is used

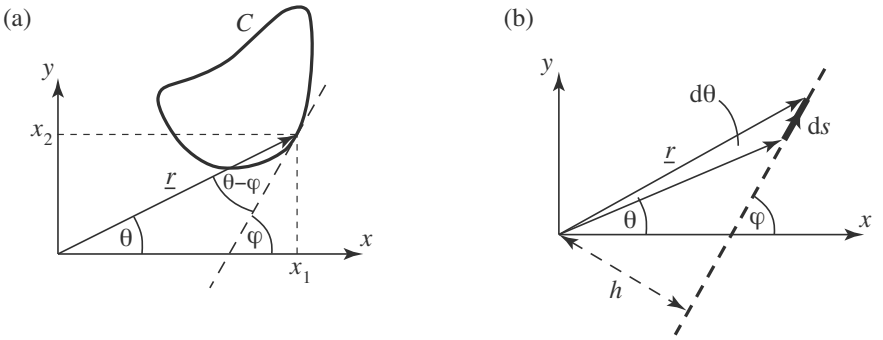

Figure 24. Geometrical relations: (a) angles, (b) tangential segment ds.

to find $a_{ms}(\theta)$. When we consider a straight dislocation, as in figure 24(b), the distance $h = r \cdot \sin(\theta - \varphi)$ is constant, and $1/h$ can be taken out of the integral. Further using the relation $\mathrm{d}s = r/\sin(\theta - \varphi)) \cdot \mathrm{d}\theta$ we can write:

$$\frac{\partial u_m}{\partial x_s} = \frac{A_{ms}(\varphi)}{h} = \frac{1}{h}\int_{\varphi}^{\varphi+\pi} \sin(\theta - \varphi)\, a_{ms}(\theta)\mathrm{d}s \tag{54}$$

The defined integral $A_{ms}(\varphi)$ is still unknown; however, its second derivative with respect to φ can be written as:

$$\frac{\partial^2 A_{ms}}{\partial \varphi^2} = 2a_{ms}(\varphi) - \int_{\varphi-\pi}^{\varphi} \sin(\theta - \varphi)\, a_{ms}(\theta)\mathrm{d}s \tag{55}$$

Here Leibniz' formula has been used because the limits of integration depend on φ. Combining equations (54) and (55) yields a simple relation between a_{ms} and A_{ms}:

$$a_{ms}(\varphi) = \frac{1}{2}\left(A_{ms} + \frac{\partial^2 A_{ms}}{\partial \varphi^2}\right) \tag{56}$$

This relation can be inserted for in equation (53), so that the strain $\varepsilon_{ms} = \partial u_m/\partial x_s$ of a generally curved dislocation is expressed by the still unknown expression $A(\theta) + \partial^2 A/\partial\theta^2$ of piecewise straight segments ds. Applying Hooke's law leads to

$$\sigma_{ij} = \oint_C \frac{\sin(\theta - \varphi)}{r^2}\left[B_{ij}(\theta) + \frac{\partial^2 B_{ij}}{\varphi^2 \theta}\right]\mathrm{d}s \tag{57}$$

with the tensor $B_{ij} = C_{ijms}A_{ms}/2$. Finally, considering the shear stresses in a glide system with Burgers vector $\underline{b}$ and glide plane $\underline{n}$ by applying

the Peach-Koehler-formula (41) and comparing these stresses with those of straight dislocations given in section 1.2, the tensor B_{ij} is identified, and the shear stress of the curved dislocation is found to be

$$\tau_{\mathrm{disl}} = \underline{b}^0 \, \boldsymbol{\sigma} \, \underline{n}^0 = \oint_C \frac{\sin(\theta - \varphi)}{r^2} K_S(\theta) \mathrm{d}s \tag{58}$$

where $K_S(\theta)$ is the pre-logarithmic factor for the line tension of a straight dislocation: $K_S = K_E + \partial^2 K_E / \partial \theta^2$. For the case of elastic isotropy, the function $K_S(\theta)$ is given by equation (35b), but equation (58) is also valid in case of anisotropy: isotropy has not been assumed, not even by using the isotropic Green's tensor G_{km} of equation (41).

Dislocation segments To utilize a stress formula like (49) or (58) in computer simulations of dislocation motion, a dislocation must be cut into segments, like in case of a polygon. Hence the line integrals are decomposed into contributions from segments k connecting the points A and B at $\underline{r}^A$ and $\underline{r}^B$:

$$\sigma_{ij} = \sum_k \sigma_{ij}^{\mathrm{seg}} \left(\underline{r}_k^A, \underline{r}_k^B \right) \quad \text{with}$$

$$\sigma_{ij}^{\mathrm{seg}} = \int_A^B I_{ij} \mathrm{d}s = \sigma_{ij}^{\mathrm{semi}} \left(\underline{r}^B, \underline{s}^0 \right) - \sigma_{ij}^{\mathrm{semi}} \left(\underline{r}^A, \underline{s}^0 \right) \tag{59}$$

where I_{ij} is the integrand of (49) or (58). The integral is expressed as the contributions from the two integration limits; these may be seen as the stress contributions $\boldsymbol{\sigma}^{\mathrm{semi}}$ from semi-segments. Besides on $\underline{r}$, $\boldsymbol{\sigma}^{\mathrm{semi}}$ depends on the direction $\underline{s}^0$. When equation (49) is used for integration this dependence results from the direction of $\underline{\mathrm{d}x}'$, in case of equation (58) from the angle φ of the tangent. For $\boldsymbol{\sigma}^{\mathrm{semi}}$ of a straight segment with fixed line vector $\underline{s}^0$, Devincre (Devincre, 1995) derived:

$$\sigma_{ij}^{\mathrm{semi}} =$$

$$\frac{\mu}{2\pi Y^2} \left[(\underline{b} \times \underline{Y})_i \left(\underline{s}^0 \right)_j + (\underline{b} \times \underline{Y})_j \left(\underline{s}^0 \right)_i - \frac{\left(\underline{b} \times \underline{s}^0 \right)_i Y_j + \left(\underline{b} \times \underline{s}^0 \right)_j Y_i}{1 - \nu} \right]$$

$$- \frac{\mu}{2\pi Y^2} \frac{\underline{b} \times \underline{Y} \cdot \underline{s}^0}{1 - \nu} \left[\delta_{ij} + \left(\underline{s}^0 \right)_i \left(\underline{s}^0 \right)_j - \frac{2}{Y^2} \left(h_i Y_j + h_j Y_i + Y_i Y_j L / R \right) \right] \tag{60}$$

with the definitions $L = \underline{r} \cdot \underline{s}^0$, $\underline{h} = \underline{r} - L\underline{s}^0$, and $\underline{Y} = (r - L)\underline{s}^0 - \underline{h}$, and the point of stress observation being the origin. Some of these definitions are sketched in figure 25(a). The summation of stress contributions of semi-segments in equation (59) is equivalent to considering single segments with

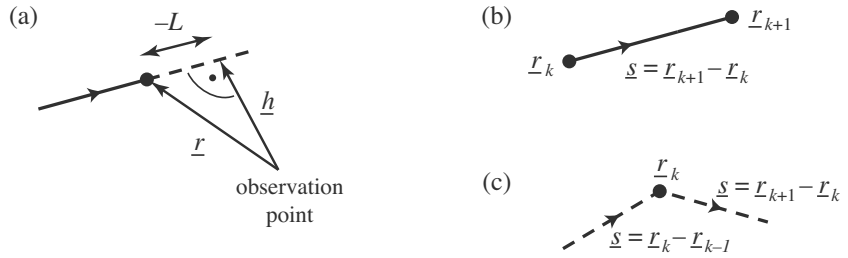

Figure 25. (a) Geometrical meanings for equation (60); (b) segment summation; (c) angular summation.

two different ending points $\underline{r}$ and the same line vector $\underline{s}^0$, as indicated in figure 25(b). This type of summation may be inconvenient, depending on the type of segmentation in a simulation code. An alternative approach is to evaluate equation (60) for the connection points $\underline{r}$ between segments with different line vectors $\underline{s}^0$, as indicated in figure 25(c).

For 2-dimensional simulations using only one glide plane $\underline{n}^0$, it is useful to apply a specialized and, therefore, simpler expression. With $\underline{n}^0 = (0, 0, 1)$ and the Peach-Koehler equation (16) applied to equation (49), the resolved stress of a segment from $\underline{r}_A$ to $\underline{r}_B$ is found as (Mohles, 2001c):

$$\tau_{\mathrm{seg}} = \frac{\mu}{4\pi}\frac{1}{D}\left[(\underline{b}_{\mathrm{s}} \cdot \underline{k})\,(\underline{b}_{\mathrm{r}}^0 \cdot \underline{s}) + \frac{(\underline{b}_{\mathrm{s}} \cdot \underline{k}_\perp)\,(\underline{b}_{\mathrm{r}}^0 \cdot \underline{s}_\perp)}{1-\nu}\right] \tag{61}$$

with $D = (\underline{r}_A \times \underline{r}_B)_z$, $\underline{s} = (s_x, s_y, 0) = \underline{r}_B - \underline{r}_A$, $\underline{k} = (k_x, k_y, 0) = \underline{r}_B^0 - \underline{r}_A^0$, $\underline{s}_\perp = (-s_y, s_x, 0)$, $\underline{k}_\perp = (-k_y, k_x, 0)$, and $\underline{b}_{\mathrm{s}}$ and $\underline{b}_{\mathrm{r}}$ denoting the Burgers vectors of the stress source and the stress receiving dislocation, respectively.

Self interaction Equations (49), (58), (60), and (61) describe the stresses a dislocation imposes on another one. In principle, the stress receiver can be the same as the source. But on the dislocation line, elasticity theory predicts a stress singularity as can already be seen from straight dislocations (equation (4) or (7)). This is an artifact of the dislocation being assumed to exist in a continuous medium, which is a conflict. In real materials this problem does not exist due to the atomistic nature of a real crystal. In applications of the quoted stress formulae, a bit of material around the point of stress observation must be cut out, in analogy to the calculation of the energy of straight dislocations.

One option for this is Brown's approach (Brown, 1964), (Brown, 1967)

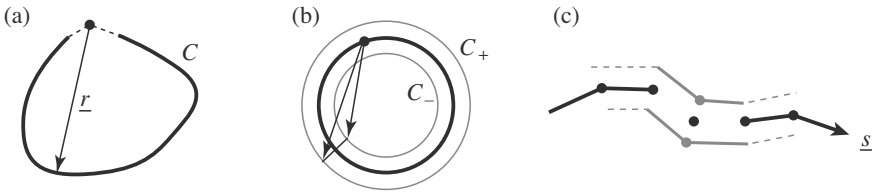

Figure 26. Cut-out procedures for the dislocation core introduced by (a) Bacon (Bacon, 1967); (b), (c) Brown (Brown, 1964), (Brown, 1967).

sketched in figure 26: instead of evaluating a stress formula on the dislocation line C itself (figure 26(a)), two lines C_+ and C_- parallel to C at given distances of $\pm r_{\mathrm{cut}}$ are considered (figure 26(c)), and the mean value of the corresponding stresses is used. By this procedure the dislocation core with radius r_{cut} is left out of the calculation. At large distances $|\underline{r}|$ this calculation yields the same stress contribution as using the original line C because the vectors to C_+ and C_- are very similar to $\underline{r}$ (figure 26(b)). But in the vincinity of the node (figure 26(c)), the vectors to C_+ and C_- have essentially opposite directions, and the respective stress contributions cancel each other. The additional computational effort of two, instead of one, stress calculations can be mostly avoided by using C_+ and C_- only in the vincinity of each node.

Another option to cut out the dislocation core is to disregard the stress contributions of the dislocation segments connected to the observation point, as sketched in figure 26(a). However, this procedure must be used with caution for two reasons: Firstly, the stress of a dislocation segment of finite length is not unique. As has been shown (Mohles, 2001c), the stress $\underline{b}^0 \boldsymbol{\sigma}_{\mathrm{disl}} \underline{n}^0$ with $\boldsymbol{\sigma}_{\mathrm{disl}}$ of equation (49) equals τ_{disl} of equation (58) if the same closed dislocation loop is considered. But if a dislocation segment is left out of the integration, the stresses do not match. After all, such a segment of finite length does not exist anyway (section 1.1). But in the calculations, errors of unknown magnitude can arise from this stress equivocality for non-closed dislocations. Such errors can be avoided by a special segmentation procedure described in section 3.1.

The second implication of disregarding the neighbour segments of a node is that the cut-out length L_{cut} has a meaning equivalent to that of r_{cut}: it defines the energy associated with the dislocation core (see equation (6aa), $r_{\mathrm{cut}} \approx r_{\mathrm{core}}$) and hence influences a dislocation's flexibility, as can be seen from the line tension model. In simulations, the lengths of the neighbour segments of every node will vary; but the core energy and the corresponding

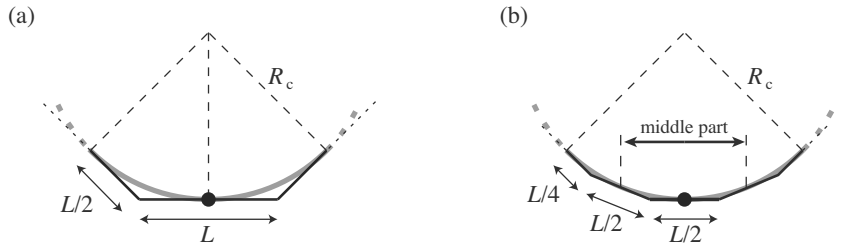

Figure 27. A curved dislocation segment (grey) of length $2L$ in different approximations (black) with (a) three and (b) five segments.

length L_{core} should be constant. In order to find a way to achieve this, we consider a curved dislocation segment (arc) of constant length $2L$ and curvature radius R_{c}. This arc is approximated by two different sets of straight segments, as sketched in figure 27. Subsequently, $L \ll R_{\mathrm{c}}$ is assumed; in figure 27 this condition is disregarded in order to improve the visibility of the angles. The dislocation arc is assumed to have a parabolic shape. With these assumptions and equation (61) the stress of the arc on its centre point can be calculated for the approximations with (a) three and (b) five segments. In both cases, the stress contribution of the segment in the centre vanishes for symmetry reasons. This centre segment may be seen as being cut out in the approximations. It gives no stress contribution, regardless of the stress formula used.

$$\tau_{(\mathrm{a})} = \frac{\mu b}{24 R_{\mathrm{c}}} \left(\frac{9 + 3\nu}{1 - \nu} \cos^2\alpha + \frac{9 - 12\nu}{1 - \nu} \sin^2\alpha \right) \tag{62}$$

$$\tau_{(\mathrm{b})} = \frac{\mu b}{24 R_{\mathrm{c}}} \left(\frac{13 + 7\nu}{1 - \nu} \cos^2\alpha + \frac{13 - 20\nu}{1 - \nu} \sin^2\alpha \right) \tag{63}$$

Here α is the angle between Burgers and line vector. Note that $\tau_{(\mathrm{a})}$ and $\tau_{(\mathrm{b})}$ depend on the curvature radius R_{c}, but they are independent of the length L. This means that when approximation (a) had been constructed with the same R_{c} but with an overall length of L instead of $2L$, the same stress $\tau_{(\mathrm{a})}$ would have been obtained. This is exactly the case for the middle part of the approximation in figure 27(b). Hence, the outer parts of (b) generate the stress $\tau_{(\mathrm{b})} - \tau_{(\mathrm{a})}$. This difference is the *additional* stress caused by the transition from approximation (a) to (b). In this transition, the length of the straight segment in the centre has been reduced by a *factor* two. Hence if the length L_{cut} is actually cut out of the calculations in a simulation, but L_{core} is the aspired cut-out length defined by the core energy, the *additional*

stress $\tau_{\rm arc}$ must be considered:

$$\tau_{arc} = \left(\tau_{(\rm b)} - \tau_{(\rm a)}\right)\ \log_2 \frac{L_{\rm cut}}{L_{\rm core}} = \left[\frac{2}{3\ln 2}\right] \frac{K_S(\alpha)}{bR_{\rm c}}\ \ln\ \frac{L_{\rm cut}}{L_{\rm core}} \qquad (64)$$

In the second part of equation (64), the pre-logarithmic stress factor $K_S(\alpha)$ of equation (35b) has been used to replace $\left(\tau_{(\rm b)} - \tau_{(\rm a)}\right)$. The similarity of equation (64) with the self-stress $\tau_{\rm self}$ in the line tension model (equation (34)) is not accidental: the line tension model is very local, just like the stress of a dislocation arc of finite length. But in applications of the line tension model, a more global, radial cutting procedure is used with the factor $\ln\left(r_{\rm shield}/r_{\rm core}\right)$ (equation (6b)) instead of the more local factor $\ln\left(L_{\rm cut}/L_{\rm core}\right)$.

The square bracket of equation (64) equals about 0.961. This resulted from the comparison of approximations (a) and (b). When a higher order approximation with halved segments and the cut-out length $L/4$ had been compared with approximation (b), the factor $[24/(35ln2)] \approx 0.989$ would have been found. Obviously the square bracket can be set to equal 1.0, like in the line tension model. Altogether the total self interaction of a dislocation in a point $\underline{r}_k$ including stress contributions from distant segments can be summarized by

$$\tau_{\rm self}\left(\underline{r}_k\right) = \sum_{i \neq k} \tau_{\rm seg}\left(\underline{r}_i - \underline{r}_k\right) + \frac{K_S\left[\alpha\left(\underline{r}_k\right)\right]}{bR_{\rm c}\left(\underline{r}_k\right)}\ \ln\ \frac{L_{\rm seg}\left(\underline{r}_k\right)}{L_{\rm core}} \qquad (65)$$

where $L_{\rm seg}\left(\underline{r}_k\right)$ is the local cut-out length and $L_{\rm core} \approx 2b$ is the length determining the core energy.

With equation (65) and a segment fomula like that of equation (60) or (61), the mathematics for dislocation dynamics simulations is complete. But the numerical effort for such simulations using the self interaction concept is very high because, in principle, the interaction of every dislocation segment with every other one must be calculated in every time step. This makes it inevitable to apply certain optimisations in a simulation code; some successful ones are described in section 4.2.

3 2-D Applications

Many plasticity related properties of materials depend on the flexibility of dislocations because the latter determines the actual number of obstacles a dislocation encounters simultaneously while moving. This can be seen from Friedel's basic strengthening model (section 2.1) for 2-dimensional dislocation glide, but it holds as well in three dimensions. The flexibility is mainly

determined by the dislocation's elastic self interaction (section 2.2) and approximately described by the line tension (section 2.1). In the present section, simulations of 2-D dislocation glide are described using both the line tension model as well as true self interaction.

3.1 Simulation Technique

The dislocation is described as a flexible line in the glide plane; the equilibrium of resolved stresses is considered along this line. Regardless of the dislocation model, the local equilibrium of resolved shear stresses τ along the dislocation line can be used as the basis for simulations:

$$\tau_{\text{ext}} + \tau_{\text{disl}} + \tau_{\text{allobst}} = 0 \tag{66}$$

Here τ_{ext} is an external stress driving the dislocation forwards; it can be derived from a global stress tensor via the Peach-Koehler formula (16). τ_{disl} denotes the dislocation's self interaction, either as given by τ_{self} of equation (65) or approximated by τ_{self} of equation (34). The obstacle stress τ_{allobst} can be defined by solute foreign atoms, particles of secondary phases, other dislocations, grain boundaries or any other kind of obstacles. The equilibrium (66) holds generally for static dislocation configurations like those considered in section 2.1; equation (66) has been used there implicitly.

If the equilibrium is violated the sum of resolved stresses renders a driving force on the line. For the simulations a non-static stress equilibrium is introduced by adding a viscous drag stress $\tau_{\text{drag}} = -(B/b)v_\perp$ to the left hand side of equation (66), where $v_\perp$ is the local velocity normal to the dislocation line and B is a drag coefficient. Inertial effects can be considered as well (see below) but are disregarded here so that the motion is assumed to be overdamped. The viscous drag term τ_{drag} may be seen to represent the phonon drag; Jassby and Vreeland (Jassby and Vreeland, 1973) have measured coefficients B of real specimens. However, the physical basis for τ_{drag} is irrelevant here because we are only looking for a static equilibrium here ($v_\perp \to 0$). When completed by τ_{drag}, equation (66) can be written as

$$v_\perp(\underline{x}) = (b/B)\,(\tau_{\text{ext}} + \tau_{\text{disl}} + \tau_{\text{allobst}}) \tag{67}$$

where $v_\perp$ defines the magnitude and the sign of the velocity, and it depends on the observation point $\underline{x}$ on the dislocation. The direction of the motion is defined by the unit vector $\underline{s}^0_\perp$ normal to the local line vector $\underline{s}$. Since only one glide plane is considered in 2-D, only planar vectors are noted subsequently. The directions $\underline{s}^0$ and $\underline{s}^0_\perp$ can be expressed by the derivatives $x' = \partial x/\partial s$ and $y' = \partial y/\partial s$: $\underline{s}^0 = (x', y')$ (see figure 28), where s denotes the arc length, and by definition $\underline{s}^0_\perp = (-y', x')$. The velocity vector $\mathrm{d}\underline{x}/\mathrm{d}t = (\mathrm{d}x/\mathrm{d}t, \mathrm{d}y/\mathrm{d}t)$ is

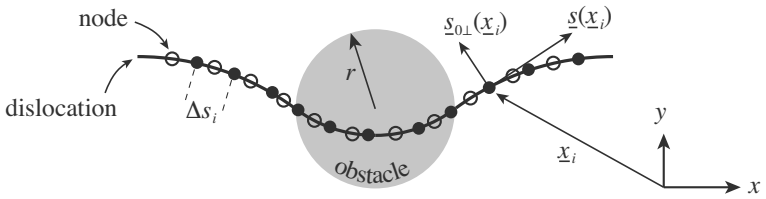

Figure 28. Local line vector $\underline{s}(x, y)$, and two possible representations of the same dislocation by different sets of nodes (empty and filled circles) of equal mean distance Δs (segmentation coarseness). Individual distances Δs vary. There are either 4 (empty) or 5 (filled) nodes inside the obstacle.

defined as $\mathrm{d}\underline{x}/\mathrm{d}t = \underline{s}^0_\perp v_\perp$ so that

$$\frac{\mathrm{d}}{\mathrm{d}t}\begin{pmatrix} x \\ y \end{pmatrix} = \begin{pmatrix} -\partial y/\partial s \\ \partial x/\partial s \end{pmatrix} \frac{b}{B}\left(\tau_{\mathrm{ext}} + \tau_{\mathrm{disl}} + \tau_{\mathrm{allobst}}\right) \tag{68}$$

τ_{disl} depends on the local curvature with the radius $R_{\mathrm{c}} = (y''x' - x''y')^{-1}$, where x'' and y'' denote the second derivatives $\partial^2 x/\partial s^2$ and $\partial^2 y/\partial s^2$, respectively. The dependence on R_{c} is obvious in the line tension model ($\tau_{\mathrm{disl}} = \tau_{\mathrm{line}}$, equation (35) but also holds for the self-interaction concept (equation (65)). In a simulation the derivatives x' and y', and R_{c} must be calculated for all points $\underline{x}_i$ and in each time step from the present configuration. This can be done for instance by constructing a circle through three neighbouring nodes $\underline{x}_{i-1}$, $\underline{x}_i$, and $\underline{x}_{i+1}$ and using the tangent in $\underline{x}_i$ for $\underline{s}_0$ and the radius for R_{c}. Altogether equation (68) is a partial differential equation which can be solved numerically, for instance using a Runge-Kutta type method (Press et al., 1992).

Dislocation discretisation For the simulations a discretisation is required. This means that a finite number of points $\underline{x}_i$ must be chosen to represent the dislocation line; equation (68) is then solved in these points. In figure 28, two different but equivalent discretisations of the same dislocation are plotted. Both representations have the same coarseness (average node distance), but either four or five nodes are located inside an obstacle. Individual distances Δs_i vary during a simulation run as the nodes move. But they have to be kept close to a mean value Δs by removing nodes or inserting new ones (by interpolation) during a simulation as required locally. This 'mean value' Δs may be forced to depend on the local curvature in order to keep the total number of nodes and hence the computational effort

low. However, the present author advises to use a constant value Δs within a simulation because a curvature dependent value Δs has sometimes been found to cause minor but systematic errors in simulation results.

For the subsequent considerations all individual distances Δs_i are assumed to equal Δs. In the example of figure 28, five of the filled nodes, but only four of the empty ones are inside the obstacle, where the dislocation is supposed to experience a constant obstacle stress $\tau_{\mathrm{obst}} = -\gamma/b$ (equation (19)) as in the case of a long-range ordered particle as an obstacle. This means that in y-direction (forward direction), the simulated dislocation in its critical configuration senses either the force $4\gamma\Delta s$ or $5\gamma\Delta s$, depending on which set of nodes happens to represent the dislocation. Hence, in principle, the simulated dislocation over- or underestimates the true maximum obstacle force $F_{\max} = 2r\gamma$ by the amount $\gamma\Delta s/2$, which causes a relative error of $\pm\Delta s/(4r)$. For the case of figure 28 this would mean an error of more than $\pm 10\%$ ($\pm 0.5\gamma\Delta s$ of $\approx 4.5\gamma\Delta s$). This statistical error can easily be reduced by choosing a higher node density Δs^{-1}. But this must be avoided because the calculation effort in the computer is roughly proportional to about Δs^{-3}: the number of nodes is proportional to Δs^{-1}. Likewise, in the self-interaction concept, the number of interaction partners for each node is proportional to Δs^{-1}. Moreover, the number of integration steps the integrator (any one) must take for a simulation run increases as Δs decreases. Therefore, in order to keep the calculation times in the computer low, the obstacle stress τ_{allobst} should be smoothed over the length Δs if it contains a discontinuity, like on the surface of the obstacle in figure 28. In that case $\Delta s = r/3$ can be chosen as the mean node distance for good simulation results, where r is the obstacle radius. However, this is only an upper limit. If two dislocations are simulated which get very close, like Shockley partial dislocations (section 1.4), Δs must not be larger than the distance between these dislocations (equation (23)). Otherwise, when Δs is too large, numerical instabilities can occur.

A lower limit for Δs is given by the length L_{core} (section 2.2), which is basically equivalent to the inner cut-off radius r_{core} in the line tension model. With a chosen length $r_{\mathrm{core}} = 2b$ it has been found that the simulations are only stable if $\Delta s > b/2$. For the upper limit $\Delta s = r/3$ quoted above this means that only obstacles with $r > 1.5b$ can be treated, for instance, particles with a diameter larger than 1 nm. Obviously this restriction arises from the linear elastic continuum model itself, which fails to cover atomistic properties well. While Δs affects the accuracy of the simulation results and the calculation speed, it does not affect the simulation results systematically as long as it is chosen constant.

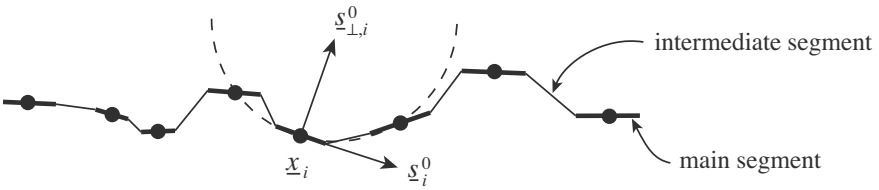

Figure 29. Segmentation procedure with main and intermediate segments used to ensure that the nodes are in the centres of straight (main) segments.

Dislocation segmentation When the dislocation self interaction model is used for τ_{disl}, a segmentation of the dislocation must be defined in addition to the discretisation in order to utilize a segment stress formula like equation (61). A frequently applied segmentation method is to use the node connecting vectors $\underline{x}_{i+1} - \underline{x}_i$ as segments. However, for the dislocation self interaction, a piece of dislocation around the point of stress observation must be cut out because of the stress singularity on the dislocation line. This may cause errors of unknown magnitude because the stress of a non-closed dislocation is undefined, as outlined in section 2.2.

However, the subsequent segmentation procedure fully avoids such errors becauses it enforces that every node is placed in the centre of a segment, where the stress of this segment vanishes unequivocally. This is accomplished in three steps. At first in every time step, a circle (dashed in figure 29) through the points $\underline{x}_{i-1}$, $\underline{x}_i$, and $\underline{x}_{i+1}$ is constructed for each node i. The local line direction $\underline{s}^0_i = \underline{s}^0(\underline{x}_i)$ and the local curvature radius $R_{\mathrm{c},i} = R_{\mathrm{c}}(\underline{x}_i)$ are derived from this circle. Then a straight dislocation segment with the direction $\underline{s}^0_i$ is assigned to node i so that this node lies in the centre of the segment. This is called a main segment. In figure 29 the main segments are drawn as thick lines. The length of main segments is chosen to be $\Delta s_i/2$, where $\Delta s_i = 1/2\,|\underline{x}_i - \underline{x}_{i-1}| + 1/2\,|x_{i+1} - \underline{x}_i|$ is the mean distance to the adjacent nodes. Finally, the end points of the main segments are connected by intermediate segments so that a closed polygon results. In figure 29 the intermediate segments are drawn as thin lines for distinction; they have no nodes in their centres. With this segmentation there are twice as many segments as nodes; to each node belong one main segment and two half intermediate segments on the left and the right. This segmentation may seem quite laborious, but possible errors arising from the stress ambiguity of segment stresses are avoided. Moreover, numerical instabilities have not been encountered with the present segmentation, even in cases which are prone to such instabilities (Duesbery et al., 1992). For the cut-out length

L_{cut} in the arc stress τ_{arc} of equation (64), the quoted value of $\Delta s_i/2$ is to be used.

Quasistatic simulation procedure A simulation run is started with any dislocation configuration, for instance a straight dislocation (or several ones) near the lower side of a rectangular obstacle field with the obstacle stress $\tau_{\mathrm{allobst}}(\underline{x})$. Usually this field contains many obstacles k at the locations $\underline{x}_k$; their stress contributions are superimposed locally:

$$\tau_{\mathrm{allobst}}(\underline{x}) = \sum_k \tau_{\mathrm{obst},k}\,(\underline{x} - \underline{x}_k, P_k) \tag{69}$$

In general the obstacles can have individual stress functions $\tau_{\mathrm{obst},k}(\underline{\Delta x})$ and parameters P_k. By solving the differential equation (68) for subsequent time steps, new configurations are found, hence dislocation glide is simulated. Various approaches can be used to derive quantitative results from this glide. One approach is to start with a low external stress τ_{ext}. This drives the dislocation forwards against the obstacles; usually there are many. The dislocation bows out between them until a static equilibrium configuration is found ($v_\perp = 0$ in all points). Then τ_{ext} is increased by a small step $\Delta\tau$ so that the dislocation bows out a bit more. Thereby the dislocation may overcome some obstacles by shearing or circumventing them before it finds the next equilibrium. Then τ_{ext} is increased again; this is repeated until the dislocation touches the upper side of the obstacle field. Then the simulation run is ended, and the last value of τ_{ext}, called $\mathrm{Max}[\tau_{\mathrm{ext}}]$, obviously suffices to keep the dislocation running continuously in this obstacle field. The simulated critical resolved shear stress τ_{sim} is defined as

$$\tau_{\mathrm{sim}} = \mathrm{Max}\,[\tau_{\mathrm{ext}}] - \Delta\tau \tag{70}$$

because this value is the highest one that yields a static dislocation configuration. $\Delta\tau$ should be chosen to be about 2% or 3% of an estimation of the end result τ_{sim}, which may, for instance, be the strengthening contribution τ_{p} of particles. In figure 30 several dislocation configurations are plotted while a single obstacle is overcome, either by shearing or by circumventing it.

The present definition of τ_{sim} may appear a bit arbitrary when an (irregular) array of obstacles is considered: if the array is particularly long so that the dislocation must overcome many obstacles successively, the probability will increase that the dislocation finds an obstacle arrangement which is particularly hard to overcome. This would increase τ_{sim}. On the other

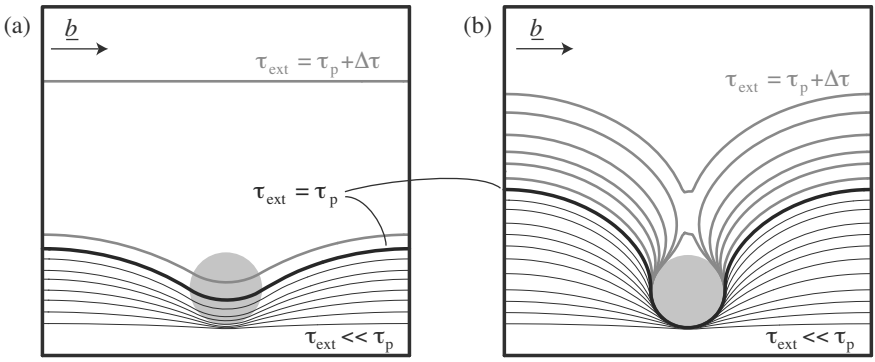

Figure 30. A dislocation overcoming an obstacle by (a) shearing or (b) circumventing it. Black lines are static equilibrium configurations, the grey lines are snapshots of the dislocation moving at a constant stress larger than the critical one, τ_p. In (b) an Orowan loop is left behind around the obstacle.

hand, if the obstacle array is particularly wide, so that a longer dislocation sweeps out in forward direction, this longer dislocation will have an increased chance to find an easy way to move on. This would lower τ_sim. These effects have been found to be rather weak and mostly compensate for each other. In test simulations no systematic dependence of τ_sim on the size of the obstacle field has been detected when the length and the width of the field were varied by equal factors. The typical scatter of τ_sim involved with individual obstacle fields of (mostly) equal statistical properties and size has been found to be $\pm 6\%$ for arrays with 500 to 1000 obstacles (Bacon, 1967), (Foreman and Makin, 1966), (Foreman and Makin, 1967).

The outlined approach to derive τ_sim is quasistatic: The dislocation's velocity tends to vanish in the static equilibrium positions, the last of which defines τ_sim. This means that the derived result is independent of the strain rate. Moreover this means that the drag coefficient B has no meaning and is arbitrary in these simulations: According to equation (68), B defines the time scale in the simulations, but the time required in reality to accomplish the stress increments $\Delta\tau$ is disregarded.

Dynamic simulation procedures In experiments the measured stress to overcome obstacles is often found to depend on the strain rate $\dot{\varepsilon}$. Such a dependence of $\tau_\mathrm{sim}(\dot{\varepsilon})$ can be introduced in simulations by assuming a mobile dislocation density ρ_m and enforcing a predefined dislocation velocity:

$v = \dot{\gamma}/(b\rho_\mathrm{m})$ (Orowan equation (13)). This can be done by continuously adjusting the external stress τ_ext accordingly (Monnet, 2006); in that case τ_sim is defined as the temporal average of τ_ext. By this method the tendency $\partial\tau_\mathrm{sim}/\partial\dot{\varepsilon} > 0$ is found, in agreement with experiments. But this strain rate dependence is only linked to the viscous drag factor B, which accounts for the phonon drag. The much stronger strain rate dependence resulting from thermally activated dislocation motion is not considered in this approach.

In a truly dynamic simulation the thermal stress pulses τ_therm on a dislocation are accounted for. They introduce probabilities for dislocations to overcome obstacles by the help of these pulses at a given temperature. In addition, effects of a dislocation's inertia can be accounted for by a stress term τ_inert. Hence the stress equilibrium of equation (66) is extended to

$$\tau_\mathrm{inert} + \tau_\mathrm{drag} + \tau_\mathrm{ext} + \tau_\mathrm{therm} + \tau_\mathrm{disl} + \tau_\mathrm{allobst} = 0 \tag{71}$$

where again $\tau_\mathrm{drag} = -(B/b)v_\perp$ and equivalently, the inertial stress is defined as $\tau_\mathrm{inert} = -(m^*/b)a_\perp$ with a length specific mass m^* and the acceleration $a_\perp$ normal to the dislocation line vector $\underline{s}^0$. It must be emphasized here that the introduction of m^* is as vague as the introduction of a line tension because the dislocation's inertia is not in the line but in the motion and mass of all atoms surrounding it. Still, a mass of about one atom weight is usually attributed to the length of one Burgers vector (Isaac and Granato, 1988), (Mohles, 1997). With $a_\perp$ being the second derivative in time, the equivalent of equation (68) can be written as

$$\frac{\mathrm{d}^2}{\mathrm{d}t^2}\underline{x} = \underline{s}^0_\perp \frac{b}{m^*}\left(-(B/b)v_\perp + \tau_\mathrm{ext} + \tau_\mathrm{allobst} + \tau_\mathrm{disl} + \tau_\mathrm{therm}\right) \tag{72}$$

The thermal stress pulses, τ_therm, are essentially random numbers without correlation in time and space, which impose Brownian motion on the dislocation. The pulses add or substract energy to the dislocation in random amounts; on a temporal average energy is added by the term τ_therm. But as the random motion of the dislocation increases, so does the dissipation via τ_drag. Hence an equilibrium will be found in which the energy added to the dislocation by τ_therm is compensated on a temporal average by τ_drag, such that an average amount of random motion resides in the dislocation: this is the temperature. This fluctuation-dissipation-theorem for dislocations defines the amplitude of the random pulses τ_therm:

$$\tau_\mathrm{therm}\left(\underline{r}_i, \Delta t_j\right) = \frac{1}{b}\sqrt{\frac{2Bk_\mathrm{B}T}{\Delta s_i\ \Delta t_j}}\ \Lambda_{i,j} \tag{73}$$

$$\text{with} \quad f(\Lambda) = \frac{1}{\sqrt{2\pi}}\exp\left(-\frac{\Lambda^2}{2}\right)$$

Here k_B is the Boltzmann constant, T is the temperature, Δs_i is the length attributed to the dislocation segment located at $\underline{r}_i$, and Δt_j is the time interval during which the particular stress $\tau_\mathrm{therm}\left(\underline{r}_i, \Delta t_j\right)$ acts. $\Lambda_{i,j}$ are random numbers picked individually from the indicated Gaussian distribution $f(\Lambda)$ for $\underline{r}_i$ and Δt_j. The dependence of τ_therm on the drag coefficient B reflects the energy equilibrium quoted above. Equation (74) ensures for instance that each dislocation node in a fixed glide plane, which represents one degree of freedom, has the average kinetic energy $\left\langle 1/2\left(m^* \Delta s_i\right) v^2 \right\rangle = 1/2 k_\mathrm{B} T$.

A simulation using the stochastic equation (72) never finds an equilibrium configuration due to the thermal stresses. Instead, the dislocation will move through the obstacle field in a jerky manner, as is also observed by in-situ transmission electron microscopy. Instead of a critical stress the mean glide velocity can be evaluated as a function of temperature and τ_ext; this is discussed in section 3.4.

3.2 Static Simulations Using the Line Tension Model

The present section summarizes some simulations using the simple line tension model to calculate the strengthening effect of simple obstacles which give some general insights. This means that equation (68) is used, with τ_line of equation (34) used for τ_disl, and τ_ext is imcremented by steps $\Delta\tau$ as described in section 3.1. Hence only τ_allobst is to be defined via equation (69). For the simulations of the present section, the following simplifying assumptions are used in order to allow for a direct comparison with analytical models (section 2.1) and the more refined simulations from literature:

(i) The obstacles are circular. Inside the obstacles $\tau_\mathrm{obst} = -\gamma/b = \text{const.}$, and outside $\tau_\mathrm{obst} = 0$. This corresponds to energy storing obstacles: When the obstacle area q is swept by a dislocation, the energy $q\gamma$ is employed (by τ_ext) and stored in form of a faulted boundary. This case is similar to order strengthened materials (section 3.3, $\gamma = \pm\gamma_{APB}$). (ii) The radius r of all obstacles in the glide plane is the same. Accordingly the maximum obstacle force $F_\mathrm{max} = 2r\gamma$ and energy $q\gamma = \pi r^2 \gamma$ are well-defined. (iii) The obstacle arrangement in the glide plane is purely random in section 3.2; later on, this condition is relaxed to some extent. (iv) The line tension model is used with the line energy E^* and hence the line tension S being constant, hence $S = E^*$ according to equation (34). (v) Only one dislocation is simulated. All simulated data are presented in the common scales described subsequently. These scales have been chosen because they are convenient for weak and strong obstacles of any extension and arrangement.

An important length scale in a real crystal is the obstacle radius r. Another length scale is the shortest distance L_cc between the obstacles (centre

to centre) which would hold if they were arranged in a square grid. L_{cc}^{-2} is the number of obstacles per unit area. Each obstacle occupies the area $q = \pi r^2$, hence

$$L_{cc} = r\sqrt{\pi/f} \tag{74}$$

where f is the area fraction covered by the obstacles. The obstacle strength $F_{max} = 2r\gamma$ is related to the line tension S; the relative strength is denoted by k.

$$k = \frac{F_{max}}{2S} = r\frac{\gamma}{S} = r\frac{b\tau_{obst}}{S} \tag{75}$$

Note that the fraction S/γ is another length scale in addition to r and L_{cc}. One of these three scales may be taken as the unit length and be kept constant in simulations. For analytical considerations, L_{cc} may be useful as a unit length; however, in the present simulations it is more convenient to keep (S/γ) constant. This latter parameter depends on material parameters alone, and not on the geometry of the obstacles and their arrangement. This geometry is subject to variations in the subsequent simulations.

All stresses are described in units of τ_{unit}, which is defined as:

$$\tau_{unit} = F_{max}/\left(bL_{cc}\right) = \sqrt{(4/\pi)f}\,(\gamma/b) \tag{76}$$

By definition, τ_{unit} is independent of S. This is helpful since S is not known exactly, neither in evaluations of experiments nor in simulations using the self-interaction concept (section 3.3). But τ_{unit} does already include the basic stress dependence on f : $\tau_{unit} \sim f^{1/2}$. For instance, in these units the critical stress predicted by Friedel's model (section 2.1) simply reads as $\tau_{Friedel} = k^{1/2}\tau_{unit}$ with *apparently* no dependence on f.

The magnitude b of the Burgers vector in equation (76) is, in principle, a fourth length scale. But it appears only in τ_{unit} and, therefore, does not interfere with the other length scales.

The normalized simulation results τ_{crit}/τ_{unit} are basically a function of the parameters k and f alone. This gets obvious when all terms in the stress equilibrium (equation (68) with $\tau_{disl} = \tau_{line}$) are divided by τ_{unit}. The ratio τ_{obst}/τ_{unit} depends only on f (τ_{obst} of assumption (i)). The ratio τ_{line}/τ_{unit} can be written as a function of k, f, and the local curvature R_c (in units of the chosen unit length S/γ). The latter stands for the dislocation configuration (on the scale of S/γ). This configuration *adjusts itself* to the parameters (τ_{ext}/τ_{unit}), k, and f in the given obstacle arrangement. The last stable equilibrium configuration for given values of k and f, which defines $\tau_{crit} = Max\,[\tau_{ext}]$, depends on the individual spatial arrangement of the obstacle field used. Hence τ_{crit}/τ_{unit} is a function of k and f and the geometry of the individual obstacle arrangement. The latter merely

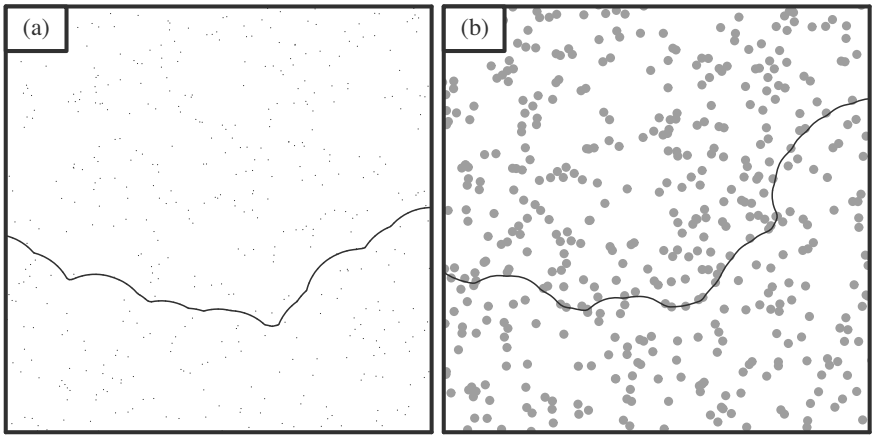

Figure 31. Critical dislocation configurations simulated with the line tension model for randomly distributed overlapping obstacles. Only parts of the obstacle arrays are shown. The number of obstacles ($\approx$ 440 of 8000 total) and the relative obstacle strength $k = 0.304$ are the same. The area fractions of the obstacles and the critical resolved shear stress are (a) $f = 0.0025$ ($\approx$ point obstacles), $\tau_{\rm crit}/\tau_{\rm unit} = 0.60$; (b) $f = 0.16$ (extended obstacles), $\tau_{\rm crit}/\tau_{\rm unit} = 0.91$.

produces a statistical scatter in $\tau_{\rm crit}$. It has been found that this scatter is about $\pm 6\%$ for obstacle arrays containing 500 to 1000 obstacles (see section 3.1). For the present simulations with 8000 obstacles in the square-shaped obstacle field, the scatter is estimated less than $\pm 4\%$.

Effects of the obstacle strength and size When obstacles are vanishingly small ($r \ll L_{\rm cc}$, or $f \to 0$) they can be considered as point obstacles. The effect of the relative obstacle strength k on dislocation configurations and on $\tau_{\rm crit}$ in arrays of point obstacles have been worked out in literature by analytical models like Friedel's and also by computer simulations (Foreman and Makin, 1966), (Foreman and Makin, 1967). However, the condition $r \ll L_{\rm cc}$ (or $f \ll 1$) is not sufficient to rate the applicability of the results (Mott and Nabarro, 1948), (Schwarz and Labusch, 1978) because another independent length scale beside r and $L_{\rm cc}$ is involved, namely the material dependent constant S/γ.

If obstacles have a finite extension, a distinction must be made whether the obstacles are allowed to overlap each other spatially or not. Of course,

objects like second phase particles cannot overlap in reality, but their obstacle stresses can. Subsequently the respective obstacles are called overlapping and discrete, respectively. The term 'non-overlapping' as the opposite of 'overlapping' is avoided because it is prone to cause confusion. An example for overlapping obstacles are particles with a lattice mismatch (see e.g. section 3.3): their coherence stresses superimpose (overlap) linearly. In contrast, in dispersion strengthening and order strengthening (section 3.3) the stresses do not overlap spatially; these particles are discrete obstacles.

Figure 31 shows two examples of simulated critical dislocation configurations for a very low ($f = 0.0025$) and a rather high ($f = 0.16$) area fraction. The relative obstacle strength $k = 0.304$ is the same in both cases. With $f = 0.0025$ the dislocation configuration is very similar to those found by Foreman and Makin and successors by means of the circle rolling technique (Foreman and Makin, 1966), (Foreman and Makin, 1967), (Hanson and Morris, 1975). Even with $f = 0.16$ the configuration looks rather similar. This may surprise because with less free space between the obstacles at $f = 0.16$, weaker bow-outs are to be expected. But in the obstacle array this is 'compensated' for by a higher external stress: $\tau_{\mathrm{crit}}/\tau_{\mathrm{unit}}$ is found to be higher for $f = 0.16$ than for $f = 0.0025$ by about 50% although the obstacle strength k and density (their number) are the same. Hence this must be an effect of f, or the relative obstacle extension r/L_{cc}.

In figure 32, τ_{crit} is plotted (empty symbols) as a function of the square root of the normalised obstacle strength k, equation (75), for four area fractions f. For comparison results from literature are added. As to be expected, $\tau_{\mathrm{crit}}/\tau_{\mathrm{unit}}$ for $f = 0.0025$ agrees well with results from literature for point obstacles in the full range of k: with $L_{\mathrm{cc}} \gg r$ the obstacles are point-like. At low k, the simulations agree with Friedel's result τ_{Friedel} of equation (71) very well. Near $k \approx 1$ the strength reaches a maximum, albeit τ_{crit} is reduced by a factor 0.8 relative to τ_{Friedel}; this is attributed to the randomness of the obstacle array (Foreman and Makin, 1966), (Foreman and Makin, 1967). In the range $k > 1$, $\tau_{\mathrm{crit}}/\tau_{\mathrm{unit}}$ decreases because the Orowan process operates here.

At higher volume fractions $f = 0.01$, which might still be considered as small, systematic deviations with increasing f are found: $\tau_{\mathrm{crit}}/\tau_{\mathrm{unit}}$ increases with increasing f, for weak and for strong obstacles. This means that for reasonably strong particle strengthening effects, which usually require $f > 0.01$, point obstacles are rather inaccurate as a model. In the following, generally, the data with $f = 0.16$ are discussed because they show the strongest effects. But the statements and conclusions also hold for lower area (or volume) fractions.

For weak obstacles an increase of τ_{crit} with increasing obstacle extension

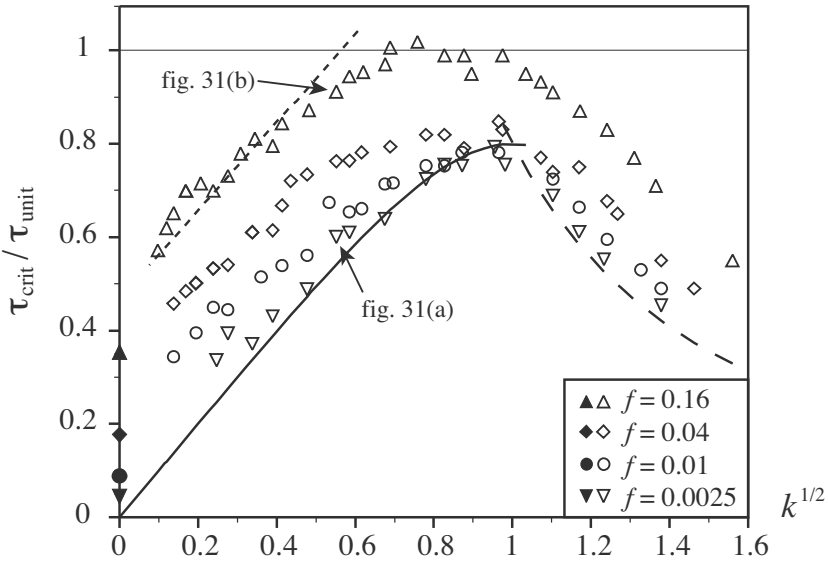

Figure 32. Normalized critical stress as a function of k and f. Empty symbols represent simulations, filled symbols indicate the energy storing effect: $\tau_{\text{store}} = f\gamma/b$; —— $\tau_{\text{FM}} = (1 - 0.2k^2)k^{1/2}\tau_{\text{unit}}$; — — $\tau_{\text{OFM}}(f = 0) = 0.8k^{-1}\tau_{\text{unit}}$; - - - - $\tau_{\text{LS}}(f = 0.16) = (0.94k^{1/2} + 1.17f^{1/2})\tau_{\text{unit}}$.

has already been found by Labusch and Schwarz (Labusch and Schwarz, 1992). The computer simulations of these authors were originally designed for solid solution hardening, but the results can also be applied to particle strengthening. Labusch and Schwarz used obstacles extended only in the direction normal to the dislocation line. Similar to point obstacles, such obstacles cannot overlap because they are one-dimensional (1-D); their areas vanish. This may lead to the perception that these obstacles are non-overlapping and hence discrete, but physically these 1-D obstacles overlap since a non-vanishing obstacle area (area fraction $f > 0$) is assigned to the 1-D obstacles in order to apply a simulation result, hence they inevitably have a finite width $w_x > 0$. The obstacle arrangement of Labusch and Schwarz was purely random (a pre-requisite for the scaling used by these authors); therefore, the obstacles can actually overlap, and they increasingly do so with increasing w_x or f.

In the units used here, the simulation results τ_{SL} of Labusch and Schwarz for energy storing obstacles reads: $\tau_{\text{LS}} = \left(0.94k^{1/2} + 1.17f^{1/2}\right)\tau_{\text{unit}}$. As in-

dicated for $f = 0.16$ in figure 32, this result also represents the present simulations well. Essentially it appears that in the range $0 < k < 1$, $\tau_{\mathrm{crit}}/\tau_{\mathrm{unit}}$ is increased relative to $\tau_{\mathrm{Friedel}}/\tau_{\mathrm{unit}} = k^{1/2}$ by the amount $f^{1/2}$. This effect is caused by the energy storing character of the obstacles: when a dislocation is straight as in the case $k = 0$, the fraction f of it resides inside obstacles and senses the obstacle stress $\tau_{\mathrm{obst}} = -\gamma/b$. This leads to the critical stress $\tau_{\mathrm{crit}} = f\gamma/b = (\pi f/4)^{1/2}\tau_{\mathrm{unit}}$ for straight dislocations. If the obstacles involved negative and positive obstacle stresses τ_{obst} in equal amounts, this contribution to τ_{crit} would vanish. This latter case means that the dislocation stores no energy when it overcomes obstacles, unlike in the present case. More accurate statistical investigations have shown (Arsenault et al., 1989a), (Arsenault et al., 1989b) that stress fluctuations also give rise to a stress $\tau_{\mathrm{crit}}(k = 0)$; however, this is beyond the scope of the present contribution.

In the case of very strong obstacles with $k > 1$, which are circumvented by the Orowan process, τ_{crit} decreases with increasing k because the free space between the obstacles, $L_{\mathrm{cc}} - 2r$, scales with k (equation (75)). In the present units, Orowan's stress prediction (26) reads $\tau_{\mathrm{crit}} = \left(1 - (4f/\pi)^{1/2}\right)^{-1} k^{-1}\tau_{\mathrm{unit}}$. This also predicts an increase of the relative stress $\tau_{\mathrm{crit}}/\tau_{\mathrm{unit}}$ with increasing volume fraction f, in full agreement with figure 32.

Around $k = 1$, τ_{crit} has a maximum. At $f = 0.16$ it can be seen that $\tau_{\mathrm{crit}}/\tau_{\mathrm{unit}} \leq 1$ defines a maximum for τ_{crit}. It is reached when (i) the obstacles exert the maximum force (i.e. $2S$) and (ii) the distance between obstacles is small. The smallest distance that can be reached everywhere in the glideplane for a given number density is L_{cc}, the centre-to-centre square lattice spacing. This had been used for the definition of τ_{unit} (equation (76), so that $\tau_{\mathrm{crit}} \leq \tau_{\mathrm{unit}}$ holds for any other obstacle arrangement, regardless of f.

Effects of the obstacle arrangement The geometry of the obstacle arrangement can affect the resulting critical stress, as can be seen in figure 33 by comparing the overlapping obstacles of figures 31 and 32 with discrete obstacles as defined above. The arrangement of discrete obstacles is generated in the computer by assigning random locations to all obstacles first, disregarding overlappings like above. Then all obstacles which are found to overlap with others are assigned new random locations. The latter step is repeated until no more overlaps are found. The prevention of overlaps means a restriction for the randomness of the obstacle arrangement: at very large area fractions f, the arrangement of rigid obstacles will be close to a closest packing, which is a very regular arrangement. The restriction of

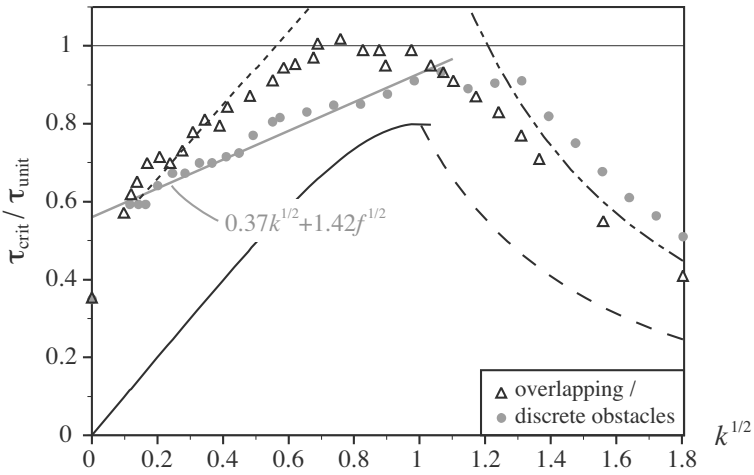

Figure 33. Normalized critical stress as a function of k at $f = 0.16$ for overlapping (black) and discrete (grey) obstacles; lines as in figure 32 except for — - — $\tau_{\mathrm{OFM}}(f = 0.16) = 0.8k^{-1}\left(1 - (4f/\pi)^{1/2}\right)^{-1}\tau_{\mathrm{unit}}$.

randomness is obviously most pronounced at high area fractions; therefore only the case $f = 0.16$ is considered subsequently.

In the range of strong obstacles ($k > 1$), the discrete obstacles yield a higher critical stress than the overlapping ones (figure 33). This has two reasons. Firstly, in the case of overlapping obstacles the fraction f of f, i.e. f^2, does not contribute to strengthening because it overlaps. This reduces the effective volume fraction to $f - f^2$ and lowers τ_{crit} correspondingly. Secondly, in case of a regular obstacle arrangement as is the tendency for the discrete obstacles, the probability for the dislocation to find weak spots (large individual obstacle distances) is low; this also increases τ_{crit} .

For weak obstacles ($k < 1$), the overlapping obstacles yield a higher stress than the discrete ones. This is most obvious for $k^{1/2} \approx 0.7$. A possible explanation is that the overlapping areas can be seen as separate obstacles with double strength ($\tau_{\mathrm{obst}} = -2\gamma/b$). The area fraction of these obstacles of double strength equals $f^2 = 0.0256$. The total area fraction covered by obstacles is reduced from f to $f - f^2$ due to overlapping. This would lower τ_{crit} like in the case $k > 1$. But this is overcompensated by the obstacles with double strength because they have a stronger influence than the normal ones: $\tau_{\mathrm{crit}} \sim k^{1/2}\tau_{\mathrm{unit}}$ according to Friedel's model, where both τ_{unit} and k increase linearly with γ.

The simulated data of discrete obstacles for $f = 0.16$ and $k < 1$ are well represented by a linear function of $k^{1/2}$ (grey line in figure 33), similar to τ_{LS} (see figure 32), but with different coefficients: $\tau_{\mathrm{crit}}/\tau_{\mathrm{unit}} = 0.37k^{1/2} + 1.42f^{1/2}$ instead of $\tau_{\mathrm{LS}}/\tau_{\mathrm{unit}} = 0.94k^{1/2} + 1.17f^{1/2}$. While $\tau_{\mathrm{LS}}/\tau_{\mathrm{unit}}$ is essentially in line with τ_{Friedel} and τ_{FM} (parallel lines in figure 32), which had also been derived for random obstacle arrangements, the results for the more regular arrangement of the discrete obstacles deviates strongly. This emphasizes the importance of using realistic obstacle arrangements in simulations.

3.3 Simulations Using Dislocation Self Interaction: Particle Strengthening

The present section summarizes some simulations using the accurate dislocation self interaction model and the quasi-static procedure to calculate the strengthening effect of spherical second phase particles in a material. This means that equation (68) is used, with τ_{self} of equation (65) for τ_{disl}. τ_{allobst} is defined by equation (69) with a realistic distribution of particles as obstacles (locations $\underline{x}_k$, radii r_k). The interaction functions $\tau_{\mathrm{obst}}(\underline{\Delta x})$ depend on the particle types.

Realistic particle arrays As has been shown in section 3.2, the arrangement of obstacles has a significant impact on the critical stress τ_{crit}; the same holds for other geometrical properties. For instance, the impact of the size distribution of particles on their strengthening effect has been worked out statistically by Nembach (Nembach, 1996). Realistic particle arrangements may be obtained from atom-probe tomographic reconstructions or phase field or Monte-Carlo-simulations of precipitation. But in most cases, the obtainable particle arrangements are too small, meaning that they contain too few particles to keep the statistical scatter involved with individual arrangements low.

For the subsequent simulations, an arrangement is used which has been generated artificially and compared to real particle arrangements (Mohles and Fruhstorfer, 2002). The particles are assumed to be spherical and to have the radius distribution $g_{\mathrm{LSW}}(\rho)$ which has been derived analytically by Lifshitz, Slyozov (Lifshitz and Slyozov, 1961) and Wagner (Wagner, 1961) for the case of Ostwald ripened particles of low volume fractions f. In the

range $\rho = r/r_0 < 1.5$,

$$g_{\mathrm{LSW}} = \frac{4}{9}\rho^2 \left(\frac{3}{3+\rho}\right)^{7/3} \left(\frac{1.5}{1.5-\rho}\right)^{11/3} \exp\left(\frac{\rho}{\rho - 1.5}\right) \tag{77}$$

and $g_{\mathrm{LSW}}\,(\rho \geq 1.5) = 0$, where r are individual radii and r_0 is the mean particle radius. With this size distribution a rather closely packed arrangement of spheres is generated. Each of these spheres is meant to represent the corona of volume from which one particle has obtained its material during the Ostwald ripening process. By scaling appropriately all distances and individual corona radii down to the particle radii, the mean particle radius r_0 and the volume fraction f is selected. Finally, these particles are shifted by small additional random vectors to adjust the arrangement's randomness to experimental findings. The procedure is detailed and the resulting arrangements are discussed in (Mohles and Fruhstorfer, 2002).

Dispersion strengthening In dispersion strengthened crystals the glide system in the matrix is not continued inside the particles. Hence the particles are impenetrable; they must be circumvented by the Orowan process. In simulations this is enforced with a negative obstacle stress of large amount ($\tau_{\mathrm{obst}} \to -\infty$) inside the obstacles and no stress outside. For reasons of numerical stability it may be useful or even necessary (depending on the numerical integration method) to assume a finite but sufficiently high stress instead, and to smooth out the stress transition in $\tau_{\mathrm{obst}}(\underline{\Delta x})$ on the particle's interface in order to the limit slope of the step function. Details on the chosen stress value inside the particles and on the smoothing procedure are given in (Mohles, 2001c).

To give an impression, two dislocation configurations of a simulation using this obstacle stress are plotted in figure 34. $\tau_{\mathrm{obst}}(\underline{x})$ is represented by the dark grey disks: these are the intersections of the particles (arranged in 3-D) with the glide plane. The size distribution of these disks result from the particle size distribution $g_{\mathrm{LSW}}\,(r/r_0)$ and from the distribution of heights at which the particles intersect the plane. The starting configuration was a straight screw dislocation (dashed; $\underline{b}$ is indicated in figure 34); however, the dislocation bends strongly while gliding such that all dislocation characters are present. The local bending between the particles is stronger in x- than in y-direction because edge dislocations are more flexible than screw dislocations. This is predicted by the line tension model (section 2.1) and obviously remains true in the present case, where each dislocation piece interacts with every other one, including the Orowan loops. Quantitative results of dispersion strengthening are presented and discussed in (Mohles

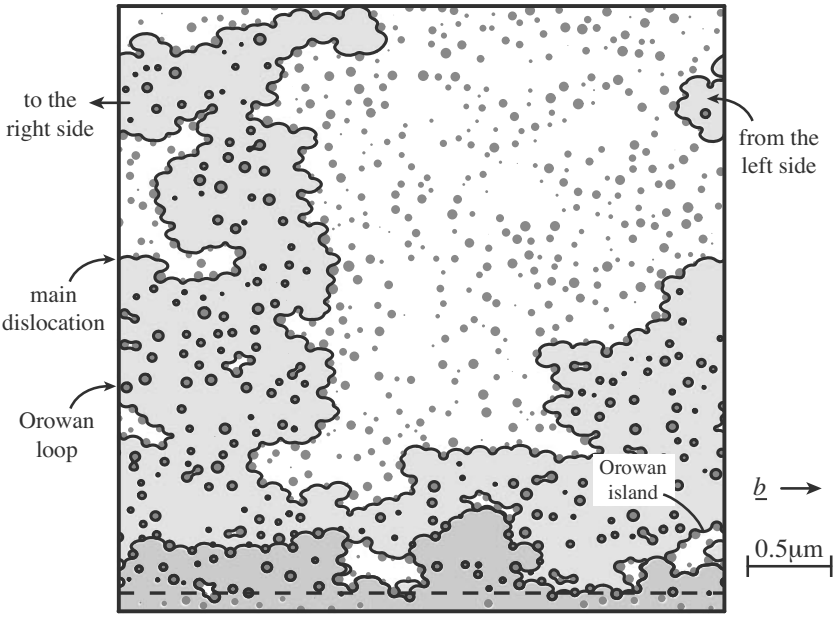

Figure 34. Two dislocation configurations in a dispersion strengthened crystal with $r_0 = 100b$, $f = 0.1$, Poisson ratio $\nu = 0.4$. The dashed line indicates the starting position; on the left and right periodic boundary conditions are applied. Dark grey: particle intersections with the glide plane; medium / light grey: area swept out at $\tau_{\text{ext}} = 226\text{MPa}$ / 230MPa. Representative configurations for other parameters can be seen in (Mohles and Fruhstorfer, 2002). Note that every piece of dislocation interacts elastically with all other pieces.

and Nembach, 2001).

Order strengthening In order strengthened materials, the crystal structure is continued inside particles (they are coherent), and they usually have long-range order whereas the matrix is disordered. This causes the dislocations to glide in pairs of two: the first one of a pair is pushed backward inside the particles because it destroys the order there, which takes energy, and creates an antiphase boundary with the energy γ_{APB}. A second dislocation in the same glide plane may restore this order and is, therefore, pushed forward. Hence according to equation (19) the obstacle stress for

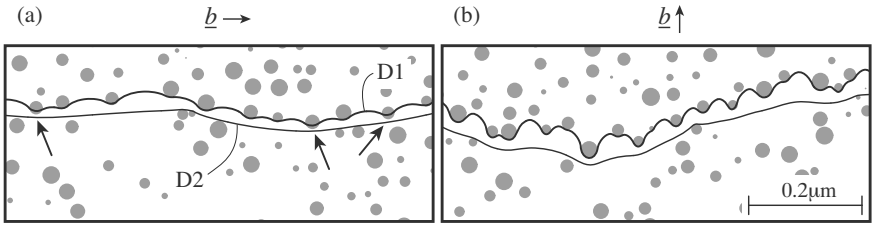

Figure 35. Critical dislocation configurations in a peak-aged order strengthened crystal for a pair of (a) screw and (b) edge dislocations. In the screw configuration the leading dislocation D1 often penetrates the particles (arrows) so that D2 is likely to follow immediately; edge dislocations do not show this effect.

these dislocations is described by

$$\tau_{\text{obst}}\,(\underline{\underline{\Delta x}}) = \begin{cases} -\gamma_{\text{APB}}/b \text{ for 1st dislocation inside particle} \\ +\gamma_{\text{APB}}/b \text{ for 2nd dislocation inside particle} \end{cases} \tag{78}$$

and $\tau_{\text{obst}} = 0$ outside the particles. Like in dispersion strengthening a smooth step function should be used for $\tau_{\text{obst}}(\underline{x})$ on the particle interfaces.

Figures 35(a) and (b) show sections of a pair of simulated screw and edge dislocation pairs. All parameters are chosen close to those of the Nickel based superalloy Nimonic PE16: $b = 0.25$nm, $\mu = 65$GPa, $\nu = 0.4$, $\gamma_{\text{APB}} = 0.25\text{Jm}^{-2}$. The volume fraction is $f = 0.1$, and the mean particle radius is $r_0 = 49b$. These latter parameters define the aging state of the material: a thermal treatment (prior to our plastic deformation) will define the amount (f) and the size (r_0) of the particles that precipitate from the matrix due to classical nucleation, growth and ripening.

If only one dislocation is considered, equation (78) is similar to the obstacle stress $-\gamma/b$ assumed for the obstacles in section 3.1. Accordingly the critical stress of order strengthed materials can be discussed in terms of the relative obstacle strength k introduced in equation (75): for a given material, which defines defines (S/γ_{APB}), the parameter k is essentially equivalent to the mean particle radius r_0. The line tension S is not defined in the present simulations because the dislocation self interaction model is used, but S is known to be rather constant as it depends on the surrounding dislocation geometry only through a logarithm function (equation 24). Similar to the simulation results of section 3.2, the strengthening of particles reaches a maximum at some mean radius r_0 (where $k \approx 1$). The corresponding material is denoted as peak-aged. With smaller or larger radii, the material is

in the underaged or overaged aging state, respectively.

The dislocation configurations in figure 35 belong to the peak-aged state. The leading edge dislocation D1 in figure 35(b) bows out strongly between the particles, almost as strong as in the case of dispersion strengthening in figure 34: D1 almost circumvents the particles. Actually, in case of large radii r_0, the configuration of D1 looks just like in figure 34; D2 is stuck behind Orowan loops left behind by D1. On the other hand, the leading screw dislocation D1 in figure 35(a) shears the particles, as is indicated by arrows. The trailing dislocation D2 is always rather straight because it touches almost no particles; and if it does so, it is pushed forwards as modelled. In the underaged state (small radii) both dislocations are rather straight, and D1 and D2 move as a pair. Altogether the dependence $\tau_{\mathrm{crit}}\left(f, r_0\right)$ for order strengthening is rather complex because of the combined shearing and circumventing of the particles, as well as by D1 and D2 moving either as a pair or individually. This is explained in more detail in (Mohles, 2004).

Lattice mismatch strengthening In the previous subsections of section 3.3 the particles were discrete obstacles because only in their interior, the dislocations interacted with them. This is different when the particles have a lattice mismatch: inside the particles there is hydrostatic stress, and outside there are shear stresses that cause a long-ranged interaction with dislocations. Hence these particles are overlapping obstacles, and moreover, their arrangement in 3-D space is important because the obstacle stresses depend on the height Δz of the particle centre over the glide plane. In the former cases, only the particle intersections with the glide plane mattered. The stress tensor of a spherical inclusion in an isotropic medium had been derived by Eshelby (Eshelby, 1956); applying the Peach-Koehler formula (16) on this yields the obstacle stress:

$$\tau_{\mathrm{obst}}\left(\underline{\Delta x}, \underline{b}^0\right) = \begin{cases} 6\varepsilon\mu\Delta z r^3 |\underline{\Delta x}|^{-4} \left(\underline{b}^0 \cdot \underline{\Delta x}^0\right) & \text{outside the particle} \\ 0 & \text{inside} : |\underline{\Delta x}| < r \end{cases} \tag{79}$$

Here ε denotes the constrained (relaxed) relative lattice mismatch. Inside the particle τ_{obst} vanishes because a driving force for dislocation glide results only from shear stresses. Outside, the stress depends on the direction of the Burgers vector $\underline{b}$ (but not on the line vector $\underline{s}$). This means that a static simulation procedure with τ_{obst} and τ_{allobst} changes as $\underline{b}$ is rotated, but for a given dislocation, $\underline{b}$ is constant and hence the obstacle stress is unique for it. Still, edge and screw dislocations experience different overall stresses because for a given $\underline{b}$, screw and edge dislocations experience τ_{obst} in different locations (as $\underline{s}$ must differ).

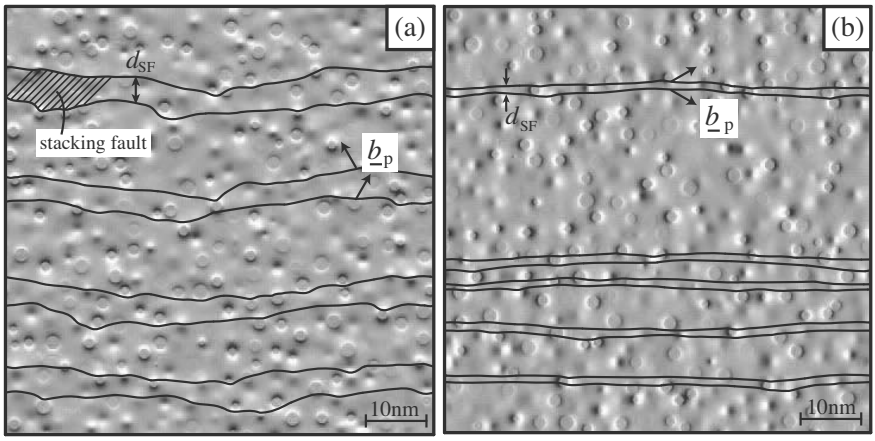

Figure 36. Configurations of one pair of Shockley partial dislocations in an underaged lattice mismatch strengthened crystal with $f = 0.1$. The greyscale plot of τ_{allobst} (dark: > 0, light: < 0) is that of the corresponding perfect dislocation. (a) Dissociated edge, (b) screw dislocation.

The partials of a dissociated dislocation sense different obstacle stresses when their Burgers vectors $\underline{b}_{\text{p1}}$ and $\underline{b}_{\text{p2}}$ differ, like in the case of Shockley partials (section 1.4). In figure 36 several dislocation configurations of such a case are plotted for a copper matrix with cobalt particles ($\mu = 42\text{GPa}$, $\nu = 0.43$, $\underline{b}_{\text{p}} = 0.148\text{nm}$, $\gamma_{\text{SF}} = 0.036\text{Jm}^{-2}$, $\varepsilon = 0.015$). The edge dislocation in figure 36(a) is dissociated more strongly than the screw dislocation in 36(b). With the elastic dislocation repulsion and the attraction stress $\pm\gamma_{\text{SF}}$ from the stacking fault considered in the simulation, the distance d_{SF} between the partials adjusts automatically in a simulation, and the mean value of d_{SF} agrees with d_{eq} of equation (23). The background of figures 36(a) and (b) is a greyscale plot of the obstacle stress $\tau_{\text{allobst}}\left(\underline{\Delta x}, \underline{b}^0\right)$, which is the combination of equation (79) with (69) for a given arrangement of particles k located at $\underline{x}_k$. Since τ_{allobst} depends on $\underline{b}_0$, the vector of the corresponding perfect dislocation has been used for the greyscale plot.

The dissociation width d_{SF} is another length scale in addition to those described in section 3.2. This makes analytic predictions of τ_{crit} very difficult, in particular when d_{SF} is in the range of the particle radius or the free space between them, like in the case of figure 36. Another difficulty for analytic considerations is that τ_{allobst} represents a wide spectrum of obstacle strengths; the effective number and strength of obstacles cannot be defined

unequivocally as can be seen from the greyscale plots. This makes it hard to apply analytic strengthening models as those in section 2.1 (Nembach, 1996). However, in dislocation simulations all effects can be considered concurrently. More details on such simulations can be found in (Mohles and Nembach, 2001), (Mohles, 2001a), (Mohles, 2001b), (Mohles, 2002), (Mohles, 2003).

3.4 Simulations of Thermally Activated Dislocation Glide

In section 3.1, the procedure for dynamic simulations considering random thermal stress pulses has been described. The stochastic nature of the differential equation (72) prevents the dislocations from ever finding a local equilibrium; they always stay in motion. This makes simulations particularly slow when the self interaction concept is used because some of its optimizations (section 4.2) remain useless. Therefore the line tension approach is used for the present simulations: $\tau_{\mathrm{disl}} = \tau_{\mathrm{line}}$ of equation (34).

Thermal activation helps dislocations to overcome obstacles. This means that the stress required to overcome the obstacles is lowered by a dimensionless factor $\tau_{\mathrm{rel}} < 1$ which depends on the temperature T, the imposed shear rate $\dot{\gamma}$ and possibly on other parameters:

$$\tau_{\mathrm{ext}} = \tau_{\mathrm{rel}}\,(T,\ \dot{\gamma},\ ...)\,\tau_{\mathrm{0K}} \tag{80}$$

where τ_{0K} is the stress required to overcome the obstacles by mechanical stress alone, that is at $T = 0\mathrm{K}$. In the terms used so far for the static simulations, τ_{0K} is the same as τ_{crit} with all its dependences on r_0, on f or on other parameters. When the obstacles are large, the thermal pulses are not strong enough to push a dislocation over obstacles. In that case the stress $\tau_{\mathrm{ext}} = \tau_{\mathrm{0K}}$ is required, or $\tau_{\mathrm{rel}} \to 1$ virtually independent of T. In contrast, small obstacles like solved foreign atoms are overcome by thermal activation. This causes solid solution strengthening to be temperature dependent.

Jerky dislocation glide In order to simulate solid solution strengthening, the obstacle stress $\tau_{\mathrm{obst}}(\underline{\underline{\Delta x}})$ of single foreign atoms must be defined. Here only an approximating function can be used as long as the foreign atom's interaction with the atomistic nature of the dislocation core is not known accurately. A possible approach is to consider a foreign atom as a sphere and calculate its size mismatch by equation (79) with the radius $r = b/2$. The locations $\underline{x}_k$ can be chosen to represent lattice or interstitial sites of the crystal lattice considered. In the greyscale plots of τ_{obst} in figure 37 used later on, the foreign atoms are assumed to be substitutive in a face centred cubic crystal. The stress of equation (79) is altered slightly

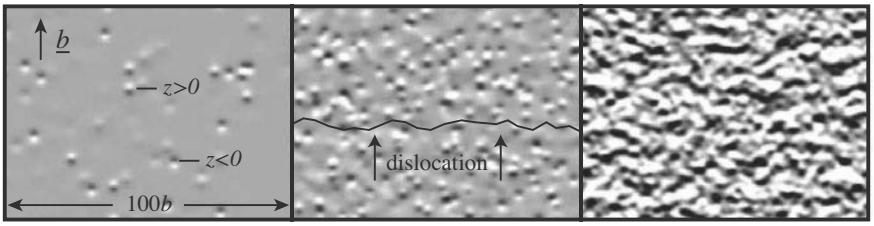

Figure 37. Greyscale plot of the assumed atomic mismatch obstacle stress at $c_{\mathrm{at}} = 10^{-3}/10^{-2}/10^{-1}$.

by ignoring the 'hole' (vanishing stress) inside the atoms. Furthermore, the stress is convoluted with a Gauss function $\exp\left(-|\underline{\Delta x}|^2/b^2/2\right)$ in order to account for the non-discrete nature of a real dislocation core; details are not important here. Figure 38 shows dynamic configurations of thermally activated dislocation glide in such obstacle fields in equidistant time steps. In some areas the dislocation moves fast (low line density) and in other places its overall velocity vanishes; here the dislocation only fluctuates (black areas), waiting for activation. Accordingly, the mean velocity v_{mean} of this jerky motion through the whole field can be written as

$$v_{\mathrm{mean}} = \frac{\lambda}{t_{\mathrm{wait}} + t_{\mathrm{run}}} \approx \frac{\lambda}{t_{\mathrm{wait}}} \tag{81}$$

where λ is the mean free path between waiting positions, and t_{run} and t_{wait} are the mean time intervals of running and waiting, respectively. Usually t_{run} is fully negligible compared to t_{wait}. The free path λ may be considered as a constant defined by the obstacle density, for instance by $\lambda^2 \approx b^2/c_{\mathrm{at}}$. This is not always the case, especially when inertial effects become important and the dislocation overruns obstacles with its kinetic energy (Mohles, 1997). Even in figure 38, an estimated λ would be larger for $c_{\mathrm{at}} = 10\%$ than for $c_{\mathrm{at}} = 1\%$, which is in contradiction to the aforementioned definition of λ. Still, the mean velocity is mostly determined by t_{wait} and its dependence on the temperature T and the present stress τ_{ext}, both of which assist activation (transition from waiting to running).

In figures 38(b) and (c), the same parameters have been used except for the sets of random numbers for τ_{therm}. The resulting mean velocities v_{mean} for this obstacle field differ by a factor two in these simulation runs. Hence in order to derive a function $v_{\mathrm{mean}}(T, \tau_{\mathrm{ext}})$ from simulations, many single simulation results must be averaged. This of course means a high numerical effort, which is another argument against using the dislocation self interaction concept for thermally activated dislocation glide. On the other hand,

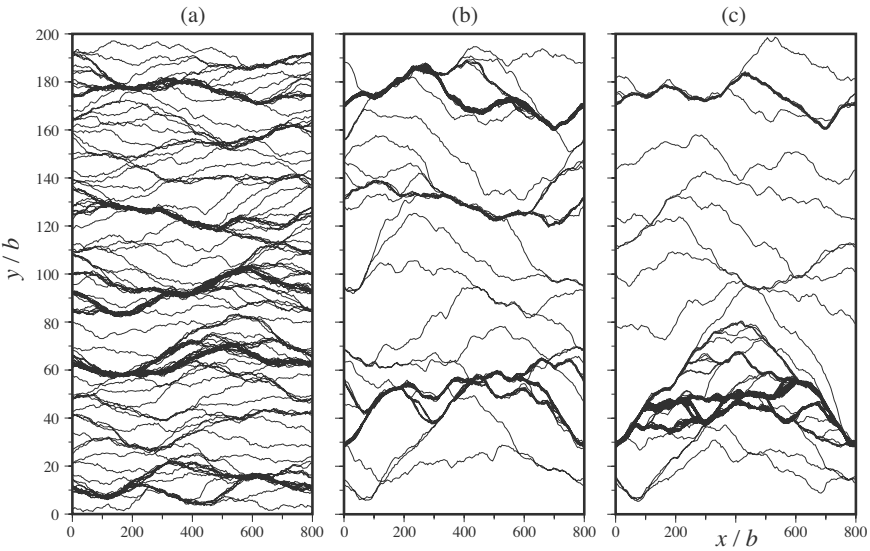

Figure 38. Dislocation configurations of thermally activated dislocation glide after equidistant time intervals. (a) $c_{\mathrm{at}} = 1\%$, $\tau_{\mathrm{ext}} = 7\mathrm{MPa} \rightarrow v_{\mathrm{mean}} = 10\mathrm{m/s}$; (b) $c_{\mathrm{at}} = 10\%$, $\tau_{\mathrm{ext}} = 27\mathrm{MPa} \rightarrow v_{\mathrm{mean}} = 6.1\mathrm{m/s}$; (c) $c_{\mathrm{at}} = 10\%$, $\tau_{\mathrm{ext}} = 27\mathrm{MPa} \rightarrow v_{\mathrm{mean}} = 3.3\mathrm{m/s}$. In (b) and (c) all parameters are equal except for the sets of random numbers for τ_{therm}, causing different configurations and mean velocities v_{mean}. Note that the y-direction has been streched by a factor 8 for clarity.

v_{mean} has essentially been broken down to the mean activation event with its mean waiting time t_{wait}. Individual waiting times vary much stronger than by a factor of two, but the activation event can be treated analytically and also by simulation.

Simulated activation event In figure 39, three simulated activation events are plotted. The obstacles are small size mismatched spherical particles which are not intersected by the glide plane; details are not important here. In figure 39(a), the obstacles are arranged at random. They are all equal in strength, size and shape, but there are attractive and repulsive obstacles. Starting from the static equilibrium position found at $T = 0\mathrm{K}$ (dashed line), the dislocation fluctuates for a while at $T = 300\mathrm{K}$ (grey lines around the dashed one) and eventually reaches a critical configuration (thick black line). When such a configuration has been reached, the dislocation

moves on (grey lines beyond the critical configuration): it has overcome the obstacle arrangement. The fact that the activation takes place on the boundary is physically meaningless because the boundary is periodic. The critical configuration has been estimated from observation of many simulated activation events; a different one has been published in (Mohles and Rönnpagel, 1996) for the same obstacle and dislocation parameters. Always in a critical configuration, the dislocation has moved forwards from its static equilibrium by Δy equal to about one obstacle diameter. The length of dislocation which has moved forward is much larger than Δy, by roughly two orders of magnitude. Note that in figure 39, the y-direction has been stretched by a factor ten. The estimated number of obstacles that are overcome concurrently in the critical configuration is two or three.

The activation event for the equidistant obstacle row in figure 39(b) can be described in exactly the same way. Even the same estimated activation length L_{est} is found from the critical configuration. It has often been assumed in literature (e.g. (Kocks et al., 1975), (Nadgornyi, 1988)) that this length is related to the distance L_{cc} between obstacles, but figure 39(c) proves that this assumption is fundamentally wrong. There, a continuous obstacle wall with the stress $\tau_{\mathrm{wall}}(y)$ replaces the obstacles such that

$$\tau_{\mathrm{wall}}(y) = \frac{1}{L_{\mathrm{cc}}} \int_{-\infty}^{\infty} \tau_{\mathrm{row}}(x, y)\mathrm{d}x \tag{82}$$

where $\tau_{\mathrm{row}}(x, y)$ is the stress function of the obstacles in figure 39(b). The obstacle wall stands for an obstacle row with a high density ($L_{\mathrm{cc}} \to 0$) of weak obstacles ($\mathrm{d}F_{\max} = b\tau_{\mathrm{obst}}\mathrm{d}x \to 0$). Since no length L_{cc} is involved in the activation event of figure 39(c), the activation length L_{act} (of which L_{est} is an estimation) cannot be related to the obstacle density. Instead, L_{act} depends on the dislocation's flexibility (or, the line tension S) and the present stresses τ_{wall} and τ_{ext}. This is similar to section 3.2, where the term $(b\tau_{\mathrm{obst}}/S)$ defined an important length scale. In the subsequent section the activation event and the related length L_{act} are considered analytically.

Analytic description of the activation event In the simulations of section 4.2, a critical dislocation configuration has been estimated from simulations. The criticality of this configuration lies in the dislocation's decision to either move back and continue waiting or to move forward and leave the waiting position: this is an unstable state close to an unstable equilibrium (saddlepoint configuration). The static stress equilibrium of a dislocation is given by equation (71) with $\tau_{\mathrm{therm}} = \tau_{\mathrm{drag}} = \tau_{\mathrm{inert}} = 0$. For the present case, $\tau_{\mathrm{allobst}}(x, y)$ is replaced by $\tau_{\mathrm{wall}}(y)$, and $\tau_{\mathrm{line}}(R_{\mathrm{c}}$ of equation (34)) is used for τ_{disl}. The dislocation's shape can be described as a function

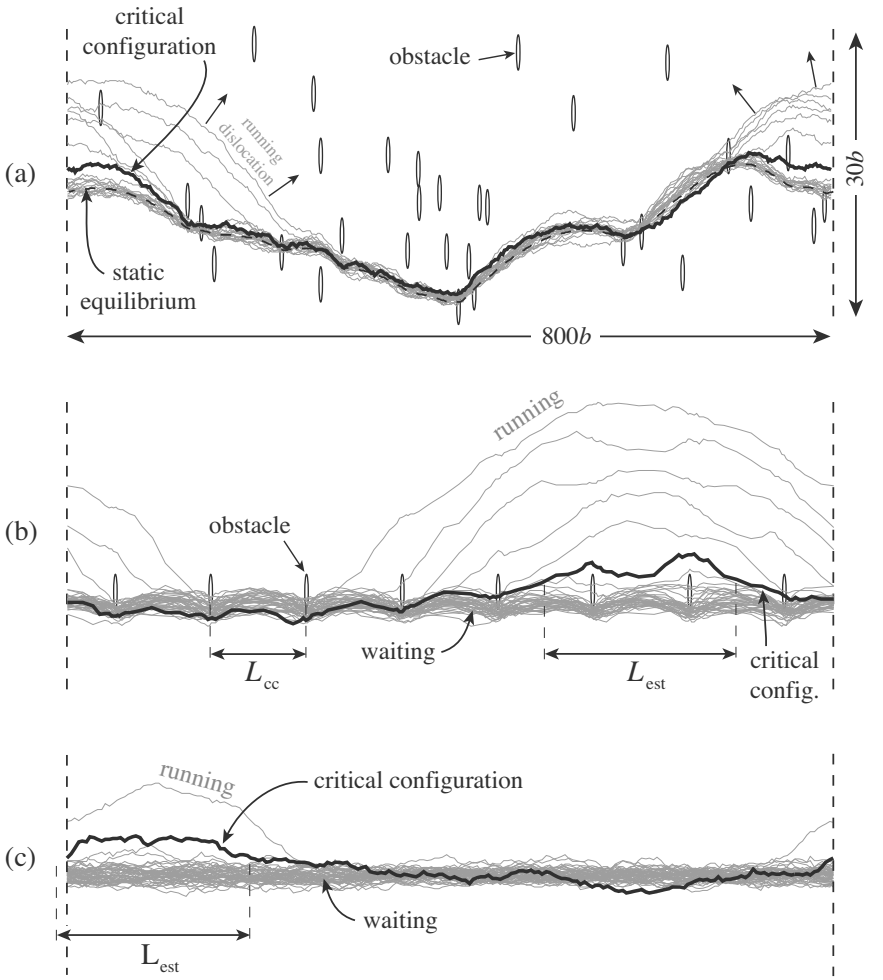

Figure 39. Dislocation configurations of activation events at different obstacle arrangements: (a) random arrangement, (b) equidistant obstacle array, (c) continuous obstacle wall. In all cases $\tau_{0K} = 25.3$MPa, $\tau_{ext} = 23$MPa, $T = 300$K. The obstacle wall stands for an infinite density of infinitely weak obstacles ($L_{cc} \to 0$, $F_{max} \to 0$). Note that the y-direction is stretched by a factor 10 for improved visibility.

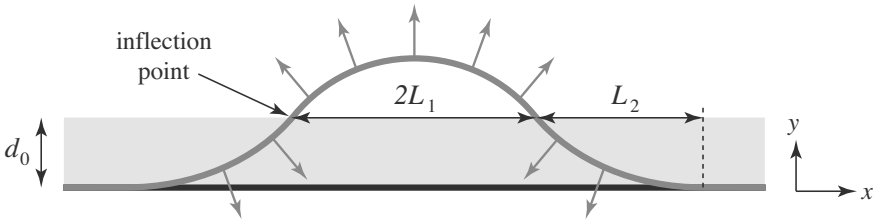

Figure 40. Unstable (grey) and stable (black) equilibrium configuration (T=0) of a dislocation at an obstacle wall (light grey).

$y(x)$. Approximating the curvature $(1/R_c)$ by the derivative $\mathrm{d}^2y/\mathrm{d}x^2$ yields the differential equation

$$\frac{\mathrm{d}^2y}{\mathrm{d}x^2} = -\frac{b}{S}\left(\tau_{\mathrm{wall}}(y) + \tau_{\mathrm{ext}}\right) \tag{83}$$

for $y(x)$. The quoted approximation is justified because the critical configurations are known to be flat (figure 39). The function $\tau_{\mathrm{wall}}(y)$ is described by the wall's maximum height, $\tau_{0\mathrm{K}}$, and by a function describing its 'shape' in y-direction. The latter contains a depth parameter d_0 which is related to the obstacle diameter. For simplicity a rectangular wall shape is assumed here; in (Mohles, 1997) a parabolic shape has also been examined with essentially the same results.

$$\tau_{\mathrm{wall}}(y) = \begin{cases} -\tau_{0\mathrm{K}} & \text{if } 0 < y \le d_0 \\ 0 & \text{otherwise} \end{cases} \tag{84}$$

With the simplified wall of equation (84), the solution $y(x)$ of differential equation (83) can be found easily by assembling dislocation pieces of constant curvature, as sketched in figure 40. A trivial solution is $y = 0$, where $|\tau_{\mathrm{wall}}| = \tau_{\mathrm{ext}}$ by definition. This describes the stable configuration. In the unstable configuration of figure 40, the curvature over the length $2L_1$ is $K_1 = b\tau_{\mathrm{ext}}/S$ (i.e., $K_1 < 0$), and in the two pieces of L_2, the curvature is $K_2 = b\left(\tau_{0\mathrm{K}} - \tau_{\mathrm{ext}}\right)/S$ (i.e., $K_2 > 0$). The length L_2 is defined geometrically by K_2 and d_0; with the quoted parabolic approximation $L_2 = \left(2d_0/K_2\right)^{1/2}$. In the inflection points the slopes have the magnitude $|m| = K_2L_2 = K_1L_1$, which finally defines L_1. Altogether this yields

$$L_1 = \sqrt{\frac{2d_0S\left(\tau_{0\mathrm{K}} - \tau_{\mathrm{ext}}\right)}{b\ \tau_{\mathrm{ext}}^2}} \quad \text{and} \quad L_2 = \sqrt{\frac{2d_0S}{b\ \left(\tau_{0\mathrm{K}} - \tau_{\mathrm{ext}}\right)}} \tag{85}$$

With the geometry $y(x)$ of the unstable configuration known, the energy ΔG can be calculated. ΔG is required to bring the dislocation from the stable to the unstable configuration. ΔG is comprised of two contributions. One is given by the obstacle stress between the configurations, reduced by the energy that is expended by the external stress. This part is found by integrating $(b\tau_{\mathrm{wall}} - b\tau_{\mathrm{ext}})$ in the area between the unstable and the stable configuration; it is large if L_1 and L_2 are large. The other contribution is given by the increment of dislocation length $\left[\int \left(\mathrm{d}x^2 + \mathrm{d}y^2\right)^{1/2}\right]$ from the stable to the unstable configuration; this part is large when L_1 and L_2 are small. In the equilibrium configuration $y(x)$, however, these contributions have equal magnitudes, as can be verified. Together this yields

$$\Delta G = \frac{4\sqrt{2}}{3}\sqrt{b\ d_0^3\ S\ \tau_{0\mathrm{K}}}\frac{1}{\tau_{\mathrm{rel}}}\left(1-\tau_{\mathrm{rel}}\right)^{1/2} \tag{86}$$

where τ_{ext} has been expressed by the relative stress τ_{rel} introduced in equation (80). ΔG is the energy that must be expended by the thermal pulses for activation. The energy contribution expended for this by the external stress has already been accounted for in the first contribution outlined above. The first square root in equation (86) is a universal feature of the activation energy, independent of the shape of the obstacle wall. It emphasizes that the activation event is governed by both the integrated obstacle stress $\tau_{0\mathrm{K}}$, which equals the maximum of τ_{wall} from equation (82), and the line tension S. The dependence of ΔG on τ_{rel} and the pre-factor is defined by the wall shape. Other wall shapes have been discussed in (Mohles, 1997). Instead of a stress wall, a potential trough can also be considered. When the trough is V-shaped with a slope equivalent to τ_{0K}, equation (86) is recovered (Kocks, 1985).

With equation (86) and the general Boltzmann equation, the probability of one attempted activation event (one attack) to be successful is known. The attack frequency, ν_0, is known to be in the range 10^{10} to 10^{11}Hz (Mohles, 1997), (Granato et al., 1964). Hence the waiting time for activation is

$$t_{\mathrm{wait}} = \frac{1}{\nu_0}\ \exp\frac{\Delta G}{k_{\mathrm{B}}T} \tag{87}$$

with ΔG and its dependence on $\tau_{0\mathrm{K}}$, S, and d_0 defined by equation (86). The dependence on τ_{rel} remains to be refined. In particular, close to the top of the wall, i.e. for $\tau_{\mathrm{rel}} \to 1$, the rectangular shape is not a good approximation; however, for small obstacles like foreign atoms this is not so critical.

Solid solution strengthening In deformation experiments often a constant shear rate $\dot{\gamma}$ is enforced. With a density of mobile dislocations ρ_m defined by the specimen's deformation state this enforces a mean dislocation velocity, as described by Orowan's equation (13). When the mean free running path λ of dislocations is assumed to be constant, this means that t_wait and hence ΔG is given (equations (81), (87), ν_0=const., T=const.). Since τ_0K, S and d_0 are material parameters, this defines τ_rel (equation (86)) and τ_ext (equation (80)), which here is called the solute strengthening contribution τ_sol here. Resolving for $\tau_\mathrm{ext} = \tau_\mathrm{sol}$ yields

$$\tau_\mathrm{sol} = \tau_{0K} \frac{2}{1+\sqrt{1+T^2/T_0^2}} \quad \text{with} \quad T_0 = \frac{\sqrt{8bd_0^3 S\tau_\mathrm{0K}}}{3k_\mathrm{B}\ln\left(\lambda\nu_0 b\rho_\mathrm{m}/\dot{\gamma}\right)} \tag{88}$$

where T_0 has no particular meaning as a special temperature; it is just an abbreviation for the temperature scale. Altogether τ_sol depends on the solute concentration c_at, but this dependence only comes through $\tau_\mathrm{0K}\,(c_\mathrm{at})$. Calculation of the latter dependence is an independent problem.

When reasonable values for solute atoms are inserted in equation (88) (e.g. $d_0 = b$, b=0.25nm, $S = \mu b^2/2$, μ=50GPa, τ_0K=50MPa, $\ln(\lambda\nu_0 b\rho_\mathrm{m}/\dot{\gamma}) = 20$), τ_rel comes out to be about 1/3 at room temperature: these small obstacles are indeed overcome by thermal activation. On the other hand, small particles with a diameter of only $d_0 = 8b = 2$nm yield $\tau_\mathrm{rel} = 0.97$. This means that thermal pulses do not help (much) to overcome particles. As noted above, the assumption of a rectangular wall shape is not a good one for $\tau_\mathrm{rel} \to 1$, so this result is not accurate. However, it can be shown with a parabolic shape of $\tau_\mathrm{wall}(y)$ (Mohles, 1997), which is more appropriate for $\tau_\mathrm{rel} \to 1$, that the statement remains valid that the strengthening contribution even of rather small particles ($d_0 \geq 4$nm) is independent of temperature (no thermal activation).

Equation (88) shows that τ_sol depends on the strain rate only weakly, but that it decreases with increasing temperature considerably. However, even at high temperatures the strengthening effect of solutes does not vanish entirely. This is all in agreement with experimental findings (e.g. (Kocks, 1985)).

4 3-D aspects

When dislocations glide in their glide planes they will encounter other ones in other glide planes. These dislocations interact mutually as described by elasticity theory, but they are also subjected to a number of reactions and effects that are intrinsically 3-dimensional. They lead to specific patterns of dislocation arrangements. For instance in face centred cubic crystals during

tensile or compression tests, the dislocations form cells with high dislocation density in the cell walls and low density in the interiors. In contrast, fatigue tests with thousands of loading and unloading cycles tend to lead to alternating layers of high and low dislocation density. One aim of 3-dimensional dislocation dynamics simulations is to investigate the corresponding pattern formation and the associated work hardening effects. However, such investigations are still in their infancy due to the enormous computational effort of dislocation dynamics simulations. Here some fundamental aspects of 3-D dislocation motion are compiled, in particular those with implications on the implementation of dislocation dynamics simulations.

4.1 Non-elastic 3-D effects

The elastic interaction between dislocations has already been described in section 1.3 for straight dislocations and in section 2.2 for arbitrary configurations. The present section outlines additional effects which in particular include irreversible dislocation reactions.

Intersecting dislocations When dislocations on different glide planes cross each other they impose a shape change on each other. Several cases are to be distinguished depending on the directions of the line and Burgers vectors. In figure 41, four cases are plotted in which two initially straight dislocations cross each other at right angles. In each of these cases and in general, every dislocation acquires a piece of dislocation length (added local line vector) of the magnitude and direction of the other dislocation's Burgers vector. This is simply a consequence of the Burgers vector being a shift vector. In the cases (a) and (d), one of the two dislocations only gains or loses length of the other dislocation's Burgers vector, whereas in the other cases both dislocations acquire a jog or kink.

In figure 41(b), each edge dislocation gets a short piece of screw dislocation lying in the same glide plane. Such local character changes in the same glide plane are called kinks; they can accompany the dislocations' glide without resistance (planar Peierls stresses are disregarded here). The edge dislocation in figure 41(d) has also acquired a kink, and the screw dislocation in 41(c) also has a kink: the line vector of this kink lies in the screw dislocation's glide plane, which in the present case is defined by the line vector and the direction of motion (see section 1.1).

The upper dislocation in figure 41(a) and the edge dislocation in 41(c) have acquired a jog, i.e. a segment with a line vector $\underline{s}$ normal to its glide plane (see 41(a)). With their own line vectors but unchanged Burgers vectors, these jogs define their own glide planes $\underline{n}_{\mathrm{jog}}$. The glide directions of

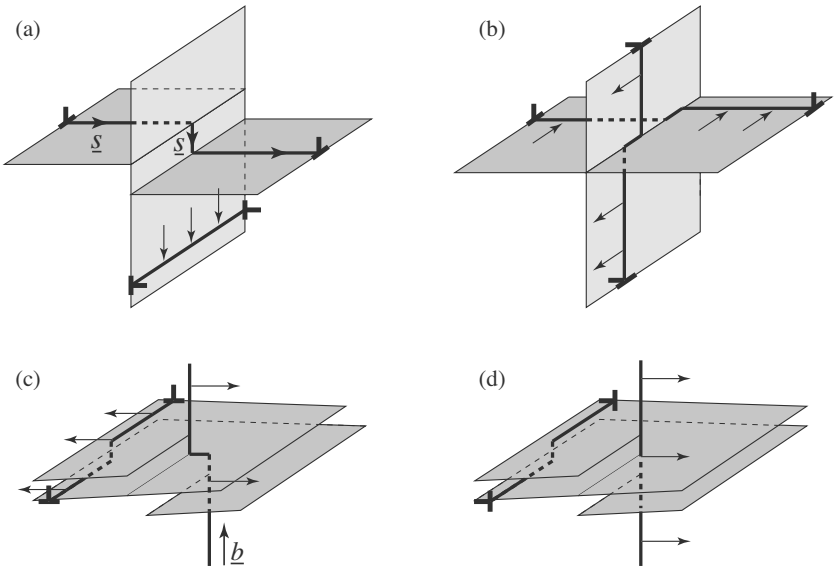

Figure 41. Straight dislocations after intersecting with another one normal to it; (a) two edges with normal Burgers vectors, (b) two edges with parallel Burgers vectors, (c) edge and screw with normal Burgers vectors, (d) edge and screw with parallel Burgers vectors.

the dislocations containing these jogs lies in the respective jog's glide planes $\underline{n}_{\text{jog}}$. This means that these jogs can, in principle, glide along with their parent dislocation's motion. If the glide plane $\underline{n}_{\text{jog}}$ is as "smooth" (section 1.4) as the dislocations' glide planes, the jogs will glide without additional resistance. However, this is not necessarily the case; additional Peierls stresses may apply for the jogs.

In figure 42 the intersection of two screw dislocations is considered; their line vectors (and consequently the Burgers vectors) are normal to each other. Both screws acquire jogs during the intersection. Unlike in the previous cases of figure 41, the jogs cannot glide with the rest of the dislocation because the direction of this motion does not lie in the glide plane of the jogs, as can be seen in figure 42(b). There the jogs may wait for approaching vacancies in order to climb in the indicated direction. This allows only for slow overall motion because the vacancy density is usually very low. On the other hand, at high stresses driving the dislocation forwards, the jogs may be dragged along, thereby emitting interstitial atoms. This can happen at

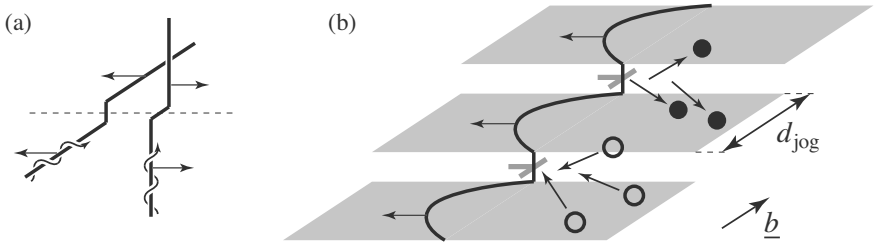

Figure 42. Straight screw dislocations after intersecting each other; (a) both screws acquire jogs; (b) the jogs must climb in order to follow the dislocation's motion by emitting or attracting interstitial atoms or vacancies. When the distance between the grey planes equals several atom layers, the jogs between them are called superjogs.

higher rates because the number of interstitials that can be generated and diffuse away is virtually unlimited. For motion in the opposite direction, or for jogs of opposite sign, the roles of vacancies and interstitials are exchanged; however, the energetics for vacancy and interstitial creation and mobility differ.

According to section 1.3 the critical stress τ_{jog} required for the dislocation to drag the jogs is $\tau_{\mathrm{jog}} = F_{\mathrm{jog}}/\left(bd_{\mathrm{jog}}\right)$, where d_{jog} is the average distance between them (figure 42(b)) and F_{jog} is the force to drag one jog. The latter is related to the energy $E_{\mathrm{v/i}}$ to create a vacancy/interstitial, which is expended while the jog climbs by the distance $d_{\mathrm{plane}} \approx b$ to the next plane. Assuming that the climb force is homogeneously distributed over the length d_{plane} such that $E_{\mathrm{v/i}} = d_{\mathrm{plane}} F_{\mathrm{jog}}$ yields

$$\tau_{\mathrm{jog}} = E_{\mathrm{v/i}}/\left(bd_{\mathrm{plane}} d_{\mathrm{jog}}\right) \tag{89}$$

For aluminium, for instance, the energy E_{v} to create a vacancy is about 0.67eV (Gottstein, 2004); the energy E_{i} of interstitial atoms is about two to four times higher. Even higher energies can occur when a screw dislocation is intersected by several other screws in the same glide plane. In that case, the length of the jog amounts to several times the Burgers vector. Such larger jogs are called superjogs; in order to move them with the gliding screw dislocation, several interstitials or vacancies must be created at once for every step of motion. Accordingly, the respective energy and the force of the superjog are larger.

In figure 42(b) it can be seen that the screw dislocation bows out between the jogs, like between all obstacles. The curvature of bending is limited by the obstacle force in relation to the line tension (see section 2.1), or by

the normalized obstacle strength $k = F_{\text{jog}}/(2S)$ of equation (74). With $S \approx \mu b^2/2$ and the values $\mu = 27\text{GPa}$, $b = 0.286\text{nm}$ and $E_{\text{v}} = 0.67\text{eV}$ for aluminium, k for vacancy creating jogs is found to be about 0.17; this means that the bending is weaker than in figure 31(a). Interstitials creating jogs or superjogs will cause stronger bending. In case of superjogs with $k \geq 1$ the dislocation will bend forwards like in the case of the Orowan process, but annihilation like in figure 18 will not occur (immediately) in the present case because the dislocation bows involved lie in parallel but different planes. Further details on jogs and superjogs can be found in (Hull and Bacon, 1992).

A possibly important effect of climbing jogs on plasticity is that this motion is thermally activated. This can introduce a strain rate and temperature dependence of plasticity in a similar way as solutes do (section 3.4). But the activation events are different and involve different activation energies; moreover the vacancy density and the jog density play important roles. Since these densities inevitably increase with continued plastic deformation as dislocations intersect each other and move on, work hardening can be affected in particular.

Dislocation reactions Dislocations can be subjected to exothermal reactions with other dislocations. A trivial example for this is when two dislocations with opposite sign meet in the same glide plane: they will annihilate each other irreversibly, like in the case of the Orowan process. Even when they are not in the same glide plane but come very close (neighbouring parallel planes, for instance), they can annihilate spontaneously and thereby release a row of vacancies or interstitial atoms. These reactions lower the free energy of the system and have a softening effect because the dislocation density is lowered.

A dislocation reaction can also occur when two dislocations in different non-parallel glide planes meet and partially annihilate, thereby lowering their combined energy. A prominent example for this is the formation of a Lomer-Cottrell lock, in which two partial dislocations lying in different glide planes react, as outlined in figure 43: The reacting partials P2 and P3 have the Burgers vectors $a/6\,[\bar{1}2\bar{1}]$ and $a/6\,[1\bar{1}2]$, respectively. They have the same magnitude $b_{\text{p}} = b/3^{1/2}$ and, for the most part, point in opposite directions. The resulting dislocation after the reaction has the Burgers vector $a/6\,[011]$ with the length $b_{\text{LC}} = b/3$. The energy of this dislocation is much lower than the combined energy of the reacting partials ($E^* \sim b^2$, equations (6) and (8)), therefore, this reaction is favourable and almost irreversible. In a realistic network of curved dislocations the reaction will only occur over a finite length, as indicated in figure 43. High stresses on the partials P2 and

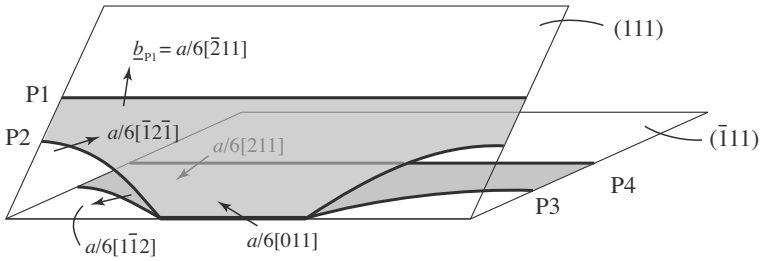

Figure 43. A Lomer-Cottrell-Lock formed locally by two Shockley partial dislocations from different planes. The length of the combined Burgers vector $a/6\,[011]$ is particularly small.

P3 may unzip this lock, but this is unlikely to happen because usually, the initial dissociated dislocations have been driven by an external stress such that they form the lock; hence essentially, a stress inversion is required to unzip this lock. The Burgers vector of the combined lock dislocation does not lie in either of the two initial glide planes. Therefore, this dislocation cannot glide with the original dislocations and hence locks them.

Another possible dislocation reaction can occur when dislocations intersect, like in figure 41(b). By the indicated motion of the two dislocations in this figure, a cube of material will be transformed into the shape of figure 44(a). Two alternatives to create the latter shape are indicated in figures 44(b) and (c). In figure 44(b), two straight edge dislocations with parallel Burgers vectors and normal line vectors move in the same direction; in 44(c) two angular dislocations move. The particular feature to be noticed here is that when the angular dislocations meet in their angles, this arrangement is indistinguishable from the case when the straight dislocations of figure 44(b) intersect. In this moment the configuration may switch from (b) to (c) or vice versa; this switch is called a collinear reaction. This reaction can be favourable for instance under certain stress conditions, or driven by dislocation length reductions which are possible in real cases where dislocations are actually curved.

A collinear reaction may also happen to the dislocations sketched in figure 41(b), which move in opposite directions and are therefore certain to intersect. The dislocations are driven in the indicated directions by given stresses, the origin of which plays no role. After the reaction occurs, the result is that of figure 44(d): for each of the angular dislocations created, the driving stresses on the two arms are opposing each other. At least in part this impedes further glide of the angular dislocations. Moreover, their

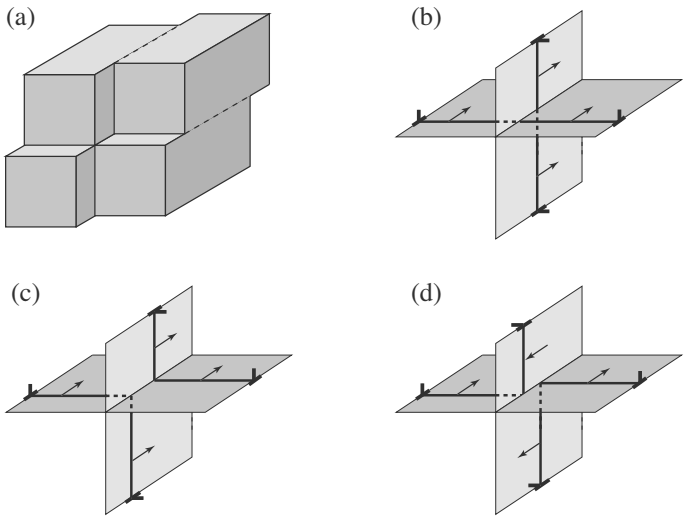

Figure 44. The shape in (a) is created from a cube by the dislocation motion in figure 41(b), or by the combined motion of the straight or angular dislocations in (b) or (c). A switch between the configurations (b) and (c) is possible when the two dislocations intersect. Likewise, (d) can be the result of a switch when the dislocations of figure 41(b) intersect. The resulting angular dislocations are essentially immobile.

glide can no longer lead to the shape of figure 44(a). Similar to the case of dislocation dipoles (section 1.3), angular dislocations are immobile or at least less mobile, so that new mobile dislocations must be created for continued plasticity. From this, a rise in material strength is to be expected, increasingly so with the number of dislocation intersections. These, in turn, increase with plastic strain. Dislocation dynamics simulations (Devincre et al., 2005) have approved that the collinear reaction in fact makes a significant contribution to work hardening.

Non-planar dislocations The angular dislocations of the previous section generated during dislocation intersections are one example of non-planar dislocations: each dislocation arm is curved in its own glide plane, and two planes are involved. Another case of a non-planar dislocation is given when a dislocation leaves its primary glide plane over a certain length. Here, like in section 1.3, a distinction between climb and cross-slip must be made: a piece of dislocation with screw character may glide into another

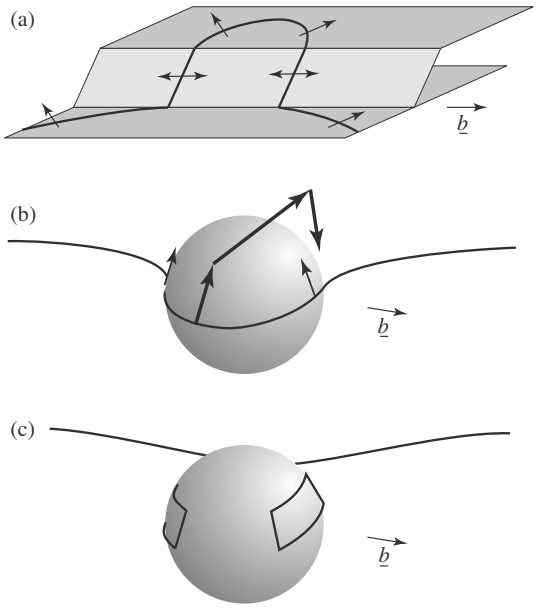

Figure 45. (a) Double cross slip of a piece of screw dislocation, arrows indicate glide directions; (b) a dislocation overcoming a particle by a combination of cross slip (big arrows) and climb (smaller arrows); (c) when a particle is overcome by cross slip alone, two prismatic dislocation loops of opposite signs are left behind, which may vanish later on by diffusion along the particle interface.

glide plane; however, a piece of edge dislocation can only climb. The latter involves material transport (diffusion) and is, therefore, slow.

In figure 45(a) a case of double cross slip is sketched: a piece of dislocation changes its glide plane twice. Changing the glide plane involves an angle to be created on the dislocation, which is energetically unfavourable. Hence there must a driving force, like from an external stress, for cross slip to occur. In contrast, climb may occur when there is an abundance of vacancies: they are attracted by edge dislocations, thereby making them climb.

Since dislocations are curved and have mixed character in general, cross slip and climb will have to occur concurrently. This means for instance that a driving force for cross slip will at the same time act as a driving force for the generation or absorption of vacancies or interstitials: the line ten-

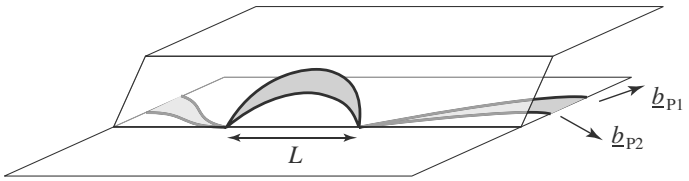

Figure 46. Cross slip of a dissociated screw dislocation. The grey area indicates the stacking fault.

sion will pull on the edge parts of the dislocation. In figure 45(b) a case is sketched where a particle is about to be overcome by a dislocation. This particle cannot be sheared. Hence it may be overcome by the Orowan process (section 2.1), or by a combination of cross slip and climb (large/smaller arrows in figure 45(b)). When cross slip and climb can take place at equal velocities, the dislocation can locally leave its primary glide plane near the particle and move back to this plane beyond it. On the other hand, when the edge components of the dislocation are unable to climb (for instance due to low temperature), the dislocation may overcome the particle by creating two prismatic dislocation loops, as sketched in figure 45(c). The prismatic loops can vanish later on by diffusing vacancies or interstitials, while the dislocation moves on in its primary glide plane. The details of what actually happens depends on a number of parameters like all stress components and the energetics and densities of vacancies and possibly interstitial atoms. Here the term "energetics" summarizes all activation energies for the creation and migration of vacancies and interstitials.

A dissociated screw dislocation cannot cross slip directly. One model for cross slip in this case is that the corresponding partial dislocations recombine to form a perfect dislocation over a certain length L before this piece of dislocation glides into the secondary plane. There it may dissociate again, as indicated in figure 46. The recombination of the two partials is a thermally activated event similar to that described in section 3.4 for overcoming obstacle walls. This explains the fact that cross slip is observed especially at high temperatures. In materials with a high stacking fault energy, like aluminium, the distance between the partials is very low (equation (23)). This means that the corresponding activation enthalpy in these materials is low, and that cross slip is very frequent even at low temperatures. This is in fact observed in aluminium alloys. However, it should also be noted that molecular dynamics simulations in literature have demonstrated the possibillity that a dissociated screw dislocation can cross slip without the recombination of the partials. In that case, cross slip must be accompanied

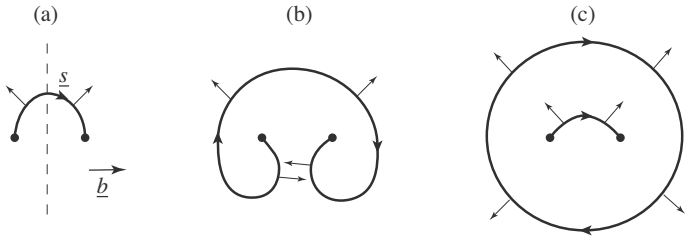

Figure 47. Operation of a Frank-Read dislocation source. The points indicate where the dislocation enters from another plane. In (b), two dislocation parts with edge character and opposite sign are about to annihilate each other; in (c) an expanding loop has been generated, and the new source is reestablished. The dashed line in (a) indicates a potential surface of the material.

by climb of the edge components of the partials.

Dislocation sources A very important aspect of cross slip is that it generates a Frank-Read dislocation source that can generate a virtually infinite number of new dislocations. Figure 47 represents the upper plane of figure 45(a), where double cross slip had just occurred. Under a given stress the dislocation segment bows out forwards between the points in which it enters this plane. When a critical stress is reached, the dislocation can move on to form the configuration of figure 47(b). Then, two dislocation parts with edge character and opposite sign annihilate each other (two half planes of atoms combine to form a full plane). The result is that of figure 47(c): an expanding dislocation loop enabling plastic deformation and a new segment, which can act as a dislocation source again.

The aforementioned critical stress is similar to that for the Orowan process: it depends on the distance between the fixed points, like τ_{Orowan} of equation (26) depends on the free space $L_{\mathrm{cc}} - 2R$ between obstacles. However, this is only an approximation because the dislocation parts outside the plane of figure 47 also cause significant stresses. Moreover, once the source has created a loop or several ones, these loops shield the external stress to some degree: the upper half of the loop in figure 47(c) repels the segment in its centre, pushing it downwards, and the lower part of the loop attracts the segment, also pulling it downwards. This means that only a finite number of loops can be generated at a given external stress, before the source "dries up". In dislocation dynamics simulations (as of yet, unpublished) it has been shown that this shielding effect is essentially independent of the size

of the (expanding) loops. For continued plastic deformation, the external stress must be increased further. Obviously this shielding effect contributes to work hardening.

When a dislocation changes its glide plane in a single point and ends on a free surface, this point can act as a spiral dislocation source. This is indicated in figure 47(a) by the dashed line: if this line describes a free surface and only the right half, for instance, of the figure is actually present, then the remaining dislocation arm can spiral around the fixed point and create half dislocation loops extending to the right into the material, just as if a mirrored counterpart were present on the left side (see section 1.3). The single fixed point may stem from half a double cross slip event (for instance, only the right half of figure 45(a)) or it may be one ending point of a superjog (see figure 42(b)).

4.2 Computational Aspects for 3-D Simulations

Some aspects of 2-D dislocation dynamics simulations, like segmentation, have been covered in section 3.1. They remain valid for 3-D simulations, but additional considerations are necessary in 3-D. For instance, decisions must be made on which glide planes are active, how cross slip is activated, and if or how climb is enabled. Generally speaking, the local direction of motion must be chosen. The subsequent considerations originate from the present author. However, there are a number of other successful approaches in literature, all with specific characteristics, see e.g. (Zbib et al., 2004), (Zbib et al., 2000a), (Zbib et al., 2000b), (Schwarz, 1999), (Devincre et al., 2001), (Devincre and Condat, 1992), (von Blanckenhagen et al., 2004), (von Blanckenhagen and Gumbsch, 2004), (Hartmaier and Gumbsch, 2004) (Ghoniem, 2000).

Direction of motion The direction of motion is unequivocal in 2-D (normal to the line vector, figure 28), but in 3-D, the glide plane must be chosen. This can be done by using predefined glide planes, depending on the crystal structure, and switching between these planes randomly with certain probabilities. These probabilities depend on temperature and on the resolved shear stresses in the glide planes of choice. But they also depend on the local dislocation configuration: a certain length of screw dislocation is required for cross-slip. But since dislocations are curved in general, it remains difficult to define such a critical length. In case of dissociated dislocations, the partial dislocations need to be merged into a perfect one over a certain length L in order or cross slip, as indicated in figure 46. This is known to

occur in a thermally activated manner, similar to the case of a dislocation overcoming an obstacle wall in figure 39. The merged length L may be used as a parameter to formulate the cross slip probability. But as seen later on, the merged length is not well-defined either.

An alternative to the approach above with predefined glide planes is to allow the simulated dislocations to move in any direction normal to its line, in principle, and to confine the motion to the preferred directions by other means. For instance, Xiang and Srolovitz (Xiang and Srolovitz, 2006) have applied the level-set method to simulate a dislocation overcoming a second phase particle. The authors used a strongly reduced dislocation mobility (a large drag factor B) for climb directions in order to account for the slowness of climb relative to slip.

Another concept using dislocations allowed to move in any direction is suggested subsequently. In this concept, a 3-D Peierls potential is used to make the dislocations prefer certain directions. It involves the symmetry and periodicity of the crystal structure under consideration. A dislocation tends to remain in low energy states within this potential; minor deviations cause stresses that drive the dislocation back. But larger deviations, caused for instance by thermal pulses, can make the dislocation leave its primary glide plane. In figure 48(a) this concept is sketched. In every point equivalent to that indicated by "0", the dislocation is free to move into the directions indicated by A, B, or C, and it will do so with the probabilities $P_A > P_B > P_C$ when the arrow in figure 48 indicates the Peach-Koehler force of equation (18).

In general, a dislocation would be curved in its glide plane, and it may even have kinks as indicated in figure 48(b). There, a piece of the dislocation (grey) has left its primary glide plane and moved into a parallel one. This motion involved double cross slip and, at the same time, climb. This means that a number of vacancies (or possibly interstitial atoms) have been created or consumed. In the concept of the 3-D Peierls potential, this means that also the energy for vacancy formation and consumption is to be considered for every geometrically necessary vacancy. The strength of the Peierls potential defines the degree of confinement.

Dislocation merging An important difference between 2-D and 3-D dislocation dynamics simulations is that there are non-trivial dislocation reactions possible in 3-D. Examples are the lock formation in figure 43 and the switch between the configurations of figures 44(b) and (c). In such reactions, dislocations can touch or intersect each other, which implicates numerical problems due to the stress singularity in the dislocations' cores. In order to avoid such singularities, all stress components defined by stress formulas

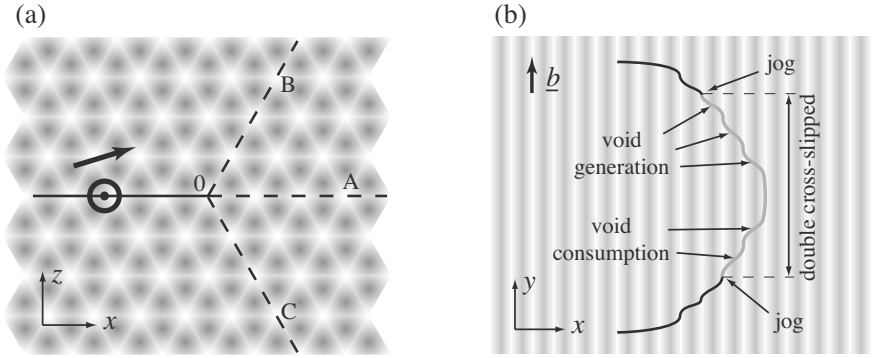

Figure 48. Concept of a 3-D Peierls potential to confine a dislocation capable of moving in any direction to glide planes. Darker shades of grey indicate a higher potential energy. (a) Straight screw dislocation along the y-axis; (b) a curved dislocation (with kinks), a piece of which (grey) has moved into a parallel glide plane.

like (49) or (58) can be multiplied by a function $f_{\mathrm{core}}(r)$ like

$$f_{\mathrm{core}}(r) = \frac{r^2}{r^2 + r_{\mathrm{core}}^2} \tag{90}$$

which accounts for the atomistic nature of the dislocation. Here, r is the distance from the dislocation and $r_{\mathrm{core}} \approx b$ is an adjustable parameter for the core radius. Equation (90) ensures that all stress components vanish in the dislocation core. Applying this function is essentially equivalent to using Peierls' dislocation model (Peierls, 1940) instead of Volterra's purely elastic approach (Volterra, 1907), on which all previous functions are based.

Besides avoiding the stress singularity in the code, a decision must be made for dislocation dynamics simulations on how to handle the joined dislocation part, like the Lomer-Cottrell lock (figure 43). One possibility is to ignore the joining, such that the dislocations coincide as indicated in figure 49(a). As a result of $f_{\mathrm{core}} \sim r^2$ for $r \ll r_{\mathrm{core}}$, and $\tau \sim r^{-1}$ for all elastic stresses, actually a linearly increasing interaction stress proportional to r would act inside the cores, which keeps attracting dislocations close together in a numerically stable way. This approach allows the simulations to automatically decompose the lock back into the two partial dislocations, provided that strong stresses on the side arms P2 and P3 in figure 43 tear them apart. This approach is convenient and useful if the dislocations that have merged are distinguishable in general. In the case of the Lomer-Cottrell

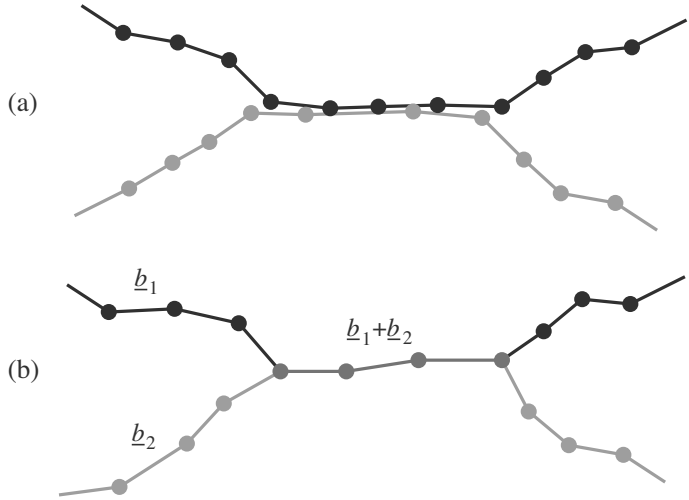

Figure 49. Merging of two dislocations (a), possibly in different glide planes, by the introduction of triple junctions (b). For the reverse effect from (b) to (a), the triple junctions may move towards each other until a quadruple junction is formed. If the Burgers vectors $\underline{b}_1$ and $\underline{b}_2$ differ, the respective dislocations are separated.

lock the distinction can always be made because the Burgers vectors of the respective partials differ.

On the other hand, dislocation reactions may also occur between dislocations with equal Burgers vectors, like in the case discussed in section 4.1 with regard to figures 44(b) and (c). There may even exist yet unidentified kinds of dislocation reactions. In such cases, ignoring the ambiguity of the dislocation configurations after intersections or after merging can lead to possibly severe errors in continued simulated plasticity. Therefore, in general, any possible cross-linking of dislocations should be considered. This can be done for instance by allowing dislocations to fully merge in one or several calculation nodes, i.e. in dislocation pieces with combined Burgers vector, as indicated in figure 49(b). Merging may start in a single node when two nodes from different dislocations come very close. This works for attracting as well as for repelling dislocations which are driven towards each other by external stresses. Starting from the first merged node (quadruple junction), its neighbour nodes will (or will not) attract each other and extend the merging to a piece of dislocation with two triple junctions at its ends. The reverse effect will be accomplished by the triple junctions mov-

ing towards each other until a quadruple junction is formed. When this happens, the junction can be resolved, and the four adjacent dislocation segments can be rejoined to two full dislocations as the Burgers vectors allow. In the case that all four Burgers vectors are equal ($\underline{b}_1 = \underline{b}_2$) in figure 4.9(b)), a decision is required on which dislocation segments are to be joined, depending on the local stresses.

Calculation effort In dislocation dynamics simulations (2-D or 3-D), the largest numerical effort lies in the calculation of the elastic interaction stresses between dislocation segments. Roughly spoken, every segment interacts with every other segment, which leads to an effort proportional to N^2. In simulations, the number of interaction partners must be reduced to those within a certain cut-off distance d_{cut} in order to keep the effort low. However, d_{cut} must be pretty large because the dislocation stress decreases only as $1/d_{\mathrm{cut}}$. For N segments with M interaction partners each, this leads to a calculation effort per integration step proportional to $N \cdot M$, where N and M can easily exceed 10000. Assuming that one segment-segment interaction of a single time step takes one microsecond to compute, it becomes obvious that the simulations are slow, given that at least tens of thousands of time steps are required for a meaningful simulation. Therefore, when aiming for dislocation dynamics simulations, measures to reduce the numerical effort need to be planned from the start.

Three measures used by Mohles (Mohles, 2001c) have proved to be quite successful. Firstly, it should be kept on mind that the calculations will implicate several small error contributions. Examples are the error which is introduced by a finite cut-off radius d_{cut}, or the errors involved with the spatial resolution Δs_i and with the finite stress increments $\Delta\tau$ as discussed in section 3.1. All error contributions have to be negligible. Reducing the error limits involved with one special respect often means dramatically increased calculation times. The overall error may still remain large as a result of other error influences. Hence calculation time would be wasted; it is, therefore, extremely useful to have equal error limits for all error influences involved.

Another measure to reduce the calculation effort is to introduce the possibility of local equilibria. Often, only parts of the dislocations move fast while the rest is hardly moving. This latter part can be put to sleep until something happens that might destroy the local equilibrium. The sleeping parts still act as interaction partners, but they do no stress evaluations on their own. When the external stress is increased, or when the stresses from other dislocation parts in the vicinity changes due to motion, the sleeping parts should be "awakened" to newly evaluate whether the state of local

equilibrium is still valid. If so, these parts can be put back to sleep, and otherwise they start moving. The definition of such local equilibria introduces another error contribution, the amount of which should again be kept as small or large as the other ones.

Thirdly, it can be exploited that the interaction stress of distant dislocation segments is low. Like in molecular dynamics simulations, the numerical effort can be reduced to $N \cdot M(d_{\mathrm{cut}})$ where $M(d_{\mathrm{cut}})$ is the number of interaction partners within a cut-off distance d_{cut}, beyond which, all contributions from interaction partners can be neglected. To find the relevant interaction partners fast, the cell method can be applied. This consists of two steps both the efforts of which scale with N^1: Firstly all N objects (dislocation segments or atoms in the case of molecular dynamics) tell "the space" where they are located; this space memorizes these locations in a discrete way, for instance by means of a 2-D or 3-D array of pointers or indices representing subspaces (cells). The array covers the whole simulated space, and the pointers or indices point to the corresponding objects. Secondly, all objects can ask "the space" which other objects are close ($d < d_{\mathrm{cut}}$) by examining the neighbouring subspaces. Hence the neighbour objects are found quickly with an effort that scales optimally with N^1.

In the case of molecular dynamics, $M(d_{\mathrm{cut}} \ll N)$, so that the numerical effort is lowered strongly. But in the case of dislocation segments, the condition $M \ll N$ it is not quite sufficient because the interaction is long-ranged: $\tau \sim d^{-1}$. This means that d_{cut} must be chosen pretty large so that the number $M(d_{\mathrm{cut}})$ also gets large, $M \approx N$. Hence the efficiency gain from the cell method alone is limited.

However, the cell method can be refined by taking basic physical principles into account. For instance, the interaction between very distant segments can change only slowly in time, depending on their velocities. Hence the interaction stress of the more distant segments needs to be calculated less often. This principle can be utilized most efficiently by introducing multiple shells of interaction distances around segments. Each segment should remember the interaction stresses of all segments which are located in certain shells (distance intervals) around it, separately for each shell. Hence, every segment can re-use the stress values it remembers instead of recalculating them. Since the outer, larger shells containing many interaction partners collects only very distant partners, the high calculation effort for this shell is required only infrequently.

With all the above measures to reduce the numerical effort combined, discrete dislocation dynamics simulations are speeded up by several orders of magnitude, increasingly so for larger simulated volumes.

Bibliography

R.J. Arsenault, S. Patu, and D.M. Esterling. Computer simulation of solid solution strengthening in fcc alloys: Part i. friedel and mott limits. *Met. Trans. A.*, 20A:1411–1418, 1989a.

R.J. Arsenault, S. Patu, and D.M. Esterling. Computer simulation of solid solution strengthening in fcc alloys: Part ii. at absolute zero temperature. *Met. Trans. A.*, 20A:1419–1428, 1989b.

D.J. Bacon. A method for describing a flexible dislocation. *Phys. Stat. Sol.*, 23:527–538, 1967.

L.M. Brown. The self-stress of dislocations and the shape of extended nodes. *Phil. Mag.*, 10:441–466, 1964.

L.M. Brown. A proof of lothes theorem. *Phil. Mag.*, 15:363, 1967.

B. Devincre. Three dimensional stress field expressions for straight dislocation segments. *Solid State Comm.*, 93:875–878, 1995.

B. Devincre and M. Condat. Model validation of a 3d simulation of dislocation dynamics: discretization and line tension effects. *Acta metall. mater.*, 40:2629–2637, 1992.

B. Devincre, L.P. Kubin, C. Lemarchand, and R. Madec. Mesoscopic simulations of plastic deformation. *Mat. Sci. Eng.*, 309-310:211–219, 2001.

B. Devincre, T. Hocb, and L P. Kubin. Collinear interactions of dislocations and slip systems. *Mat. Sci. Eng. A*, 400-401:182–185, 2005.

M.S. Duesbery, N.P. Louat, and K. Sadananda. The numerical simulation of continuum dislocations. *Phil. Mag.*, A65:311–325, 1992.

J.D. Eshelby. The continuum theory of lattice defects. In F. Seitz and D. Turnbull, editors, *Solid State Physics*, page 79. Academic Press Inc., New York, Vol.3, 1956.

A.J.E. Foreman and M.J. Makin. Dislocation movement through random arrays of obstacles. *Phil. Mag.*, 14:911–924, 1966.

A.J.E. Foreman and M.J. Makin. Dislocation movement through random arrays of obstacles. *Can. J. Phys.*, 45:511–517, 1967.

J. Friedel. *Dislocations*. Pergamon Press, 1964.

N.M. Ghoniem. Computational methods for mesoscopic, inhomogeneous plastic deformation. In D. Walgraef, C. Worner, and J. Martinez-Mardones, editors, *Materials Instabilities*, pages 76–158. World Scientific, Singapore, 2000.

G. Gottstein. *Physical Foundations of Masterials Science*. Springer-Verlag, 2004.

A.G. Granato, K. Luecke, J. Schlipf, and L.J. Teutonico. Entropy factors for thermally activated unpinning of dislocations. *J. Appl. Phys.*, 35: 2732–2745, 1964.

K. Hanson and J.W. Morris. Limiting configuration in dislocation glide through a random array of point obstacles. *J. Appl. Phys.*, 46:983, 1975.

A. Hartmaier and P. Gumbsch. Discrete dislocation dynamics simulation of crack-tip plasticity. In D. Raabe, F. Roters, F. Barlat, and L.-Q. Chen, editors, *Continuum Scale Simulation of Engineering Materials*, pages 413–427. Wiley-VCH, Weinheim, 2004.

J.P. Hirth and J. Lothe. *Theory of Dislocations*. Krieger Publishing Company, 1992.

D. Hull and D.J. Bacon. *Introduction to Dislocations*. Pergamon Press, 1992.

R.D. Isaac and V. Granato. Rate theory of dislocation motion: Thermal activation and inertial effects. *Phys. Rev. B.*, 37:9278, 1988.

K.M. Jassby and T. Vreeland. Dislocation mobility in pure copper at 4.2°k. *Phys. Rev.*, 8B:3537–3541, 1973.

U.F. Kocks. Kinetics of solution hardening. *Metall. Trans. A*, 16:2109–2129, 1985.

U.F. Kocks, A.S. Argon, and M.F. Ashby. Thermodynamics and kinetics of slip. *Prog. Mat. Sci.*, 19:1, 1975.

R. Labusch and R.B. Schwarz. Simulation of thermally activated dislocation motion in alloys. In *Proc. of ICSMA 9*, pages 47–69. 1992.

I.M. Lifshitz and V.V. Slyozov. The kinetics of precipitation from supersaturated solid solutions. *Phys. Chem. Solids*, 19:35–50, 1961.

V. Mohles. *Thermisch aktivierte Versetzungsbewegung in Kristallen auf der Grundlage von Simulationsrechnungen*. Shaker Verlag, 1997.

V. Mohles. The critical resolved shear stress of single crystals with long-range ordered precipitates calculated by dislocation dynamics simulations. *Mat. Sci. Eng. A*, 365:144–150, 2004.

V. Mohles. Simulation of particle strengthening: Lattice mismatch strengthening. *Mat. Sci. Eng. A*, 319-321:201–205, 2001a.

V. Mohles. Simulation of particle strengthening: the effects of the dislocation dissociation on lattice mismatch strengthening. *Mat. Sci. Eng. A*, 319-321:206–210, 2001b.

V. Mohles. Computer simulations of the glide of dissociated dislocations in lattice mismatch strengthened materials. *Mat. Sci. Eng. A*, 324:190–195, 2002.

V. Mohles. Superposition of dispersion strengthening and size mismatch stengthening: computer simulations. *Phil. Mag.*, 83:9–19, 2003.

V. Mohles. Simulation of dislocation glide in overaged precipitation-hardened crystals. *Phil. Mag. A*, 81:971–990, 2001c.

V. Mohles and B. Fruhstorfer. Computer simulations of orowan process controlled dislocation glide in particle arrangements of various randomness. *Acta. Mat.*, 50:2503–2516, 2002.

V. Mohles and E. Nembach. The peak- and overstaged states of particle strengthened materials: computer simulations. *Acta. Mat.*, 49:2405–2417, 2001.

V. Mohles and D. Rönnpagel. Thermal activation analysis of dislocations in obstacle fields. *Comp. Mat. Sci.*, 7:98–102, 1996.

G. Monnet. Investigation of precipitation hardening by dislocation dynamics simulations. *Phil. Mag.*, 86:5927–5941, 2006.

N.F. Mott and F.R.N. Nabarro. *Creep and plastic flow.* The Physical Society, London, 1948.

E. Nadgornyi. Dislocation dynamics and mechanical properties of crystals. *Progr. Mat. Sci.*, 31:1, 1988.

E. Nembach. *Particle Strengthening of Metals and Alloys.* John Wiley, 1996.

E. Orowan. über den mechanismus des gleitvorganges. *Z. Phys.*, 89:634, 1934.

M. Peach and J.S. Koehler. The forces exerted on dislocations and the stress fields produced by them. *Phys. Rev.*, 80:436, 1950.

R. Peierls. The size of a dislocation. *Proc. Phys. Soc., London*, 52:34, 1940.

M. Polanyi. über eine art gitterstörung, die einen kristall plastisch machen könnte. *Z. Phys.*, 89:660, 1934.

W.H. Press, S.A. Teukolsky, V.T. Vetterling, and B.P. Flannery. *Numerical Recipes in C.* University Press, 1992.

K.W. Schwarz. Simulation of dislocations on the mesoscopic scale. i. methods and examples. *J. Appl. Phys.*, 85:108–119, 1999.

R.B. Schwarz and R. Labusch. Dynamic simulation of solution hardening. *J. Appl. Phys.*, 49:5174–5187, 1978.

G.I. Taylor. *Proc. R. Soc., London*, A145:362, 1934.

V. Volterra. Sur lequilibre des corps elastiques multiplement connexes. *Ann. Ecole Norm. Super.*, 24:401–517, 1907.

B. von Blanckenhagen and P. Gumbsch. Discrete dislocation dynamics simulation of thin film plastcity. In D. Raabe, F. Roters, F. Barlat, and L.-Q. Chen, editors, *Continuum Scale Simulation of Engineering Materials*, pages 397–412. Wiley-VCH, Weinheim, 2004.

B. von Blanckenhagen, E. Arzt, and P. Gumbsch. Discrete dislocation simulation of plastic deformation in metal thin films. *Acta Metallurgica*, 52: 773–784, 2004.

C. Wagner. Theorie der alterung von niederschlägen durch umlösen. *Elektrochem.*, 65:581, 1961.

J. Weertman. *Elementary Dislocation Theory.* Oxford University Press, New York, 1992.

Y. Xiang and D.J. Srolovitz. Dislocation climb effects on particle bypass simulations. *Phil. Mag.*, 86:3937–3957, 2006.

H.M. Zbib, T.D. de La Rubia, M. Rhee, and J.P. Hirth. 3d dislocation dynamics: stress-strain behaviour and hardening mechanisms in fcc and bcc metals. *J. Nucl. Mater.*, 276:154–165, 2000a.

H.M. Zbib, M. Rhee, and J.P. Hirth. On plastic deformation and the dynamics of 3d dislocations. *Int. J. Mech. Sci.*, 40:113–127, 2000b.

H.M. Zbib, M. Hiratani, and M. Shehadeh. Multiscale discrete dislocation dynamics plasticity. In D. Raabe, F. Roters, F. Barlat, and L.-Q. Chen, editors, *Continuum Scale Simulation of Engineering Materials*, pages 201–229. Wiley-VCH, Weinheim, 2004.